A THEORETICAL INVESTIGATION OF GAS-SOLID INTERACTION PHENOMENA

By

JERRY ALAN LORENZEN

Bachelor of Science

Midland Lutheran College

Fremont, Nebraska

1966

Submitted to the Faculty of the
Graduate College of the
Oklahoma State University
in partial fulfillment of
the requirements for
for the Degree of
DOCTOR OF PHILOSOPHY
May, 1970

A THEORETICAL INVESTIGATION OF

GAS-SOLID INTERACTION

PHENOMENA

Thesis Approved:

Lionel M. Raff
Thesis Adviser

Neil Purdie

Herbert A. Pohl

John E. Moore

D. Durham
Dean of the Graduate College

ACKNOWLEDGEMENTS

I am deeply indebted to Dr. Lionel M. Raff for his advice, encouragement, and guidance throughout the course of this study.

John Coryell also deserves credit for several interesting and thought-provoking discussions.

This study was made possible by financial support from the Oklahoma State Research Foundation through a National Science Foundation grant. I also wish to thank the Oklahoma State University Computing Center for use of their facilities to complete this study. Appreciation is also expressed to the National Aeronautics and Space Administration for financial support in the form of a NASA Traineeship.

In addition, I would like to thank Mrs. Pat Hickman for her typing excellence and advice.

Finally, I would like to express appreciation to my wife, Barb, whose understanding, encouragement, patience, and sacrifice were instrumental in the preparation of this dissertation.

TABLE OF CONTENTS

LIST OF TABLES

LIST OF FIGURES

CHAPTER I

INTRODUCTION

Studies in the area of gas-solid interactions have been numerous in recent years. This development stems from the many important applications that depend on gas-surface interactions, the recent advances in technology that have opened the way for new experimental results, and the use of computers to develop theories that give a realistic molecular view of experiments.

In many areas of application the importance of gas-surface interactions is realized. Nevertheless, due to a lack of quantitative understanding, they are usually accounted for by rough empirical relations. An important problem in aerospace dynamics, for example, is determination of the free molecule drag coefficient, C_D, for a vehicle in motion in a rarefied gas. This number represents the momentum transferred between the vehicle surface and the gaseous particles with which it collides. Its value depends upon the initial and final velocity of gaseous molecules relative to the satellite surface. Unfortunately, the final relative velocity is not known *a priori*. For earth satellites approximate methods based on present experimental data and theoretical knowledge fix the

limits for C_D between 1.9 and 2.7.[1,2] A thorough knowledge of the interaction of gaseous particles with solid surfaces would permit more accurate determinations of C_D. In the process of gaseous heterogeneous catalysis, the first step of reaction is the collision of gaseous molecules with the catalytic surface or with particles adsorbed on that surface. A microscopic understanding of this type of reaction will require a knowledge of the initial step.[3] Heterogeneous nucleation, oxidation, corrosion, vapor deposition of materials in thin film formation, growth behavior of crystals at low saturation,[4] sound propagation in rarefied gases,[5] free molecule recovery temperatures,[6] and effusion from Knudsen cells[7] are all processes that depend upon the energy transfer occurring in gas-solid interactions.

Gas-surface interaction experiments began in 1911 when Knudsen[8] interpreted his results on the conduction of thermal energy from a fine wire in terms of an accommodation coefficient (AC) for thermal energy. It is defined by

$$AC = (E_g^f - E_g^i)/(E_s - E_g^i). \qquad (1)$$

The numerator, which represents the mean energy transfer associated with the gas-surface interaction, equals the mean energy of reflected particles E_g^f minus the mean energy of incident particles E_g^i. Since the interaction is, in general, incomplete, E_g^f has a value between E_g^i and E_s; E_s is the mean energy of a beam of particles that interacts completely and attains thermal equilibrium with the surface.

The denominator of Eq. (1) represents the energy transfer for the case in which the incoming particles attain equilibrium. Thus, the AC is a measure of the degree to which gas molecules attain thermal equilibrium with the surface. The AC can be expressed in terms of temperatures by representing the mean translational energy as

$$E = 2\bar{k}T \tag{2}$$

where $\bar{k}$ is Boltzmann's constant. Equation (2) represents the mean translational energy of particles issued from a body of gas in equilibrium at temperature T. These substitutions allow Eq. (1) to be written as

$$AC = (T_g^f - T_g)/(T_s - T_g). \tag{3}$$

In some cases the AC is found to be a strong function of $(T_s - T_g)$, and it is then more convenient to use the modified expression of Jackson[9]

$$AC = \lim_{\Delta T \to 0} (T_g^f - T_g)/\Delta T \tag{4}$$

where $\Delta T = T_s - T_g$. In effect, the AC is an expression for the average efficiency of energy exchanged per collision between a gas at temperature T_g and a surface at temperature T_s. The AC and the spatial scattering distribution of reflected particles are the experimentally measurable quantities that describe gas-solid interaction phenomena.

The majority of experimental work in the area of gas-solid interactions can be classified as conductivity cell measurements or molecular beam experiments. Although Knudsen[8] reported the first conductivity cell experiments, the critical importance of a clean metallic surface was not

realized until the work of Roberts[10] in the early 1930's. Most conductivity cell measurements have been obtained by the low pressure method. A wire filament is enclosed inside a glass tube filled with a gas at low pressure. The tube is held at a temperature T_w by a temperature bath. At low pressures the gas inside the tube is in thermal equilibrium with the tube walls so that $T_w = T_g$. The filament is kept at a temperature T_s by an electric current. The power input to the filament, which equals the actual power loss from the filament to the gas ($W_g = T_g^f - T_g$), is measured. The limiting expectation value for the power conducted away by the gas ($W_{KT} = T_s - T_g$) is calculated from kinetic theory and the measured pressure and temperatures. Then, the AC is readily calculated from the ratio of W_g to W_{KT}. The thermal jump method has also been employed to determine the AC in conductivity cells. For this method the gas pressure in the tube is between 10 and 100 mm. As a result, T_g is not equal to the temperature of the wall. Also a temperature discontinuity exists at the gas-solid interface -- the so-called temperature jump. The temperature jump difference can be obtained from a series of measurements of the thermal conductivity at different pressures; the results are used to determine the AC.[1] The underlying theory is not established although the results seem to be consistent with those of the low pressure method.[11]

Systems which have been studied in conductivity cells

include various combinations of the noble gases, N_2, and H_2 on W, Mo, Al, Be, Ni, Fe, Pt, Li, Na, K.[1, 11-20] The AC's of He and Ne on absorbed layers of K, Cs, H_2, D_2, O_2, N_2, CO_2, CH_4, C_2H_6, and C_2H_4 on W and Mo have also been determined.[14, 15, 19, 20] Some general results are as follows:

(a) The AC's approach unity at low T_g, decrease to a minimum at moderate T_g, and then increase again as T_g becomes large.[16]

(b) The AC's are larger for larger heats of adsorption if the mass ratios are approximately the same.[16]

(c) The AC's decrease as the ratio (M_g/M_s) decreases; M_g and M_s are the masses of the gaseous and surface particles, respectively.[14]

(d) The AC for ^4He is greater than that for ^3He, but the two values approach each other as T_g decreases.[14]

(e) The AC's increase considerably when adsorbed particles are present on the lattice surface.[15, 16, 20]

(f) The AC's approach a maximum at a half monolayer of adsorbed alkali atom coverage, and then decrease as a full monolayer forms.[14, 15]

Although the data gained from conductivity cells have

made a significant contribution to our knowledge of gas-surface interactions, the method has several inherent disadvantages. Bulk AC's for all possible incidence angles and velocities are measured. Therefore, the dependence of the AC on incidence angle and velocity cannot be determined. The method is also restricted to the condition of T_g less than T_s. For accurate measurements the gas must show little tendency to adsorb on the surface so most experiments have been limited to noble gases. Another problem is determination of the smoothness and crystal structure of the metallic surface. The conductivity cell experiments also fail to yield scattering distributions for given incidence angles.

Molecular beam experiments are, by their very nature, more complicated than conductivity cells, but they are capable of giving the data needed for accurate theoretical analysis. The method involves producing a collimated molecular beam that strikes a surface at any given spherical polar incidence angles Θ_i and ϕ_i for which the z axis is oriented normal to the surface. A movable detector is employed to determine the resulting scattering distributions. The initial state of the interaction, which includes the gaseous beam temperature T_g or particle velocity V_i, the surface temperature T_s, the incidence angles Θ_i and ϕ_i, and the crystal structure of the surface, can be specified. The effects of these conditions on the interaction can be independently studied.

The greatest difficulty in the molecular beam

experiments is surface contamination. Several methods have been employed in recent years to obtain clean surfaces. Crews[21] has cleaved LiF crystals in vacuum and observed diffraction peaks in scattered He beams. The scattering of He, H_2, D_2, and Ar from LiF has also been studied.[22, 23] Hinchen[24-26] has employed conventional ultra high vacuum techniques and observed quasi-specular spatial distributions for noble gases from Pt. Saltsburg and Smith[27-34] have utilized the method of continuous deposition of the metal surface at a rate faster than the contamination resulting from the background gas adsorption. The substrate material and temperature were controlled so as to insure epitaxial growth of single crystals. The scattering distributions of the noble gases, ^3He, NH_3, CH_4, H_2, HD, and D_2 from Au, Ag, and Ni surfaces have been studied. The results also include velocity-selected beams.[32]

An important experimental extension, which allows estimation of the energy transfer as well as the spatial distributions, has been introduced by Smith and Fite[35] and Datz, Moore, and Taylor.[36] They have roughly estimated the mean final velocity, $\bar{V}_f$, at each angular position of a detector by employing modulated beam techniques with synchronous detection. Although surface contamination was a problem in the early experiments, development of the method was an important step. Also, both T_s and T_g were varied so the conductivity cell restriction of T_g less than T_s was

removed. Hinchen[24-26] has used modulated molecular beams and phase sensitive detection techniques to obtain accurate data for the average velocities of noble gas atoms scattered from Pt. The AC's calculated from the velocity determinations are consistent with conductivity cell measurements. A major experimental advancement would be velocity selection of the reflected beam. The distribution of final velocities rather than the average final velocity for each angle of reflection could then be determined.

Some generally observed results of molecular beam experiments are as follows:

(a) Spatial distributions of reflected gaseous particles tend to be specular (the reflection angle equals the incident angle) for clean, large crystal surfaces.[30, 37]

(b) Spatial distributions from contaminated surfaces tend to be diffuse (cosine type scattering).[30]

(c) Scattering distributions tend to become more diffuse as the heat of adsorption increases.[29]

(d) Scattering distributions shift away from the surface normal and become narrower as the ratio (T_g/T_s) increases. This trend is least prominent in He.[30,38]

(e) Bimodal distributions have been observed for He, H_2, and D_2 beams scattered from Ag,[31] for He scattered from Pt,[3] for Ar scattered from LiF,[23] and for Ag scattered from Mo.[39] The extent of

the fine structure generally decreases as T_g or T_s increase and increases as Θ_i increases.

(f) Rotational energy accommodation apparently must be considered in order to compare the scattering of He with H_2 and D_2 from Ag and LiF.[22, 31]

(g) One eV Ar particles scattered from partially contaminated siver, mica, and brass surfaces give multiple lobes that have been called "back-scatter", "quasi-normal", and "quasi-specular" lobes.[40]

(h) Velocity-selected beams give scattering distributions that are similar to those from the corresponding Maxwellian beams.[32, 41]

(i) Interaction with a surface causes broadening of the gaseous particle velocity distribution.[41, 42]

(j) Particles scattered in the specular direction have lower AC's than those scattered closer to the normal.[26]

(k) In molecular beam experiments the AC is not limited to values between zero and unity.[26]

(l) Spatial scattering distributions become temperature independent at large T_s or T_g.[34, 43]

Conductivity cell and molecular beam experiments have contributed greatly to our knowledge of gas-solid interactions. At the same time, experiments have introduced many new problems. The origin of the bimodal distributions,

the reason for the unusual behavior of the AC as a function of increasing alkali atom coverage, the nature of the interaction potential, the similarity of velocity-selected and Maxwellian beam scattering, and the origin of the scattering patterns from contaminated surfaces are observations that are only partially understood. As is the case in many areas of current research, the best method for understanding gas-surface processes is a judicious combination of experimental measurements and theoretical interpretation.

Baule[44] introduced the first theoretical treatment of gas-surface interactions in 1914. In his classical model, the surface is assumed to be composed of non-interacting, hard spheres of mass M_s initially at rest. They interact with the gaseous atom of mass M_g according to the law of hard spheres. The resulting expression is

$$AC = 2M_gM_s/(M_g + M_s)^2 \ . \qquad (5)$$

This simple theoretical result is only useful for rough calculations.

In the 1930's several attempts employing the new quantum theory were proposed. The early one-dimensional (1D) models compute the probability that a surface atom in a vibration state i will undergo transition to a state j when struck by a gaseous atom with energy E_g^i. The exiting gas atom then has energy $E_g^f = (i - j)h\nu$. Jackson and Mott[9] have considered two types of interactions -- a rigid, elastic spheres model and a repulsive exponential

field. Devonshire[45] has employed the more realistic Morse potential to represent the molecular interaction. Adjustment of the Morse potential parameters gave results that seem to agree with experiment. However, as Goodman[46] has noted, the resulting parameters are not realistic. Shin[47-49] has employed a more recent 1D model. Jackson and Howarth,[50] Piampuu,[51] and Feuer[52] have extended their theories to include diatomic gaseous molecules and the effect of internal degrees of freedom on the AC. The early quantum theories are generally unsuccessful because of two shortcomings; they have difficulty in treating 3D motion over a realistic lattice, and they are unable to successfully treat the interaction when heavy gaseous particles are involved. The recent theories of Beder,[53] Howsmon,[54] Gilbey,[55] and Allen and Feuer[56] have made progress toward overcoming these difficulties. The results of quantum theories can be summarized by the statement of Trilling[57] in a recent review article:

> If any conclusion can be drawn from the quantum calculations, it is that they are more complex by far than the classical calculations; that the trends which they suggest appear consistent with experiment, but that considerably more work is required before a satisfactory theory can be claimed to be in existence.

Classical theories have been more common because they are inherently simpler, give better physical insight, and have generally been successful. Cabrera[58] and Zwanzig[59] have included the dynamics of the surface in the interaction process by treating the solid as a linear system of

masses and springs slightly displaced from equilibrium. Goodman[46, 60-65] has extended this model in a series of papers. The gaseous atoms were always required to strike perpendicularly to the surface and to impinge directly upon a surface atom. In the first paper unrealistic interaction potentials were used, but the importance of a 3D lattice, as compared to 2D and 1D lattices, was established.[60] In the second paper impurity atoms in the lattice were considered.[61] The third paper adopted realistic interaction potentials of the Morse type and used classical perturbation theory.[46] The extension of the next paper was to a simple treatment of thermal motion in the lattice.[62] In the fifth paper quantitative agreement with the AC's for several gases on tungsten was achieved by adjusting the Morse parameters.[63] It should be noted, however, that the model was again restricted to $T_s = 0^{\circ}K$ while for the corresponding experiments T_s was greater than T_g. In a recent paper Goodman[64] has retained the unrealistic assumptions of 1D gas particle motion normal to the solid, head-on atom surface collisions only, and a cold lattice. The form of potential function allowed removal of the usual perturbation theory restriction to small AC's. The known importance of a 3D lattice was reiterated; surface impurities were included, and the "critical initial effective temperature for trapping" was estimated. However, satisfactory comparison with experiment was impossible due to the many restrictions. Chambers[66, 67] has applied a similar

model. In general, these theories, which are extensions of the Zwanzig model, are capable of calculating AC's. However, as Trilling[57] has noted, it is probable that the AC is a coarse criterion that does not test detailed features of the models. Also, since these models require that gaseous atoms strike perpendicularly to the surface and impinge directly upon a surface atom, they cannot predict scattering distributions.

Several classical models that attempt to account for scattering distributions have been proposed. Goodman[68] has presented an extension of the Baule model. The surface was represented by an array of hard spheres initially at rest. The gas particle, which is also a hard sphere, could approach the lattice with any given incidence angle and could strike the lattice at impact points between lattice spheres. The interaction was assumed to obey the law of hard spheres. To obtain smooth scattering distributions, 22,500 trajectories aimed at points distributed over the unit cell were required. This number of trajectory calculations were possible because of the simplified nature of the interaction. The resulting scattering distributions agreed qualitatively with experiment, but the lobes were too broad. The resulting energy transfer was fit by a parametric equation. The AC was found to be rather insensitive to impact point, azimuthal incidence angle, and surface structure. Due to the nature of the assumptions (impulsive interactions and a cold lattice), the model is

only applicable in the limit of large (T_g/T_s).

Logan, Stickney, and Keck[69, 70] have suggested a simple scattering model that includes lattice motion. The surface was represented as a set of independent, oscillating hard cubes. The gaseous atom was incident on a surface cube at an angle Θ_i. The normal component of momentum exchange was assumed to obey the law of hard spheres; the tangential momentum was assumed to be unchanged. With these assumptions the probability that the particle would be emitted at an angle Θ_f with a velocity V_f could be calculated. The final expression for the lobe shape is a function of Θ_i, (M_g/M_s), and (T_g/T_s). The distribution of final velocities is predicted to narrow with increasing Θ_f. The results of the hard cube model are in surprising agreement with experiment considering the nature of the assumptions. Logan and Keck[71] have recently refined the model by replacing the impulsive interaction with a stationary well attractive potential and an exponential repulsive potential. Thus, the soft cube model allows for the effects of collision time and the natural vibrational frequency of the surface atoms. The interaction parameters were fit to experimental scattering distributions with realistic results. Good qualitative agreement was obtained for the variation of the angular position of the maximum of the scattering distribution. Madix and Korus[72] have attempted to extend the hard-cube model to include the effect of trapping on the angular distribution of scattered particles. Neglect of

internal energy accommodation and tangential momentum component changes make the attempted comparison with the experimental results for Ne, CH_4, and NH_3 scattered from Ag extremely qualitative.[29]

Oman[73-77] and his co-workers have introduced a new model of gas-solid interactions in an excellent series of papers. The surface was assumed to consist of mass points arranged in a given crystal configuration. The movable mass points were connected to fixed sites by harmonic springs. A Lennard-Jones (12-6) potential was assumed to interact between the gaseous atom and the atoms of the crystal lattice. Trajectories were followed by numerical integration of the classical motion equations. Arbitrary initial conditions of velocity, impact point, lattice vibrational-phase angle, and azimuthal approach angle were specified. The model was established in the first paper and the results of a few random trajectories were presented.[73] In the second paper the assumption of an independent oscillator lattice was studied; it gives essentially the same results as a coupled oscillator lattice.[74] Trajectories of He, Ne, and Ar on Ni were studied, and unusually large percentages of gas particles were trapped. The third paper studied the effect of crystal structure, surface layer, and lattice thermal motion on the energy transfer.[75] For the high incident particle energies of the early papers (0.1 - 15 eV), thermal motion of the lattice was found to be unimportant. A simple parametric

interaction model for momentum and thermal accommodation coefficients based on the detailed calculations was also developed. In a fourth paper the model was extended to diatomic gaseous molecules.[76] Again, the energy range was restricted to epithermal energies. Vibrational energy changes were small except at high energy, and rotational energy change varied linearly with incident translational energy. A fifth paper studied the scattering of noble gases from the FCC (111) silver surface.[77] The energy range was reduced (0.06 to 7.8eV), and lattice thermal motion was incorporated. Averaging over lattice phase was accomplished by replacing each trajectory result with a Gaussian distribution of trajectories centered at that point. In general, the predicted scattering distributions were too broad and the trapping probabilities were too large. Multiple peaks in the scattering distributions were observed although their origin remained uncertain. In a sixth paper the scattering of Ne, Ar and Xe from Ag (111) surfaces was studied further.[78] It was found that excessively large values of the interatomic binding energy had been responsible for the broad scattering patterns observed in the previous work. The author also concluded that statistical fluctuations were the major cause of the multiple peaks. Of the many models that have been proposed, the type suggested by Oman seems to require the minimal number of restrictions and is thus, the best-suited for studying gas-solid interaction phenomena.

Recently, a 2D model was employed by Raff, Lorenzen, and McCoy[79] to investigate both the energy transfer and scattering phenomena. In this work the crystal lattice was assumed to consist of three movable mass points connected to five fixed sites by harmonic springs while the incident gaseous atom was represented by a single mass point. Morse type potentials were assumed to operate between the gaseous atom and each movable lattice site. All particle motion was calculated by numerical solution of the classical Hamiltonian equations for the system.

By the use of Monte Carlo trajectory analysis, the dependence of the energy transfer coefficient (ETC) and spatial distribution of reflected particles upon various interaction parameters, incidence angle, gaseous beam velocity, and surface temperature was investigated. In general, the results indicated that the ETC increases with increasing beam temperature and beam velocity; decreases with increasing lattice force constant; increases with increasing attractive interaction between gas and surface; decreases with increasing incidence angle; and decreases as the surface temperature approaches and exceeds the gaseous temperature. The calculated spatial distributions were found to depend strongly upon incidence angle, attractive well depth, and surface temperature. Subspecular shifts (toward the surface normal) of the scattering maximum were predicted for increasing attractive well depth and surface temperature. Each of the above results

was observed to be in qualitative to semi-quantitative agreement with available experimental data.

Although it was concluded that the general approach was well-suited to the study of such heterogeneous interactions, it was found that the 2D model employed was inadequate with regard to predicting the actual shape of the scattering patterns. The calculated distributions were consistently too diffuse in character with half-widths in excess of experimental curves by almost an order of magnitude. Furthermore, the positions of the calculated maxima were consistently too subspecular in character. It was suggested that these effects might be artifacts due to the 2D nature of the model, and the need for extension to 3D was indicated.

The purpose of the present study is to formulate a realistic 3D, classical model that reproduces the results of molecular beam experiments and hence, leads to a molecular level understanding of the collision process. The crystal surface of the model is represented by nine movable mass points that are connected to all nearest-neighbors by harmonic springs. The mass and force constants for each of the nine lattice atoms can be varied so that a pure lattice or a lattice with surface impurities is represented. Adsorbed particles can also be represented by including movable mass points above the crystal surface. The potential acting between the adparticles and the lattice particles is assumed to be of the Lennard-Jones (12-6) type.

The interaction between the incident gaseous particle and the surface atoms is represented by a Morse potential. The initial conditions, which include the surface geometry, incidence angles, and particle momenta, are specified. With the assumption of classical mechanics the motion equations for the system can be solved numerically to give trajectories for the particles of the system. From the final state of the system the energy transfer is easily calculated. The results of many trajectories aimed at different points within the unit cell of the crystal surface give spatial scattering distributions. The effects that result from varying the interaction potential parameters, incidence angles, incident particle velocity and mass, surface particle mass, crystal orientation, surface temperature, lattice purity, and adsorbed particle coverage and mass are calculated and compared with experiment. Careful analysis of the model explains the origin of several observed trends in terms of the molecular dynamics.

A survey of classical mechanics is presented, and the relevant equations for the classical model are derived in Chapter II. In Chapter III a ten-body, 3D model is formulated and applied to investigate the (He/Ni) interaction. In Chapter IV this model is employed to study the effects of both the velocity distribution in the incident beam and surface temperature. The gas-solid model is extended in Chapter V to treat adsorbed particles and lattice impurities. The results are summarized, and

suggestions for future theoretical work in the area of gas-solid interactions are included in Chapter VI.

CHAPTER II

SURVEY OF CLASSICAL MECHANICS

Classical mechanics is the study of the laws governing the dynamics of macroscopic bodies. In many cases the same laws can successfully treat atoms and molecules, even though microscopic particles properly belong in the realm of quantum mechanics. The division between classical and quantum mechanics is not precise, but a rough criterion for the validity of classical mechanics is that the reduced wavelength of the particles be much less than the characteristic length in which the potential changes appreciably.[80] For molecular problems this length can be taken as the Bohr radius. Calculations then indicate that all particles with masses greater than hydrogen and with energies greater than 0.01 eV can be reasonably treated by classical mechanics.[81] Classical calculations on energy exchange in the gas phase and chemical reaction kinetics indicate that classical mechanics is, in fact, valid well into the domain of quantum mechanics, particularly when averaging of the results is appreciable.[82-84] Thus, the classical assumption for a gas-surface interaction model is reasonable and can be expected to give realistic results.

Since the gas-solid model of this work is based upon classical mechanics, it is appropriate to review the basic concepts that are useful in the treatment of atomic problems. Newton's Second Law applied to a system of N point particles gives

$$\left.\begin{aligned} M_i \ddot{X}_i &= F_{xi} \\ M_i \ddot{Y}_i &= F_{yi} \\ M_i \ddot{Z}_i &= F_{zi} \end{aligned}\right\} \quad i = 1, 2, \ldots, N, \qquad (6)$$

where X_i, Y_i, and Z_i are the Cartesian coordinates of the ith particle with mass M_i, and F_{xi}, F_{yi}, and F_{zi} are the three force components acting on the ith particle. By definition the kinetic energy T of the system is

$$T = \tfrac{1}{2} \sum_{i=1}^{N} M_i (\dot{X}_i^2 + \dot{Y}_i^2 + \dot{Z}_i^2). \qquad (7)$$

Partial differentiation with respect to $\dot{X}_i$ gives

$$\partial T / \partial \dot{X}_i = M_i \dot{X}_i . \qquad (8)$$

Taking the total time derivative of Eq. (8) yields

$$d/dt\,(\partial T / \partial \dot{X}_i) = M_i \ddot{X}_i . \qquad (9)$$

For conservative systems the potential energy V is defined by the relation

$$F_{xi} = - \partial V / \partial X_i . \qquad (10)$$

Combination of Eqs. (6), (9), and (10) and generalization to the Y and Z coordinates yields the Newtonian motion equations,

$$\left.\begin{aligned} \frac{d}{dt}\frac{\partial T}{\partial \dot{X}_i} + \frac{\partial V}{\partial X_i} &= 0 \\ \frac{d}{dt}\frac{\partial T}{\partial \dot{Y}_i} + \frac{\partial V}{\partial Y_i} &= 0 \\ \frac{d}{dt}\frac{\partial T}{\partial \dot{Z}_i} + \frac{\partial V}{\partial Z_i} &= 0 \end{aligned}\right\} i = 1, 2, \ldots, N. \qquad (11)$$

This system of 3N coupled, second-order differential equations determines the motion of the N-particle system.

The Newtonian equations are restricted to Cartesian coordinates. It is often more convenient to employ other coordinate systems to specify the configuration of a system. For this reason it is common to introduce the Lagrangian function,

$$L = T - V . \qquad (12)$$

Since T is a function of the particle velocities only, and V is assumed to be a function of the coordinates only, Eq. (11) can be written as

$$\left.\begin{aligned} \frac{d}{dt}\frac{\partial L}{\partial \dot{X}_i} - \frac{\partial L}{\partial X_i} &= 0 \\ \frac{d}{dt}\frac{\partial L}{\partial \dot{Y}_i} - \frac{\partial L}{\partial Y_i} &= 0 \\ \frac{d}{dt}\frac{\partial L}{\partial \dot{Z}_i} - \frac{\partial L}{\partial Z_i} &= 0 \end{aligned}\right\} i = 1, 2, \ldots, N. \qquad (13)$$

Newton's equations in this form can be shown to be valid for any choice of coordinate system. However, for the gas-solid model of this work, a Cartesian coordinate system is preferable, and it is unnecessary to transform to

generalized coordinates.

The system of 3N second-order differential equations represented by Eq. (13) can be transformed to a more readily solvable set of 6N first-order differential equations. Since V is a function of position only, the Cartesian momenta coordinates in the X direction can be written as

$$P_{X_i} = \partial T / \partial \dot{X}_i = \partial L / \partial \dot{X}_i . \tag{14}$$

Introducing this relation into Eq. (13) gives the system of equations,

$$\left.\begin{aligned} \dot{P}_{X_i} &= \partial L / \partial X_i \\ \dot{P}_{Y_i} &= \partial L / \partial Y_i \\ \dot{P}_{Z_i} &= \partial L / \partial Z_i \end{aligned}\right\} i = 1, 2, \ldots, N. \tag{15}$$

The second step in the transformation is introduction of the Hamiltonian function

$$H = \sum_{i=1}^{N} (P_{Xi}\dot{X}_i + P_{Yi}\dot{Y}_i + P_{Zi}\dot{Z}_i) - L. \tag{16}$$

For conservative systems this relation is equivalent to

$$H = T + V. \tag{17}$$

Total differentiation of the X components of Eq. (16) yields

$$dH = \sum_{i=1}^{N} \left(P_{Xi} d\dot{X}_i + \dot{X}_i dP_{Xi} - \frac{\partial L}{\partial X_i} dX_i - \frac{\partial L}{\partial \dot{X}_i} d\dot{X}_i\right). \tag{18}$$

Substitution of Eqs. (14) and (15) gives

$$dH = \sum_{i=1}^{N} (\dot{X}_i dP_{xi} - P_{xi} dX_i). \tag{19}$$

By regarding H as a function of X_i, Y_i, Z_i, P_{xi}, P_{yi}, and P_{Zi} one obtains the relations

$$\left.\begin{aligned} \frac{\partial H}{\partial P_{xi}} &= \dot{X}_i \quad \frac{\partial H}{\partial X_i} = -\dot{P}_{xi} \\ \frac{\partial H}{\partial P_{Yi}} &= \dot{Y}_i \quad \frac{\partial H}{\partial Y_i} = -\dot{P}_{Yi} \\ \frac{\partial H}{\partial P_{Zi}} &= \dot{Z}_i \quad \frac{\partial H}{\partial Z_i} = -\dot{P}_{Zi} \end{aligned}\right\} i = 1, 2, \ldots, N. \tag{20}$$

These are the 6N Hamiltonian equations of motion.

Solution of this system of coupled, first-order differential equations uniquely determines the motion of each of the N - particles. The requirements for solution are (a) the potential of the system as a function of the coordinates must be known so that H can be determined; (b) the 6N initial position and momenta coordinates must be specified, and (c) the 6N differential equations must be solvable, either analytically or numerically. In the following chapters models will be formulated in a manner that allows the Hamiltonian and the initial conditions to be specified. Then, numerical solution of Eq. (20) yields trajectories that are used to study the characteristics of gas-solid interactions.

CHAPTER III

THREE-DIMENSIONAL GAS-SOLID INTERACTION MODEL

A. Introduction

In this chapter the classical, 3D model originally suggested in Ref. 79 is formulated and employed to study the interaction of gaseous particles with a clean surface. Spatial distributions of reflected particles and ETC's are calculated as a function of incidence angle, gaseous beam velocity and temperature, surface temperature, gaseous atom mass, lattice force constant, and attractive well depth and curvature by numerical solution of the differential motion equations represented by Eq. (20). The 3D model removes the gross deviations of calculated scattering patterns from experiment that were found with the 2D model, and in general, semi-quantitative reproduction of existing molecular beam data is obtained. Section B outlines the mathematical formulation of the model. In Section C the results are given, discussed and, where possible, compared with experiment. The results and conclusions are summarized in Section D.

B. Formulation

Figure 1 illustrates the general outline of the 3D model employed to study the interaction process. The lattice face is assumed to consist of nine movable sites in the (x - y) plane indicated in Fig. 1 by the shaded circles. The gaseous atom, A, represented by the open circle, is incident on the lattice face at some random point, P, with initial velocity V_i at spherical polar incidence angles, θ_i and ϕ_i. The scattering occurs at spherical polar angles represented by θ_f and ϕ_f at a reflected velocity V_f. All particle motion is assumed to be classical.

In the surface model the nine movable lattice sites are connected to fixed sites by harmonic springs. The orientation of these fixed sites depends upon the crystal face being investigated. In the present work both the face-centered cubic (100) and (111) crystal planes have been studied. Figure 2 shows the arrangement employed to represent the (111) plane while Fig. 3 diagrams the arrangement of the (100) plane. In each case the movable lattice sites are represented by the symbol O while X indicates a fixed site in the (x - y) plane and ● a fixed site below the lattice surface.

As can be seen, the representation of the (111) plane contains 65 pairwise harmonic potentials while the (100) representation involves 60 such terms. The overall interaction potential, $\mathcal{V}$, for the system is constructed from a sum of the harmonic potential terms plus nine

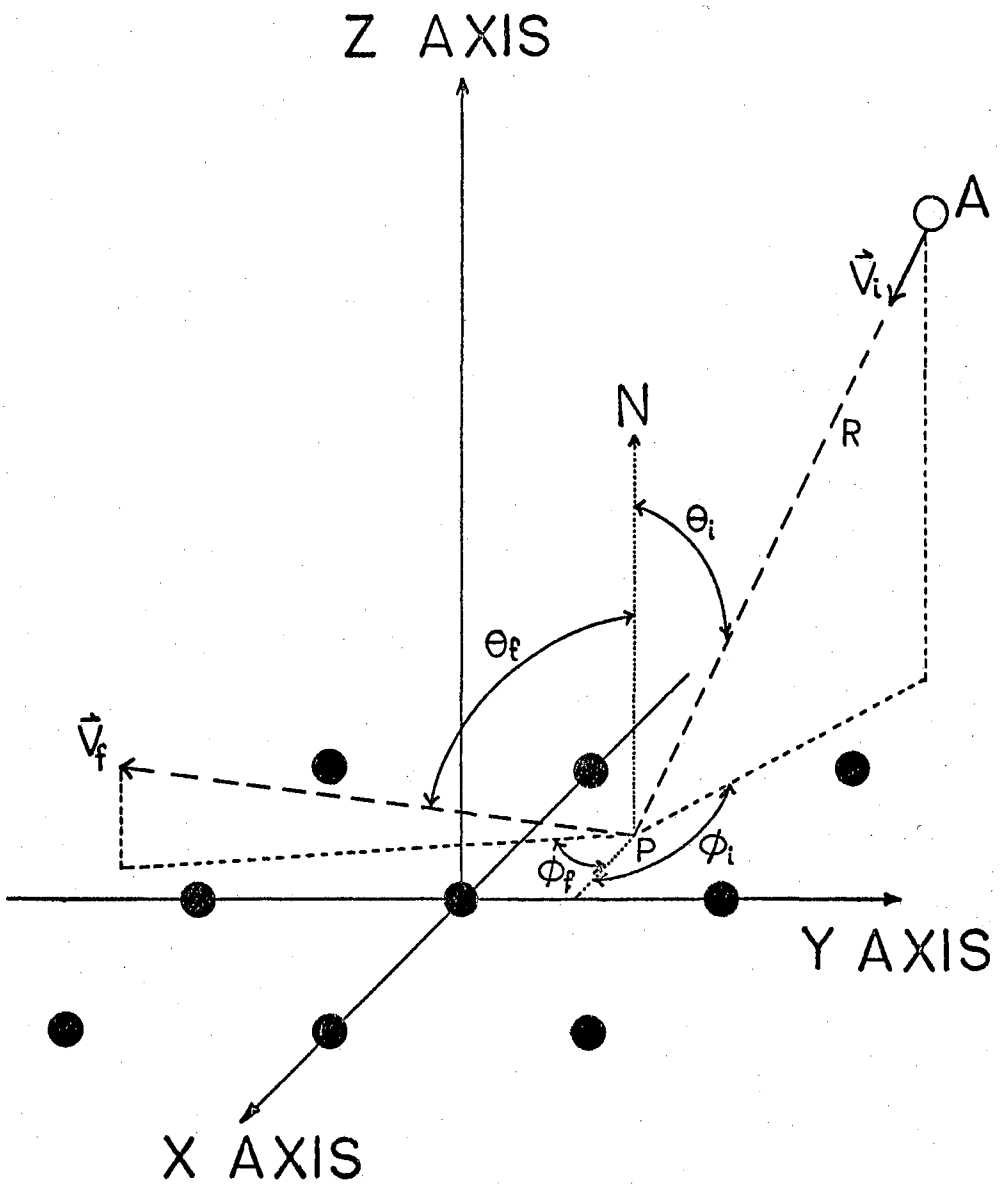

Figure 1. Three-Dimensional Gas-Solid Interaction Model for the (100) Crystal Plane.
● Represents a Movable Lattice Site.
O Represents the Incident Gaseous Atom.

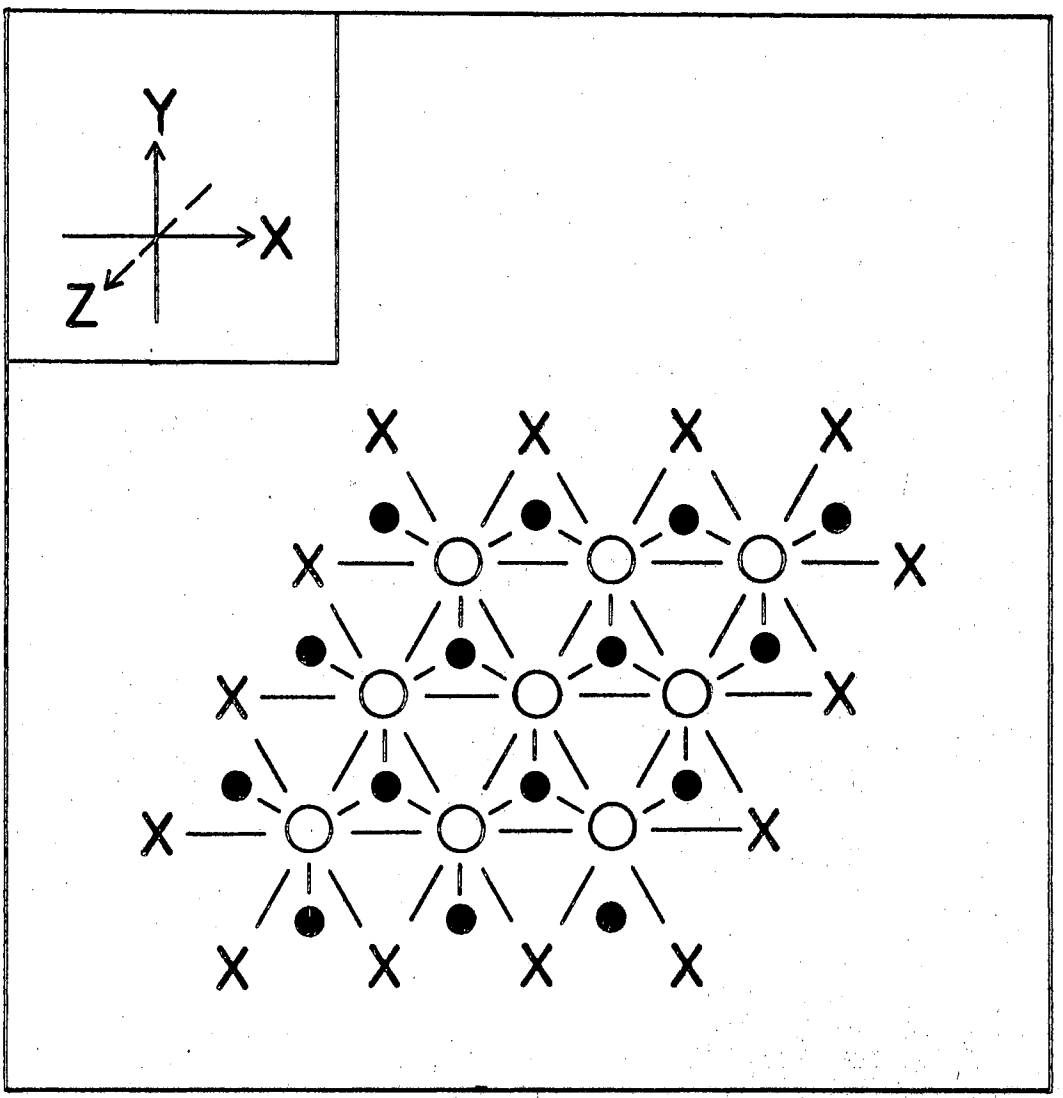

Figure 2. Model for the (111) Plane of Ni. O-Movable Lattice Site; X-Fixed Lattice Site in the Surface Plane; ● - Fixed Lattice Site Below the Surface Plane.

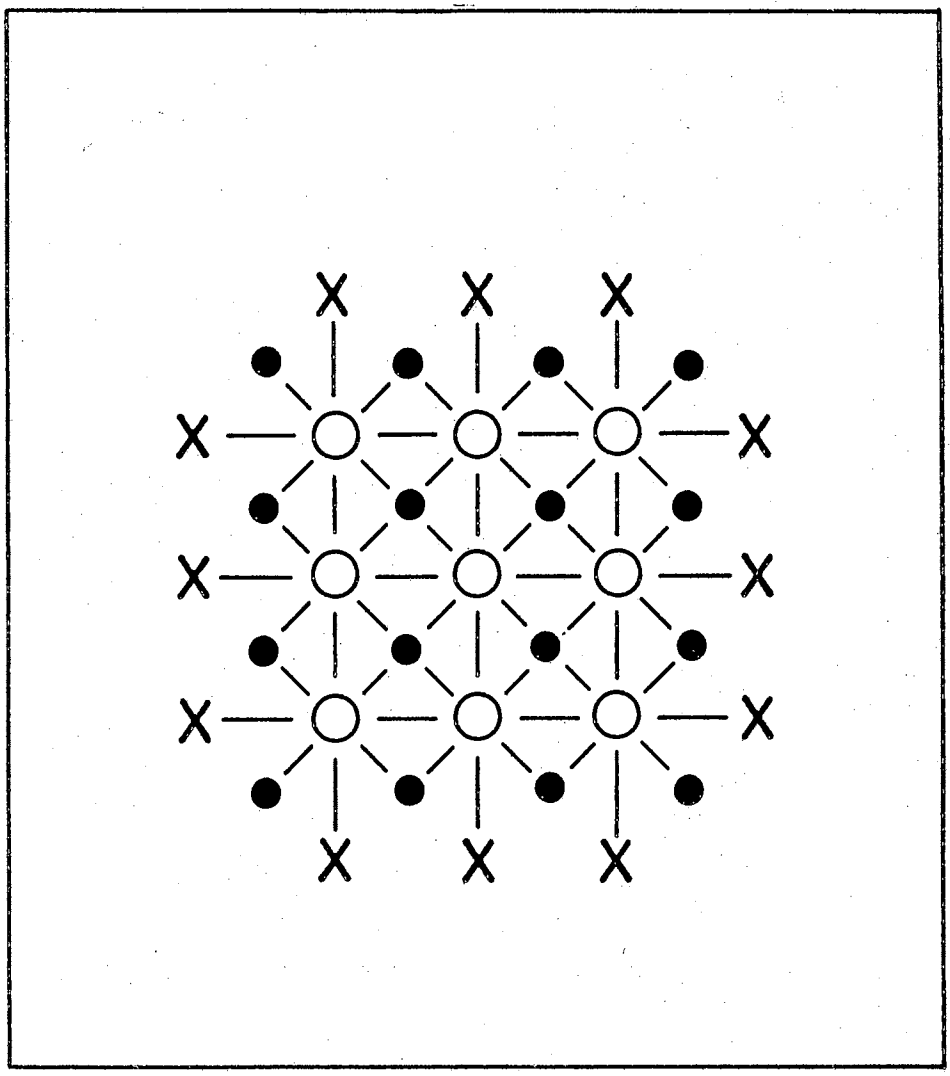

Figure 3. Model for the (100) Plane of Ni.

pairwise Morse type interaction terms operating between the incident gaseous atom and each movable lattice point. That is

$$\mathcal{V}_{111} = \sum_{i=1}^{9} V_{ia}^{M} + \sum_{j=1}^{65} V_{j}^{H} \tag{21}$$

and

$$\mathcal{V}_{100} = \sum_{i=1}^{9} V_{ia}^{M} + \sum_{j=1}^{60} V_{j}^{H} \tag{22}$$

where

$$V_{ia}^{M} = D[\exp\{-2\alpha(R_{ia} - Re)\} - 2\exp\{-\alpha(R_{ia}-Re)\}]$$

and

$$V_{j}^{H} = (k/2)(R_j - R_e^{1})^2. \tag{23}$$

In the above, R_{ia} represents the interparticle distance between movable lattice site i and gaseous atom A, R_j the interparticle distance in the harmonic pair potential denoted by V_j^H, Re^1 the equilibrium lattice spacing, while D, Re, and α are parameters of the Morse interaction potential, V_{ia}^{M}.

The system motion is determined from the Hamiltonian equations given by Eq. (20) with i = 1, 2, . . ., 9, and A. The required 3D Hamiltonian has the form:

$$H = \tfrac{1}{2}\sum_{i} [P_{x_i}^{2} + P_{y_i}^{2} + P_{z_i}^{2}]/M_i + \mathcal{V} \tag{24}$$

for i = 1, 2, 3, . . . 9, and A. Thus, in the classical, 3D gas-surface model the motion is determined by the solution of the 60 coupled differential equations represented

by Eq. (20).

The solution requires the specification of all initial position and momentum coordinates for lattice points 1-9 and for atom A. The initial lattice coordinate selection for the (100) plane was performed according to the following prescription:

$$Z_i = 0 \quad \text{for } i = 1, 2, \ldots 9 \tag{25a}$$

$$X_4 = X_5 = X_6 = 0 \tag{25b}$$

$$X_7 = X_8 = X_9 = Re^1 \tag{25c}$$

$$X_1 = X_2 = X_3 = -Re^1 \tag{25d}$$

$$Y_3 = Y_4 = Y_9 = Re^1 \tag{25e}$$

$$Y_2 = Y_5 = Y_8 = 0 \tag{25f}$$

and

$$Y_1 = Y_6 = Y_7 = -Re^1 . \tag{25g}$$

The modification Eqs. (25a) - (25g) required to represent the (111) plane is obvious from Fig. 2.

The initial lattice momenta selection is performed as follows for both crystal planes;

$$P_{X_i} = [2M_i \bar{k} T_s]^{\frac{1}{2}} [-1]^{r_i}$$

$$P_{Y_i} = [2M_i \bar{k} T_s]^{\frac{1}{2}} [-1]^{r_i{}^1} \qquad i = 1, 2, \ldots 9 \tag{26}$$

and

$$P_{Z_i} = [2M_i \bar{k} T_s]^{\frac{1}{2}} [-1]^{r_i{}^{11}} ,$$

where $\bar{k}$ is Boltzmann's constant, T_s the surface temperature and r_i, $r_i{}^1$, and $r_i{}^{11}$ are randomly chosen integers, either

even or odd. Equations (25a) - (25g) place each lattice site initially at its equilibrium position so that all initial lattice energy is kinetic. Equation (26) then equipartitions, in a random manner, the lattice energy, $3\bar{k}T_s$, between the three available momentum components of each lattice atom.

The initial variables for the gaseous atom are given by

$$\begin{aligned} X_a &= R \sin\Theta_i \cos\phi_i \\ Y_a &= R \sin\Theta_i \sin\phi_i \\ Z_a &= R \cos\Theta_i \\ P_{x_a} &= M_a V_i \sin\Theta_i \cos\phi_i \\ P_{y_a} &= M_a V_i \sin\Theta_i \sin\phi_i \end{aligned} \tag{27}$$

and $$P_{z_a} = M_a V_i \cos\Theta_i,$$

where R is the initial distance from atom A to the aiming point P on the surface. The initial value for R is chosen as

$$R = \frac{8\,\text{Å}}{\cos\Theta_i} + \mathcal{Z}^1 V_i \tau_p \tag{28}$$

where $\mathcal{Z}^1$ represents a number such that $0 \leq \mathcal{Z}^1 \leq 1$, and τ_p is the vibration period of the lattice, i. e.

$$\tau_p = 2\pi(\mu/k)^{\frac{1}{2}}. \tag{29}$$

In effect, the specification of $\mathcal{Z}^1$ determines the initial lattice-phase angle. These choices completely specify

the initial state of the system.

A trajectory is considered to have been completed whenever, after striking the surface, particle A finds itself once again at a distance R from the surface. At this point the integration of Eq. (20) is terminated, and the final variables of interest are calculated. These variables include the scattering angles Θ_f, which is given by

$$\Theta_f = \cos^{-1}[P_{za}/(P_{za}^2 + P_{ya}^2 + P_{xa}^2)^{\frac{1}{2}}], \qquad (30)$$

and ϕ_f, which is given by

$$\phi_f = \tan^{-1}[P_{ya}/P_{xa}], \qquad (31)$$

and the ETC which is defined to be

$$\alpha_E(\Theta_i, \phi_i) = (E_g^i - E_g^f)/E_g^i. \qquad (32)$$

The initial and final energies appearing in Eq. (32) can be obtained from

$$E_a = (P_{xa}^2 + P_{ya}^2 + P_{za}^2)/2M_a \qquad (33)$$

since the potential energy of A will be essentially zero whenever A is located a distance R from the surface.

C. Results and Discussion

1. Numerical Analysis

The integration of the motion equations represented by Eq. (20) was accomplished using a variable step, Adams-Moulton (AM) procedure[85] on an IBM 7040. Since the AM method is not self-starting, a Runga-Kutta program was employed to provide the initial points required. Whenever there was no lattice energy initially present

(i. e., $T_s = 0.0^\circ K$), the integration step size was varied and made as large as possible consistent with the criteria of energy conservation and coordinate consistency. Under these conditions each trajectory took an average of about 60 sec of machine time. For trajectories in which $T_s \neq 0^\circ K$, variation of step size helped very little since the requirement that lattice energy be conserved kept the step size small throughout the integration. For this reason a fixed step was employed in trajectories of this type, and the machine time required consequently increased to about 120 sec/trajectory.

The need for properly averaging over vibrational phase and aiming point has previously been pointed out in Ref. 79 where such averaging was carried out by a random Monte Carlo process. To conserve machine time this procedure has been replaced by a systematic averaging over Z^1 in Eq. (28) and over surface aiming points. The averaging over aiming points was accomplished by scanning over the unit cell with approximately 50 trajectories. For example, in Fig. 4 the unit cell is shown as the area within the rhombus. The 49 small boxes indicate the aiming point areas employed for the specific case of $\phi_i = 0^\circ$ on the (111)plane. Within each small box the aiming point was randomly selected. The results for aiming points within the unit cell not covered by boxes can be obtained by reflection symmetry. The statistical convergence of the results was checked by examining additional trajectories in specific cases. In

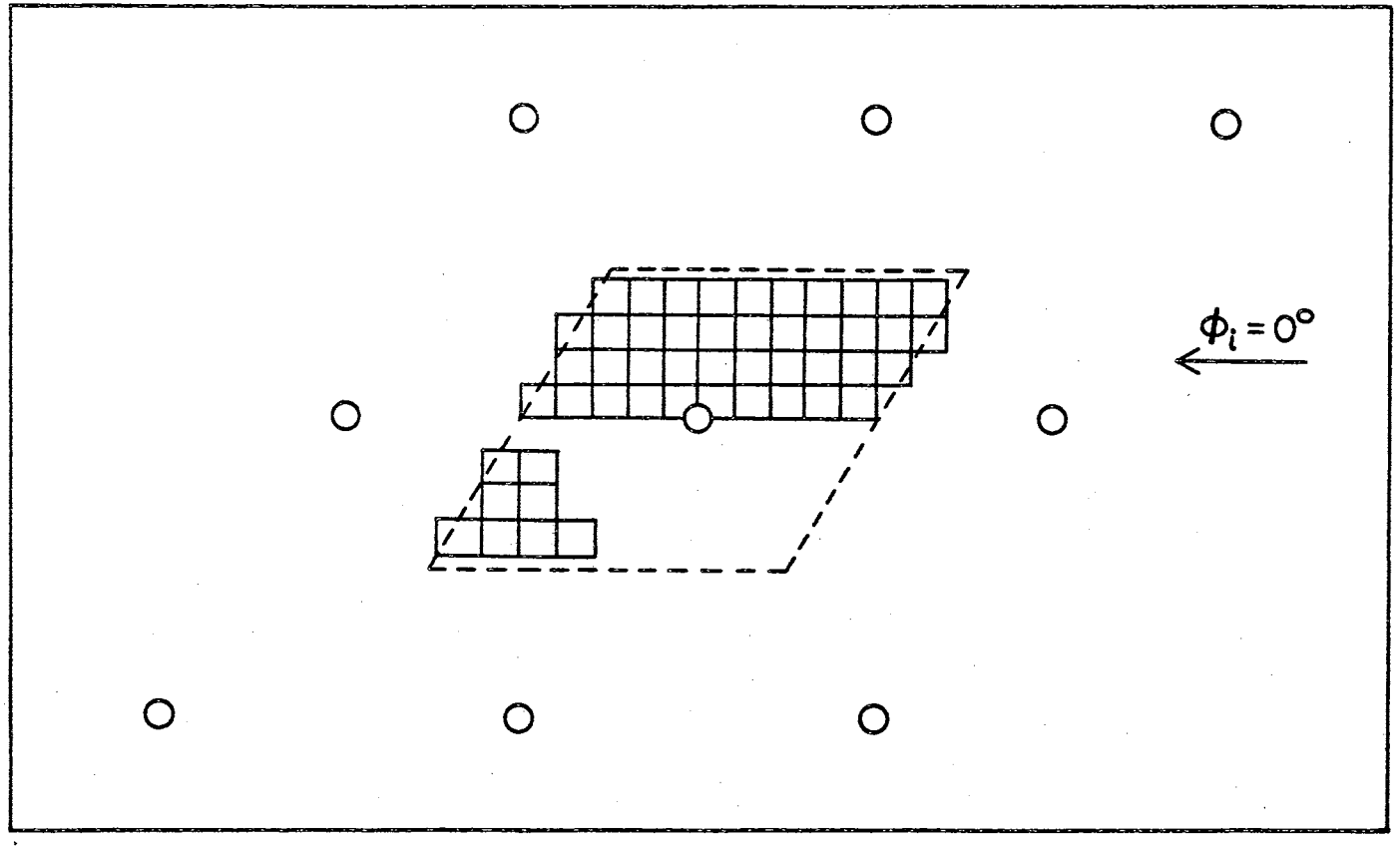

Figure 4. "Aiming Point" Regions on the (111) Ni Surface.

general, it was found that all major features were essentially unaltered by an increase in the size of the statistical sample.

2. The Potential Surface

The (He/Ni) system was chosen as the basis for the present calculations. The specific choice of a particular system is not extremely important here since the principal aim has been an investigation of the dependence of the scattering and ETC on various parameters. Reproduction of experimental data for any one particular system would require accurate values of the interaction potential parameters. Unfortunately, these are not available. The choice of the (He/Ni) system, however, does allow for a comparison of the present results with those obtained by Oman, Bogan, and Li[74] and with those of Ref. 79.

The interaction potential represented by Eqs. (21), (22), and (23) requires the specification of five parameters: D, α, Re, k, and Re^1. The significance of k and Re^1 has been discussed previously. The magnitude of the attractive well depth in an interaction between a surface atom and He is represented by D; α is related to the curvature of the attractive well; Re defines the position of the well with respect to the surface atom. The values of D, α, k, and Re^1 are taken from the work of Goodman[46] while the value of Re is obtained from the Lennard-Jones (12-6) parameters employed by Oman, Bogan, and Li.[74] The

values used, which are the same as those of Ref. 79, are summarized in Table I.

TABLE I

(He/Ni) POTENTIAL SURFACE PARAMETER VALUES

Surface Parameter	Value
D	0.00564 eV
α	1.6 $\mathring{A}^{-1}$
Re	3.11 $\mathring{A}$
k	5.36 eV/$\mathring{A}^2$
Re^1	3.517 $\mathring{A}$

If the lattice atoms are held fixed in their equilibrium positions, contour maps of the potential surface representing the (He/Ni) interaction can be plotted. Figure 5 shows a comparison of the 2D contour lines obtained in Ref. 79 and the 3D contour lines obtained from the present model. The shaded area shown in the inset illustrates the portion of the surface being considered. Solid lines represent the three dimensional contour lines while the dashed curves represent the 2D surface. As can be seen, two major differences are present:

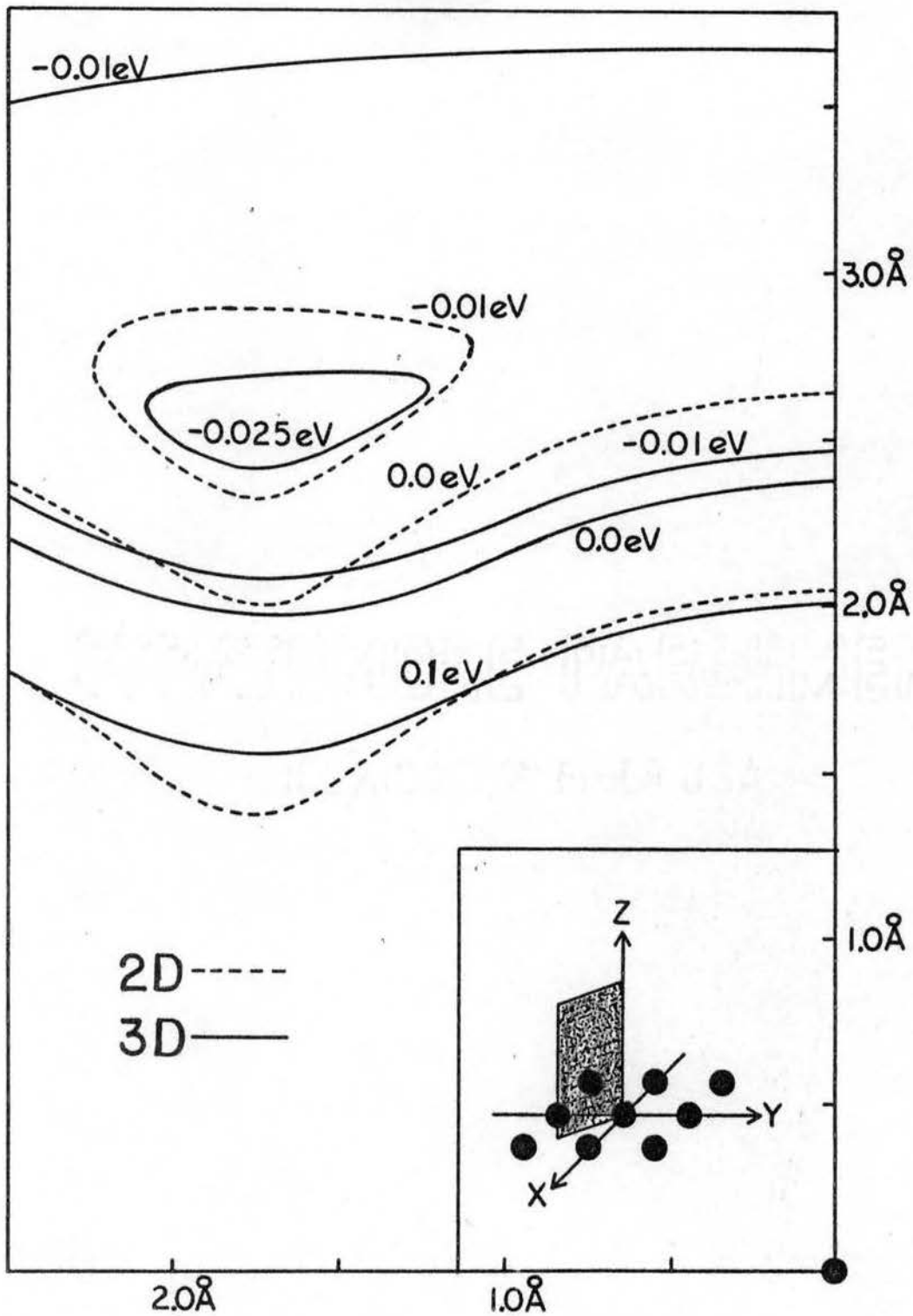

Figure 5. Comparison of 2D and 3D (He/Ni) Potential Contour Lines.

(a) Corresponding contour lines for the 3D case exhibit less curvature than that present on the 2D surface. For other planes through the lattice the difference is smaller.

(b) The well depth is a factor of 2.5 larger on the 3D surface than for the 2D case. This increased well depth, which results from a multi-dimensional model, can have significant consequences. For example, an examination of the surfaces for (Ar/Ni) using Goodman's[46] Morse parameters shows that the 3D well depth is -0.41 eV while that for the 2D surface is only -0.11 eV. These are the parameters employed by Oman, Bogan, and Li[74] in their 3D calculations which predict that Ar atoms at incident energies of 0.125 eV and 0.5 eV are almost completely trapped. This discrepancy with experiment would seem not to result from the model itself, but rather from the parameters which "fit" an over-simplified, 1D type interaction model to experimental data. Further significances of these differences are pointed out in Sections C.3. and C.4.

3. Energy Transfer

The dependence of $\alpha_E(\Theta_i, \phi_i)$ upon incidence angle, various Morse interaction parameters, atomic mass, out-of-plane scattering angle, aiming point, surface temperature, and lattice-vibrational-phase angle have all been examined. In general, the results are in reasonable agreement with those obtained for the 2D lattice of Ref. 79.

Such agreement is not unexpected since it has previously been shown that 2D models reproduce energy transfer and petitioning data reasonably well.[86]

Figure 6 shows the variation of $\alpha_E(\Theta_i, 0^\circ)$ with Θ_i on the (111) plane of Ni for a surface temperature of 0°K and an incident velocity of 1.12 x 10^5 cm/sec, the most probable He velocity for a beam effusing from a gas at 170°K. Each calculated point was obtained by averaging the results of 49 trajectories that scan over surface aiming points in the manner previously described. As can be seen, the ETC is a rapidly decreasing function of Θ_i in semi-quantitative agreement with the experimental results of Devienne, Souquit and Roustan.[87] The present calculations further indicate that $\alpha_E(\Theta_i, 0^\circ)$ is a more rapidly decreasing function of Θ_i than previously indicated by the 2D results of Ref. 79, which are shown as the solid line of Fig. 6. This behavior then lends stronger support to the "normal-component model" proposed by Datz, Moore, and Taylor[36] and explicitly assumed by Logan and Stickney[70] and by Keck and Logan[71] than that provided by the 2D results. In fact, $\alpha_E(\Theta_i, 0^\circ)$ very nearly approaches zero as $\Theta_i \to 90^\circ$ indicating that the energy present in the normal momentum component is by far the dominate factor in determining the ETC.

In essence the behavior illustrated in Fig. 6 is a manifestation of the decreased curvature of the surface contour lines shown in Fig. 5. That is, the x or y

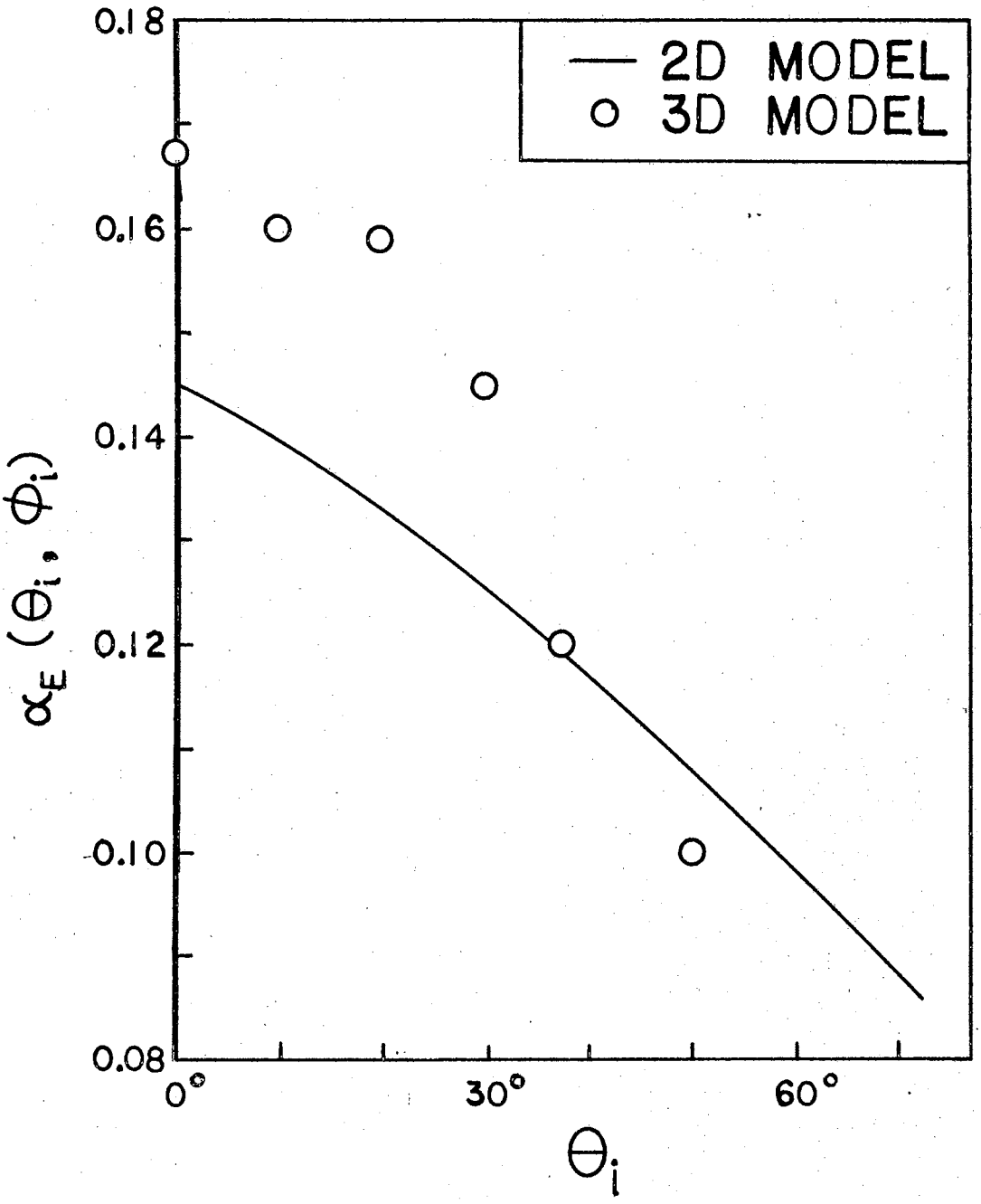

Figure 6. Variation of $\alpha_E(\theta_i, \phi_i)$ With θ_i.

components of force exerted on the gaseous atom depend upon $(\partial V/\partial x)$ and $(\partial V/\partial y)$ respectively, and both of these derivatives are smaller for the 3D surface than for the 2D case. Consequently, energy transfer from the parallel momentum components becomes smaller, resulting in the behavior shown in Fig. 6.

The variation of $\alpha_E(\theta_i,\phi_i)$ with the Morse interaction parameter D and with the lattice force constant k are as indicated in Ref. 79. A monotonic increase of the ETC with increasing attractive well depth and with decreasing lattice force constant is calculated. This behavior is in qualitative agreement with the available experimental data of Thomas[14] and Wachman[20]. Figures 7 and 8 show the calculated variation of $\alpha_E(\theta_i,\phi_i)$ with D and k respectively for E_g^i = 0.0258eV, $\theta_i = 0^\circ$, $\phi_i = 0^\circ$, and $T_s = 0^\circ K$. Each calculated point represents an ensemble average over surface aiming points as described above.

The dependence of $\alpha_E(\theta_i,\phi_i)$ upon the steepness of the repulsive potential wall has been investigated by varying the Morse parameter, α, of Eq. (23). Essentially, α determines the curvature of the attractive well. As α increases, the curvature increases, and consequently the repulsive wall becomes steeper. In the limit as $\alpha \to \infty$ a hard sphere interaction is approached.

Figure 9 shows the variation of $\alpha_E(\theta_i,\phi_i)$ with α on the (111) face of Ni for $\theta_i = 37.5^\circ$, $\phi_i = 0^\circ$, $T_s = 0^\circ K$,

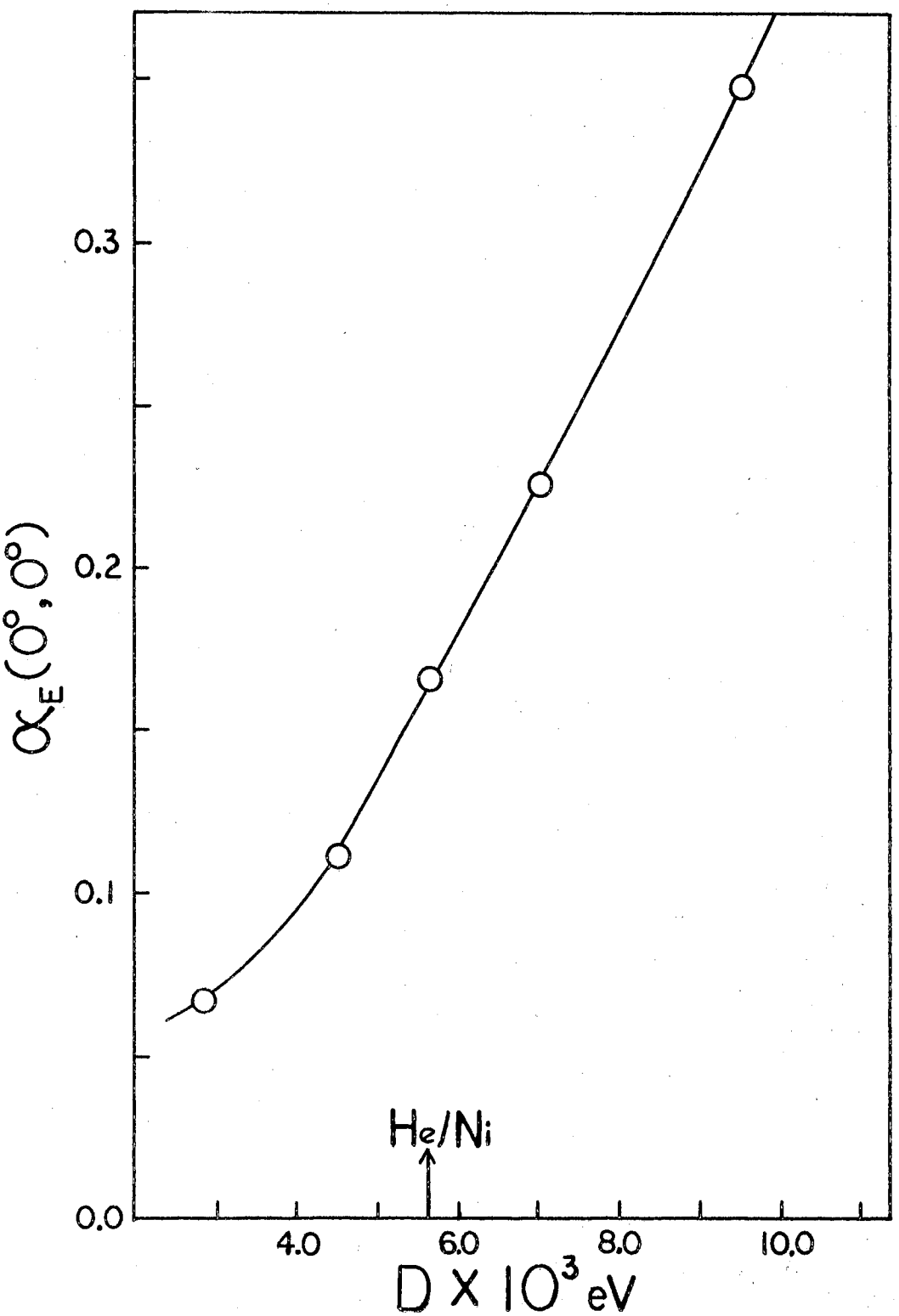

Figure 7. Variation of $\alpha_E(\Theta_i,\Phi_i)$ With Morse D Parameter.

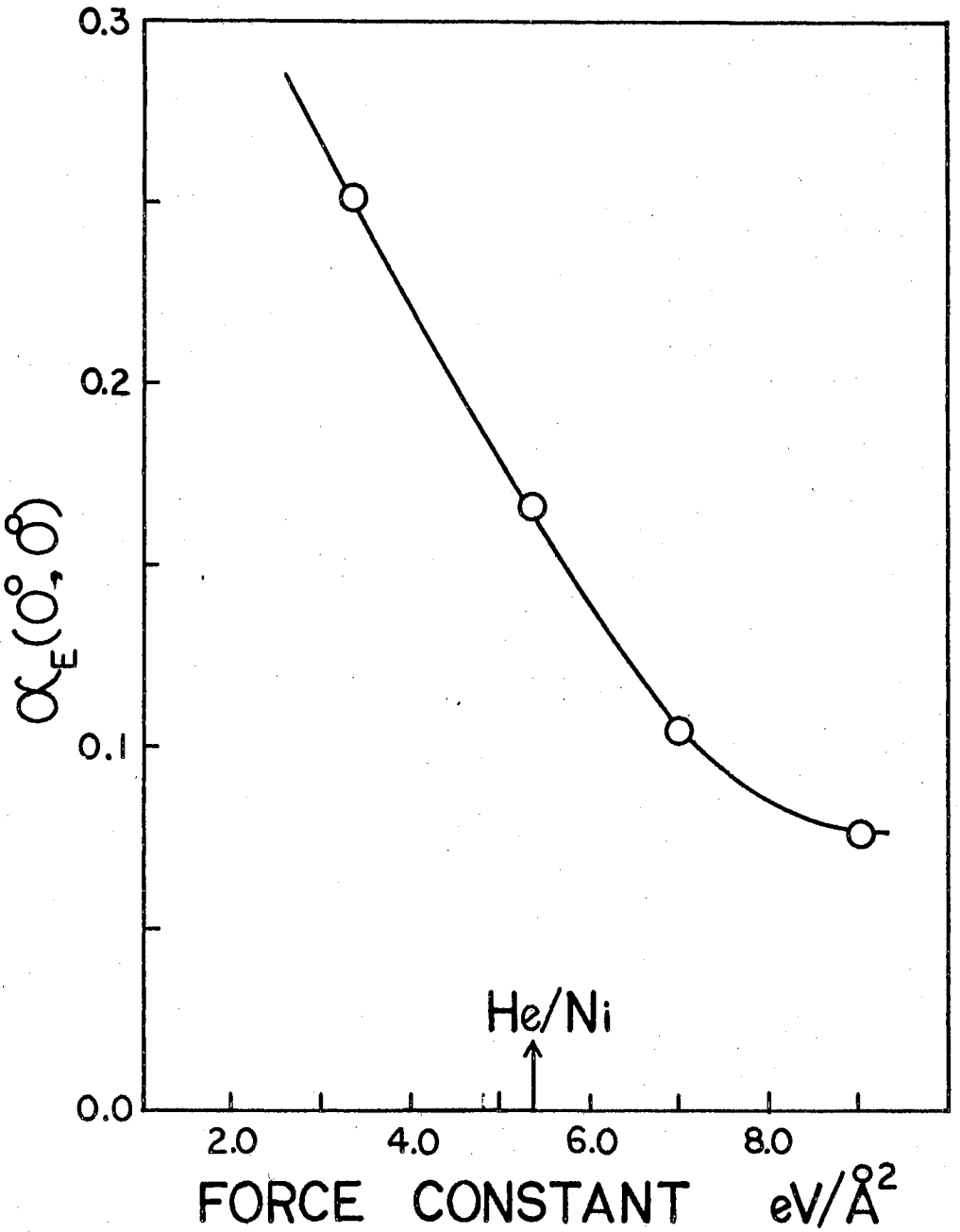

Figure 8. Variation of $\alpha_E(\theta_i,\phi_i)$ With Lattice Force Constant.

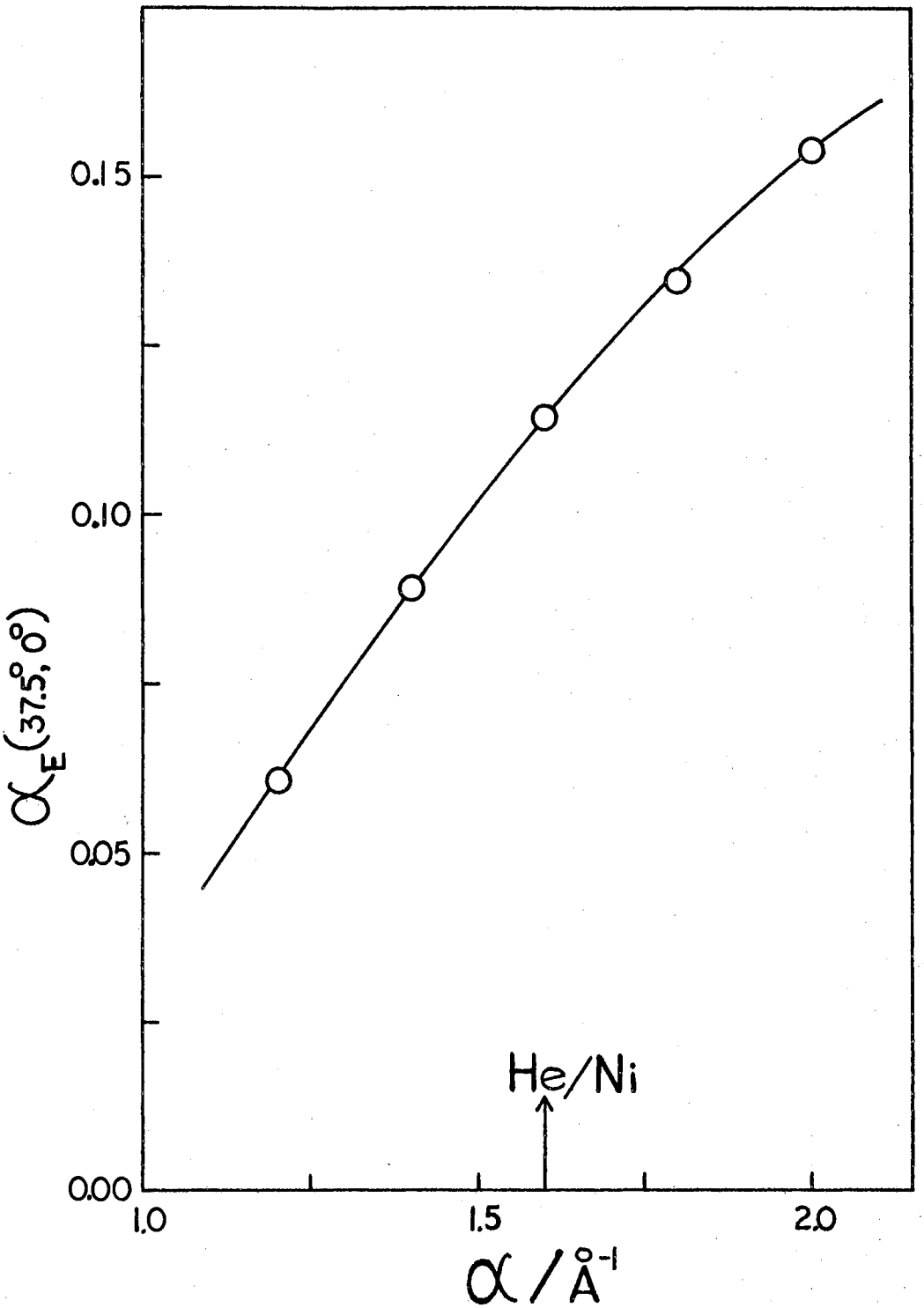

Figure 9: Variation of $\alpha_E(\theta_i, \phi_i)$ with Morse α Parameter.

and $V_i = 1.58 \times 10^5$ cm/sec, the most probable velocity for a beam of He effusing from a gas at 339°K. As can be seen, $\alpha_E(\theta_i,\phi_i)$ is a monotonically increasing function of α. The arrow in Fig. 9 indicates the value used to represent the (He/Ni) interaction. These results seem to imply that hard sphere, impact models will, in general, tend to overestimate the extent of energy transfer unless modified in some compensating manner.

The extent of energy transfer has been found to be virtually independent of the crystal face employed. For example, the average value of $\alpha_E(\theta_i,\phi_i)$ for $\theta_i = 37.5°$, $\phi_i = 0°$, $V_i = 1.12 \times 10^5$ cm/sec, and $T_s = 0°$K was calculated to be 0.11 for the (100) face of the Ni crystal while a value of 0.12 was obtained when the (111) representation was used.

The detailed interdependence of $\alpha_E(\theta_i,\phi_i)$, aiming point, and scattering angles θ_f and ϕ_f has been examined on the (111) crystal face with $\theta_i = 37.5°$, $\phi_i = 0°$, $V_i = 1.12 \times 10^5$ cm/sec, and $T_s = 0°$K. The general results are shown in Fig. 10, which illustrates the resulting values of $\alpha_E(\theta_i,\phi_i)$, θ_f, and ϕ_f for an ensemble of trajectories aimed at various points within the shaded region shown in the upper inset. The origin of each vector shown represents the aiming point of the trajectory; the direction of the vector gives the out-of-plane scattering angle ϕ_f, where a horizontal position indicates $\phi_f = 180°$; the

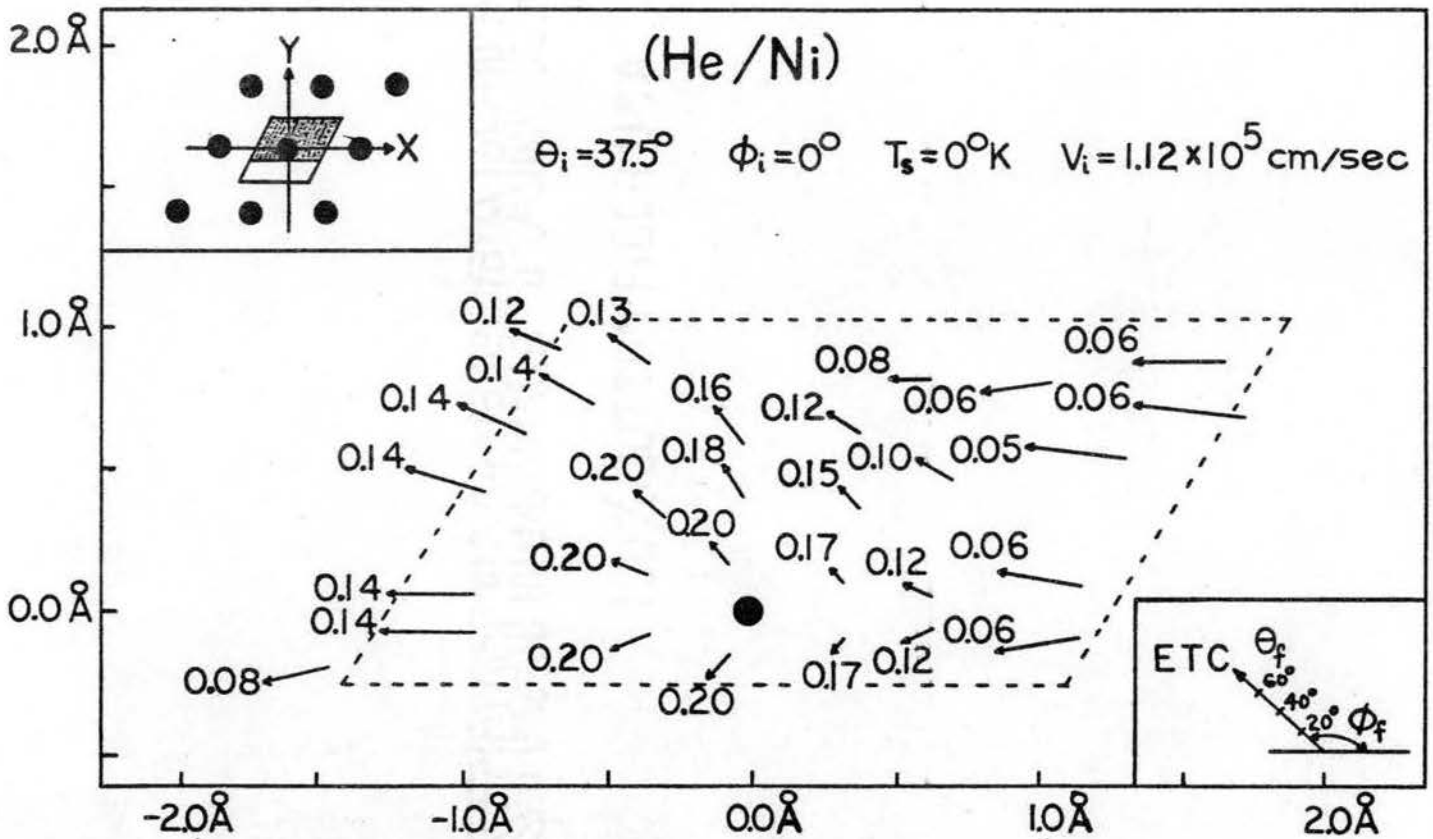

Figure 10. Interdependence of Aiming Point, θ_f, ϕ_f, and $\alpha_E(\theta_i, \phi_i)$. Upper Inset Shows Region of the (111) Surface Being Examined. Lower Inset Gives the Scale of θ_f and ϕ_f Values in Terms of Vector Length and Direction, Respectively.

length of the vector gives Θ_f according to the scale shown in the lower inset; and the numerical value listed at the head of each vector is the computed value of $\alpha_E(\Theta_i, \phi_i)$ for that trajectory. Several general features make themselves apparent in this figure:

(a) Atoms aimed near a lattice site are generally reflected at near normal Θ_f angles and are associated with large values for the ETC.

(b) Atoms aimed at points between lattice sites tend to exhibit large scattering angles Θ_f and considerably smaller transfer coefficients. These results are in accord with the experimental observations of Hinchen and Malloy[26] who found that the velocity of atoms scattered in the normal direction was less than that for atoms reflected near the surface.

(c) Most trajectories will result in "in-plane" scattering (i.e. $\phi_f \cong 180^\circ$).

(d) Energy transfer coefficients tend to increase as ϕ_f moves away from the "in-plane" angle. More detailed investigation indicates that this effect varies in magnitude between a 50-100% increase depending upon the conditions.

It should be noted that the above results indicate that serious distortions may result from employing models which require direct impact upon a lattice site. The inapplicability of such models to scattering has already been pointed out in Ref. 79. The results of Fig. 10

suggest that a similar situation may exist with regard to energy transfer.

Calculations of $\alpha_E(\theta_i,\phi_i)$ at different ϕ_i angles indicate that the energy transfer coefficient is essentially independent of ϕ_i. Thus, when $\alpha_E(\theta_i,\phi_i)$ was examined on a (111) Ni face with $\theta_i = 37.5^\circ$, $V_i = 1.12 \times 10^5$ cm/sec, and $T_s = 0^\circ K$, an average value of 0.12 was obtained for both $\alpha_E(\theta_i,0^\circ)$ and $\alpha_E(\theta_i, 45^\circ)$. Direct comparison of this result with experiment is impossible due to the lack of velocity-selected, molecular beam data.

The dependence of $\alpha_E(\theta_i,\phi_i)$ upon isotopic mass of the gaseous atom has been investigated by a series of calculations employing ^3He as the gaseous atom. The results are shown in Fig. 11 as a function of incident gaseous energy E_g^i. Curves 1 and 2 represent calculated $\alpha_E(\theta i,\phi i)$ values on the (111) crystal face for ^4He and ^3He respectively with $\theta_i = \phi_i = 0^\circ$ and $T_s = 0^\circ K$. For higher incident energies one has $[\alpha_E(\theta_i,\phi_i)]_{^4He} > [\alpha_E(\theta_i,\phi_i)]_{^3He}$ with the calculated ratios varying between 1.0 and 1.30. At low incident energy an inversion of the above inequality is predicted with the general curve shape exhibiting what might be termed a "turn-up" phenomenon, which was not observed in the 2D calculations of Ref. 79. The crossover of the ^3He and ^4He curves and the "turn-up" are manifestations of the deeper attractive well depth of the 3D surface

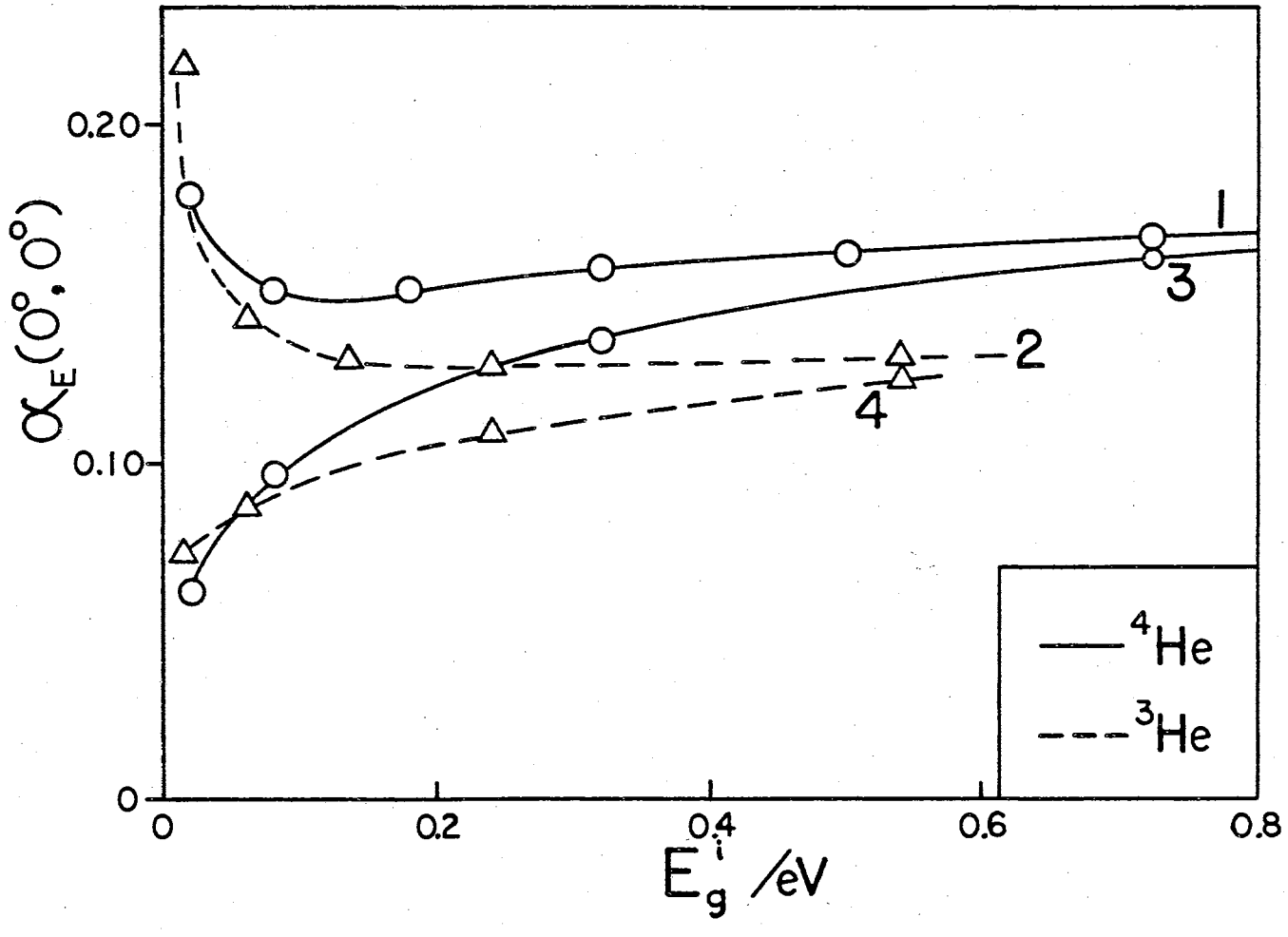

Figure 11. Variation of $\alpha_E(\theta_i,\phi_i)$ With Gaseous Atom Mass and E_g^i. Curves 1 and 2 are for D = 0.00564eV. Curves 3 and 4 have D = 0.00282eV.

mentioned above. This is shown clearly in curves 3 and 4 of Fig. 11, which illustrate the behavior of $\alpha_E(\theta_i,\phi_i)$ for ^4He and ^3He respectively when the well depth parameter D is reduced from 0.00564 eV to 0.00282 eV. As can be seen, no "turn-up" occurs, and the general character of the results approaches those reported in Ref. 79.

Since the attractive well accelerates the gaseous atom as it approaches the surface, its presence will increase the magnitude of the energy transfer which forms the numerator of Eq. (32). This accelerating effect will be greater on ^3He than on ^4He due to the mass difference, hence a crossover occurs between the two curves at low incident energy. The "turn-up" phenomenon results for much the same reason. The presence of the well prevents the numerator of Eq. (32) from approaching zero as E_g^i approaches zero. Thus, the mathematical form of Eq. (32) insures such a "turn-up" phenomenon. As the well depth decreases, the magnitude of this effect decreases, and the curve shapes revert to that shown by curves 3 and 4 of Fig. 11. It should be noted that curves 3 and 4 approach curves 1 and 2 at large E_g^i values since attractive well effects become negligible at large incident energy.

A partial comparison of the calculated isotope effect with experiment is possible. Thomas and Krueger[14] have measured isotope effects on the thermal accommodation coefficient for a (He/W) system and find that $\alpha_T(^4He)/\alpha_T(^3He) = 1.09$ for a temperature of 308°K. Further

investigation on (He/K) systems indicates that the above ratio tends to decrease as the gaseous temperature decreases.[14] Such behavior is clearly in line with that predicted by the results shown in Fig. 11 where the ratio $\alpha_E(^4He)/\alpha_E(^3He)$ decreases as E_g^i decreases. Although a one-to-one correspondence does not exist between the thermal accommodation and energy transfer coefficients, it is interesting to note that the direction of the experimental isotope effect in the (He/W) system is the same as that calculated for the (He/Ni) system. To this extent the results can be said to agree with experiment.

Figure 12(a) shows the calculated variation of $\alpha_E(\theta_i,\phi_i)$ with T_s on the (111) Ni face for both $\theta_i = 0^\circ$ and $\theta_i = 50^\circ$ with $\phi_i = 0^\circ$ and $V_i = 1.12 \times 10^5$ cm/sec. As can be seen, there is little change in the predicted behavior between 2D and 3D models. The 3D points cannot be expected to fall directly on the 2D line since the surface details differ. The important features, however, are identical. The ETC is a strong function of T_s indicating clearly that models which ignore lattice energy must be viewed with caution. As T_s becomes greater than T_g, the ETC becomes negative indicating that, on the average, energy is being transferred from the lattice to the gaseous atom.

The 3D, $\alpha_E(\theta_i,\phi_i)$ curves of Fig. 12(a) can be converted to effective energy accommodation coefficients by the relation

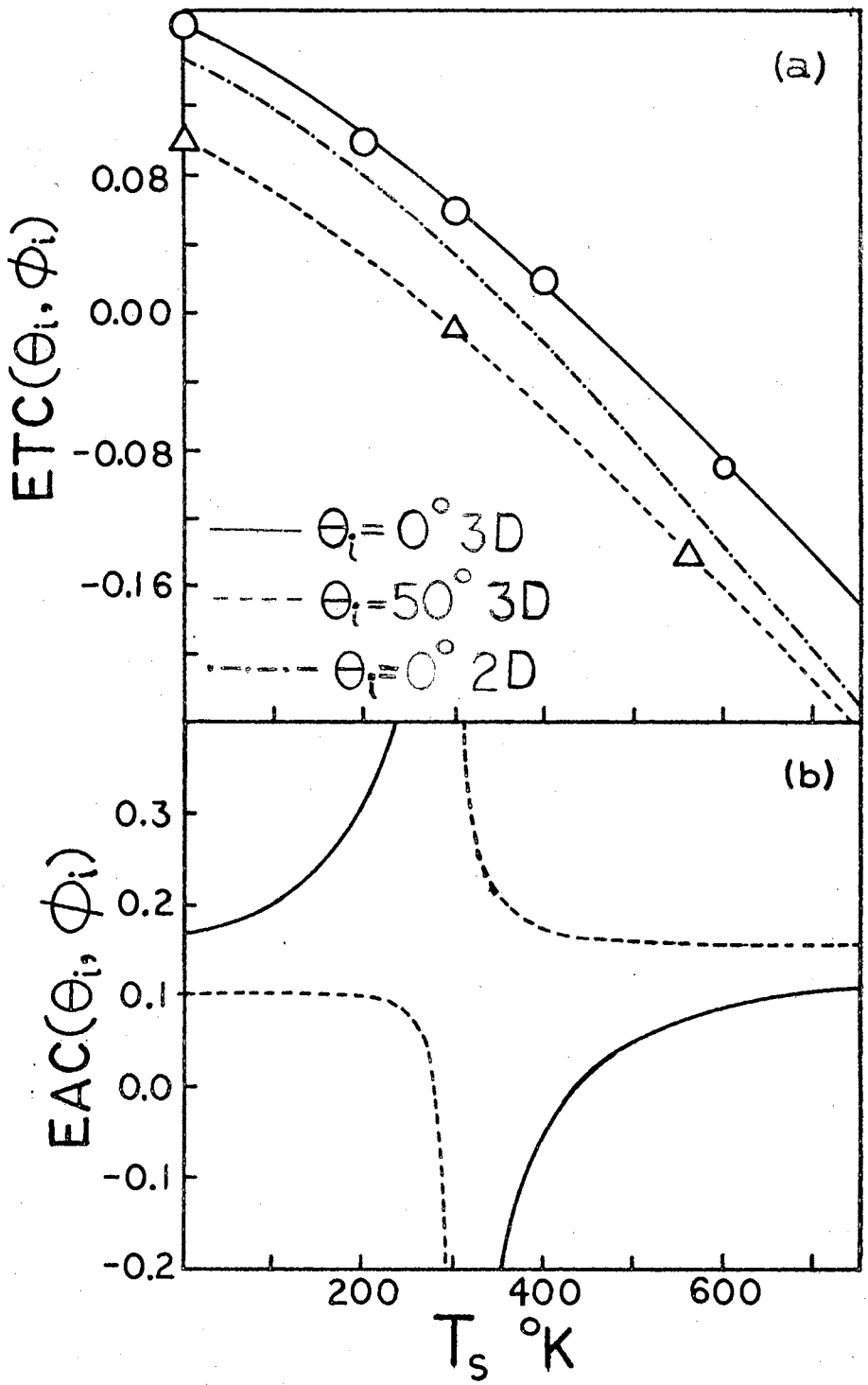

Figure 12: (a) Variation of $\alpha_E(\theta_i, \phi_i)$ With T_s. (b) Variation of EAC (θ_i, ϕ_i) With T_s.

$$EAC(\theta_i,\phi_i) = \alpha_E(\theta_i,\phi_i)/(1-E_s/E_g^i) \qquad (34)$$

where E_s is the energy of a gaseous particle at the temperature of the surface. In Fig. 12(b) the variation of these energy accommodation coefficients with T_s is shown. The curve for EAC (50°, 0°) agrees qualitatively with the experimental results of Hinchen and Malloy[26] for an (Ar/Pt) system with $\theta_i = 67.5^\circ$. Because of the higher polarizability of Ar, the curve for (Ar/Pt) is understandably shifted towards higher EAC values in accord with Fig. 7. The presence of the discontinuity and infinity at $T_g = T_s$ indicates that for molecular beam experiments an ETC, which is both well-behaved and continuous at all points, is the most convenient quantity to measure and calculate. This differs from the case of thermal conductivity cells where equilibrium exists, and the AC necessarily approaches a limit as $(T_s - T_g)$ approaches zero. It is interesting to note that integrating the results of Fig. 12(b) over all incident angles and velocities would give a result representative of conductivity cell measurements. If one approximates the velocity integration by the use of the most probably velocity, the angular integration of the results shown in Fig. 12(b) would give an EAC of approximately 0.15 that would then be essentially independent of T_s. The conductivity cell measurements of Thomas and Schofield[88] and Menzel and Kouptsidis[17] have shown the AC for (He/W) to be independent of $(T_s - T_g)$.

It should be pointed out that proper averaging over lattice phase is essential whenever $T_s \neq 0^\circ K$. This is clearly shown in Fig. 13 where the variation of $\alpha_E(\theta_i, \phi_i)$ is shown as a function of lattice-phase angle. The calculations here were carried out on the (111) crystal plane of Ni with $\theta_i = 37.5^\circ$, $\phi_i = 0^\circ$, $V_i = 1.12 \times 10^5$ cm/sec, and $T_s = 600^\circ K$. The parameter plotted on the abscissa is Z^1 of Eq. (28) by which the lattice-phase angle is varied. The extreme variation of $\alpha_E(\theta_i, \phi_i)$ with Z^1 is obvious. This situation is diametrically opposed to that existing when classical trajectory models are applied to the study of reactions occurring in crossed molecular beams. There it has been shown that vibrational-phase averaging for molecular vibrations can be ignored without appreciably altering the final result.[86] Figure 13 makes it clear that such is not the case for gas-surface interactions.

4. Spatial Distributions

It has been pointed out in the introduction that the 2D calculations were grossly inadequate with regard to predicting detailed shapes for experimental scattering patterns. The dashed line of Fig. 14 is representative of predicted 2D patterns in that they are uniformly too subspecular in character and far too broad. Both of these 2D artifacts are removed by the present generalized 3D treatment, and the resulting spatial distributions are in reasonable agreement with experiment.

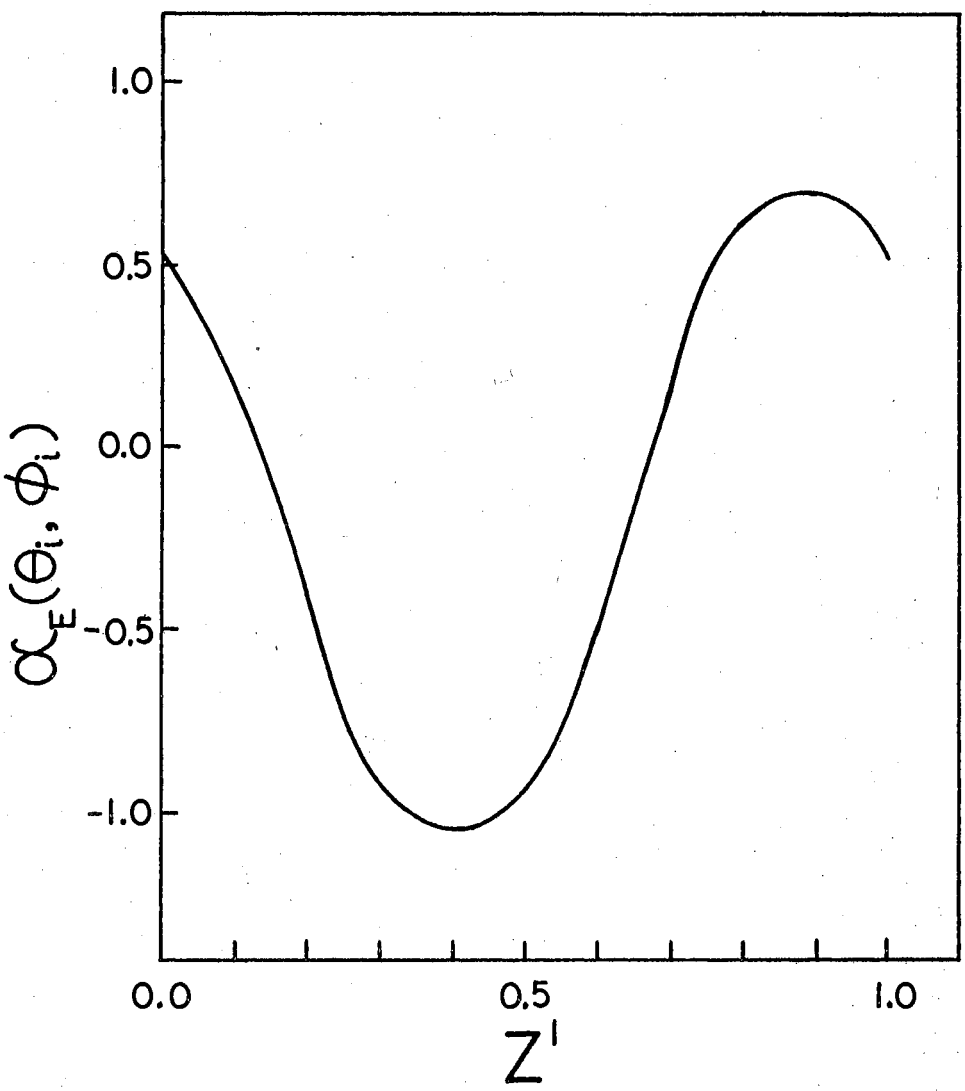

Figure 13. Variation of $\alpha_E(\theta_i, \phi_i)$ With Lattice-Vibrational-Phase Parameter.

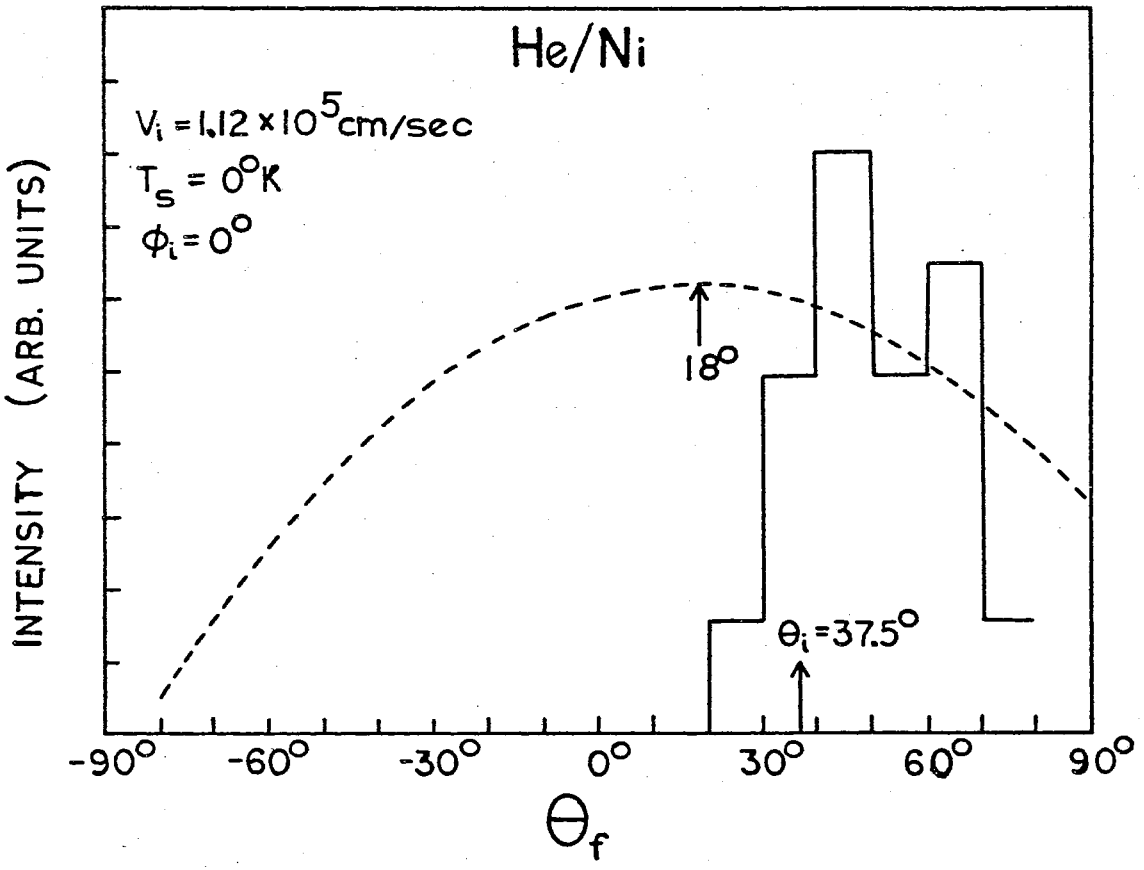

Figure 14. Comparison of Calculated 2D and 3D "In-Plane" Scattering Distributions. Dashed Curve is the 2D Result While the Histogram Represents the 3D Calculations.

The histogram plot shown in Fig. 14 represents a typical, "in-plane", 3D scattering pattern. The plot shown was obtained on the (111) plane of Ni with $T_s = 0^\circ K$, $V_i = 1.12 \times 10^5$ cm/sec, $\theta_i = 37.5^\circ$, and $\phi_i = 0^\circ$. Only particles scattered such that $160^\circ < \phi_f < 200^\circ$ are incorporated into the histogram to produce what might be regarded as the "in-plane" θ_f distribution. Aiming point averaging was carried out as previously described. It is obvious that all two-dimensional artifacts have been removed. The predicted half-widths are now much smaller and are approaching those observed experimentally, and the distribution is now peaked at a supraspecular angle (between the specular angle and the surface) as it should be since the surface temperature is $0^\circ K$.

A more quantitative comparison of the model with experiment is shown in Fig. 15. Here the circles represent the experimental in-plane scattering pattern obtained by Saltsburg, Smith, and Palmer[31] for a (He/Ag) system while the triangles represent the data of Smith and Saltsburg[28] for a (He/Au) system with $T_g = 300^\circ K$, $T_s = 560^\circ K$, and $\theta_i = 50^\circ$. The histogram plot represents the predicted (He/Ni) results under similar circumstances. Three trajectories evenly distributed over lattice-vibrational-phase for each of 25 surface aiming points were calculated. As can be seen, the agreement between theory and experiment

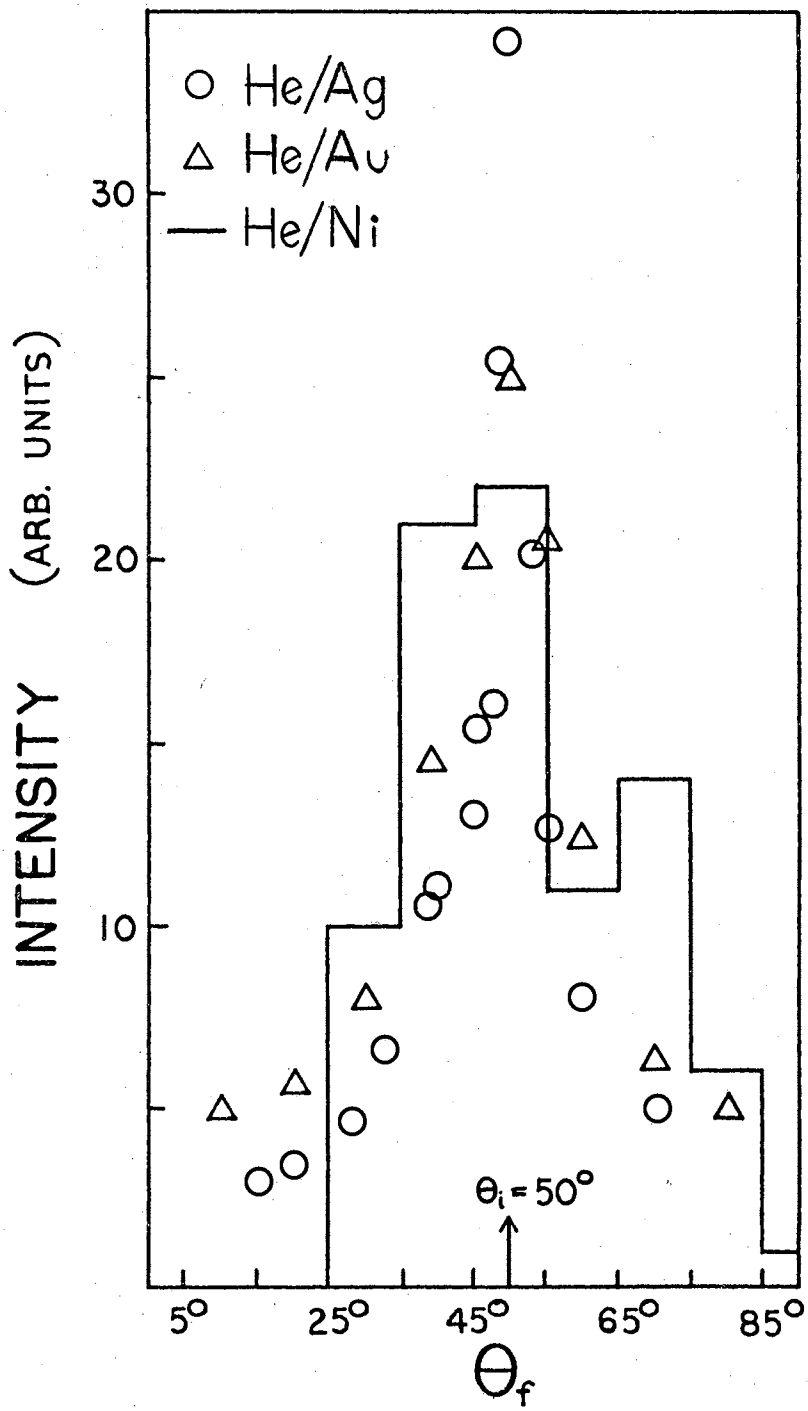

Figure 15: Comparison of Calculated 3D Scattering for a (He/Ni) System With Experimental Results.

is excellent both with regard to the position of the peak maximum and half-width.

It should be noted that the agreement between theory and experiment both here and elsewhere in the present work is the result of a totally unadjusted model. At no point has an effort been made to "fit" data by empirical adjustment of parameters.

It is interesting to note that the 3D distribution shown in Fig. 14 is "bimodal" in character in that there are two distinct peaks observed. Similar bimodal distributions have been experimentally observed as was noted in Chapter I.

Figure 16 represents a polar plot of the calculated scattering patterns for He from the (111) plane of Ni with $\Theta_i = 37.5^\circ$, $\phi_i = 0^\circ$, and $T_s = 0^\circ K$. The dashed curve is a smoothed polar representation of the histogram plot of Fig. 14 where V_i was representative of a gaseous beam temperature of $170^\circ K$. The bimodal structure of the distribution is clearly apparent. The solid curve shown in the figure represents the resulting distribution when V_i is increased to the most probable velocity for a He beam at $339^\circ K$. As can be seen, the bimodal structure vanishes in correspondence to the experimental results of Saltsburg, Smith, and Palmer[31] and Moore, Datz, and Taylor[3].

Figure 17 shows the variation of the spatial distributions with Θ_i. As before, $V_i = 1.12 \times 10^5$ cm/sec,

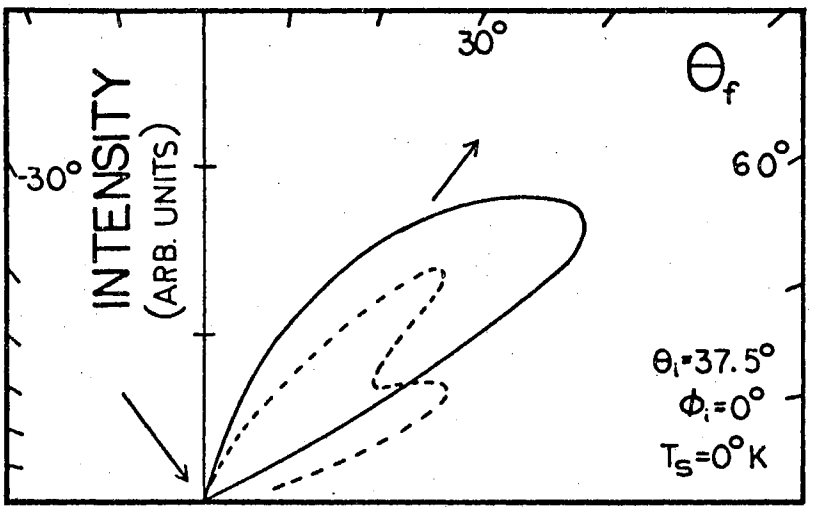

Figure 16: Variation of Spatial Distribution With Incident Beam Velocity. (----), $V_i = 1.12 \times 10^5$ cm/sec; (____), $V_i = 1.58 \times 10^5$ cm/sec.

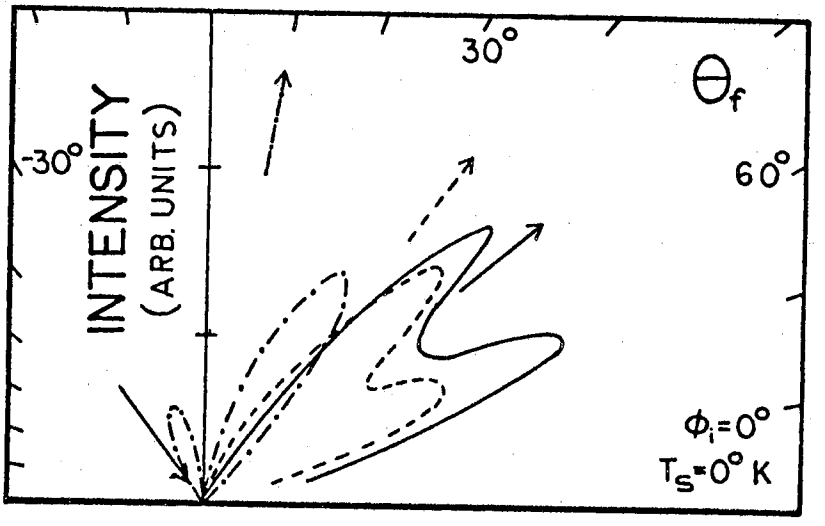

Figure 17: Variation of Spatial Distribution With Incidence Angle. (_____), $\Theta_i = 50°$; (----), $\Theta_i = 37.5°$; (-.-.-), $\Theta_i = 10°$.

$\phi_i = 0^\circ$, and $T_s = 0^\circ K$. In each case, the overall scattering is supraspecular as would be expected for a surface temperature of $0^\circ K$. Furthermore, the relative prominence of the bimodal structure tends to decrease with decreasing θ_i in correspondence to the results obtained by both Saltsburg, Smith, and Palmer[31] and by Datz, Moore, and Taylor.[3]

The variation of the spatial distributions with attractive well depth is illustrated in Fig. 18. The curves shown are for He scattered on a (111) Ni plane with $\theta_i = 37.5^\circ$, $\phi_i = 0^\circ$, $T_s = 0^\circ K$, and $V_i = 1.12 \times 10^5$ cm/sec. The dashed curve represents the results for a Morse D parameter of 0.00564 eV while the solid curve gives the results for a D of 0.00282 eV. Clearly the extent of the structure decreases with decreasing attractive well depth.

Variation of the surface temperature is predicted in the present work to have a significant effect upon measured scattering patterns. Figure 19 illustrates this point. The dashed curve is a reproduction of the dashed curve of Fig. 18 while the solid curve represents the predicted scattering pattern when T_s is increased to $600^\circ K$. Six trajectories evenly distributed over lattice-vibrational-phase were calculated for each of 49 surface aiming points. As can be seen, a sub-specular shift is predicted in correspondence both to the prediction of Ref. 79 and to experiment.[28] In addition, the bimodal structure is seen to decrease considerably in agreement with the results of

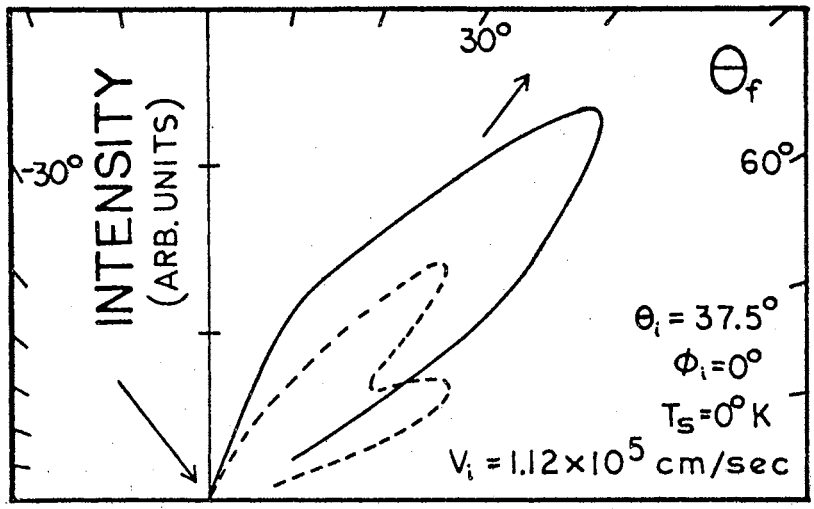

Figure 18: Variation of Spatial Distribution With Attractive Well Depth Parameter. (----), D = 0.00564eV; (____), D = 0.00282eV.

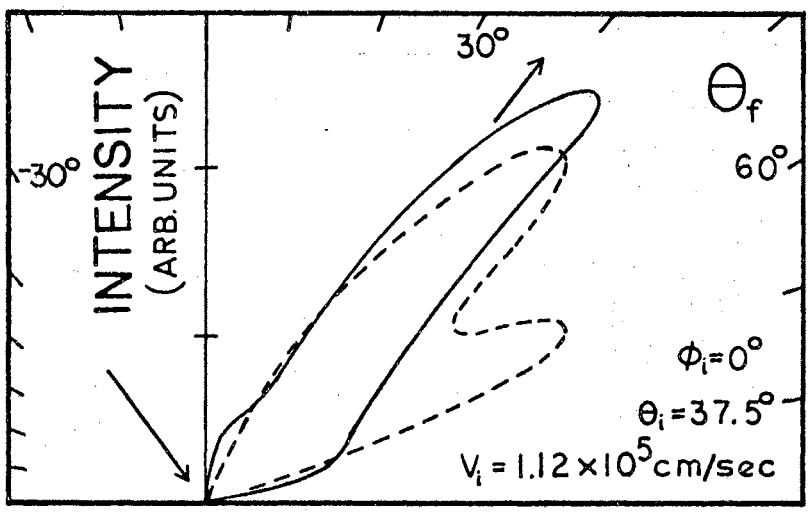

Figure 19: Variation of Spatial Distribution With Surface Temperature. (----) $T_S = 0°K$; (_____) $T_S = 600°K$.

Moore, Datz, and Taylor.[3]

As far as the model is concerned, it is a simple matter to show that the calculated structure effects result largely from the attractive wells which are present about 2.5Å from the surface. As the gaseous atoms approach the surface, their trajectories are bent toward the surface normal as a result of the accelerating effect of the well. By examining in detail trajectories aimed at different surface points, it becomes apparent that the above bending effect generally leads to scattering patterns which exhibit two favored directions. This is illustrated in Fig. 20 where projections of three trajectories on the shaded plane of the inset are shown. The dotted lines indicate the original trajectory direction while the solid curves give the actual scattering results. The accelerating effect of the well is clearly demonstrated here. Since the contour lines are relatively flat on this portion of the surface, one might expect near specular reflection if the dotted line path were followed. The change in incidence angle induced by the well, however, yields results which exhibit scattering in two general directions which differ widely from one another. It is such behavior as this which produces the bimodal patterns discussed above.

Once it is recognized that the bimodal structure predicted by the present model results from attractive well effects, the qualitative variation of the structure with V_i, Θ_i, D, and T_s can be explained. As V_i increases, the

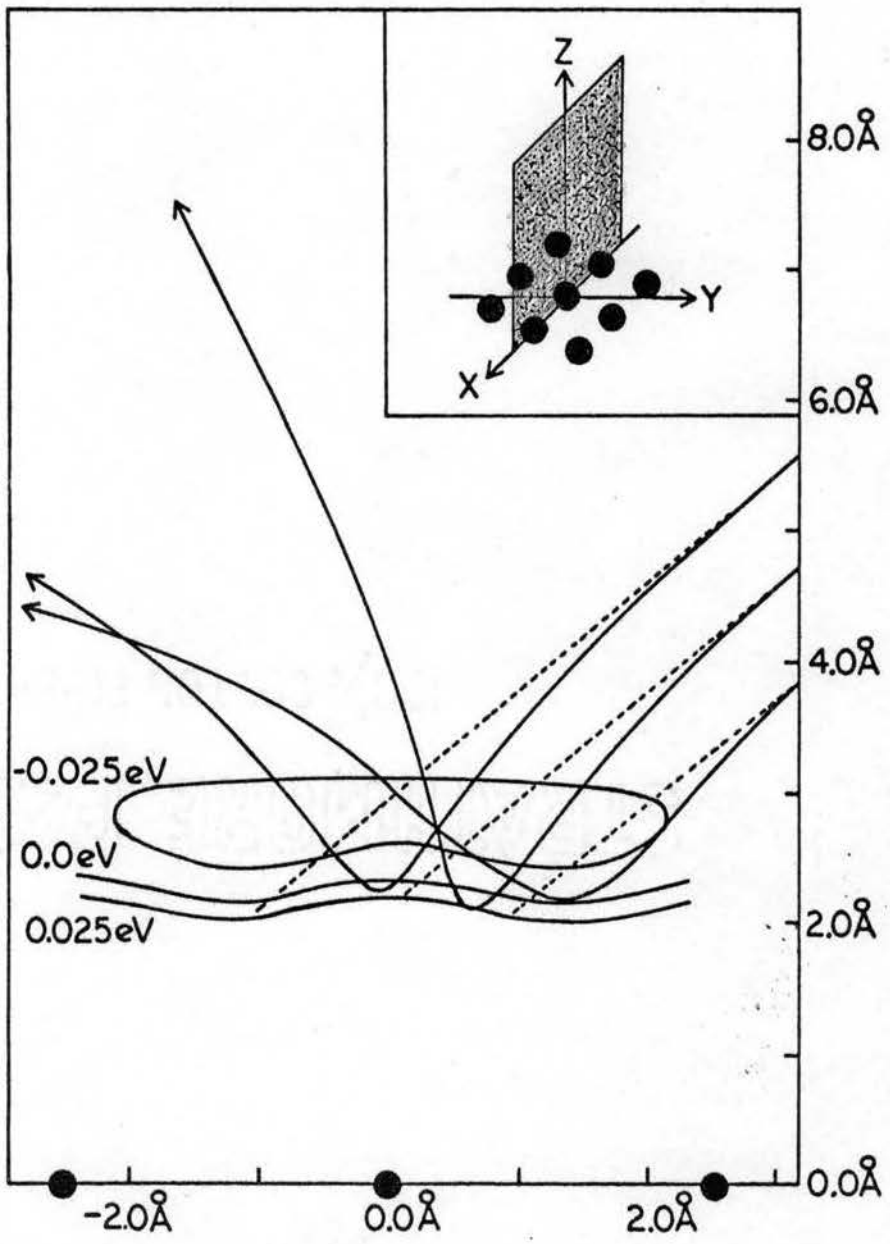

Figure 20. Accelerating Effect of the Attractive Well. Upper Inset Represents Plane of Trajectories Illustrated in the Figure.

the relative accelerating effect of the well will decrease, and hence, the relative prominence of the structure will decrease. As Θ_i increases, the bending effect illustrated in Fig. 20 will likewise increase. Thus, one would expect the bimodal structure to be most prominent at relatively large Θ_i. However, as Θ_i approaches 90° the scattering of all particles would be dominated by the wells and thus the upper lobe would be expected to disappear. As D decreases, so does the well depth, which will in turn reduce the effect. As T_s is increased, the final scattered energy of the gaseous atom, E_g^f, is increased as in Fig. 12 and again the effects of the attractive well are reduced.

Figures 21(a) and 21(b) show the calculated ϕ_f distributions for the (111) plane with $\Theta_i = 37.5^\circ$, $\phi_i = 0^\circ$, $T_s = 0^\circ K$, and V_i the most probable velocity at $T_g = 170^\circ K$ for 21(a) and $T_g = 339^\circ K$ for 21(b). The smooth curves are obtained by fitting Lorentz functions by least square technique to the histogram plots. As can be seen, the distributions are peaked at the in-plane angle of 180° and fall-off rapidly in accord with experimental observations.[25] Comparison of Fig. 21(a) and Fig. 21(b) indicates that a narrowing effect should occur at elevated temperatures. The histograms indicate the presence of some structure which disappears with increasing T_g.

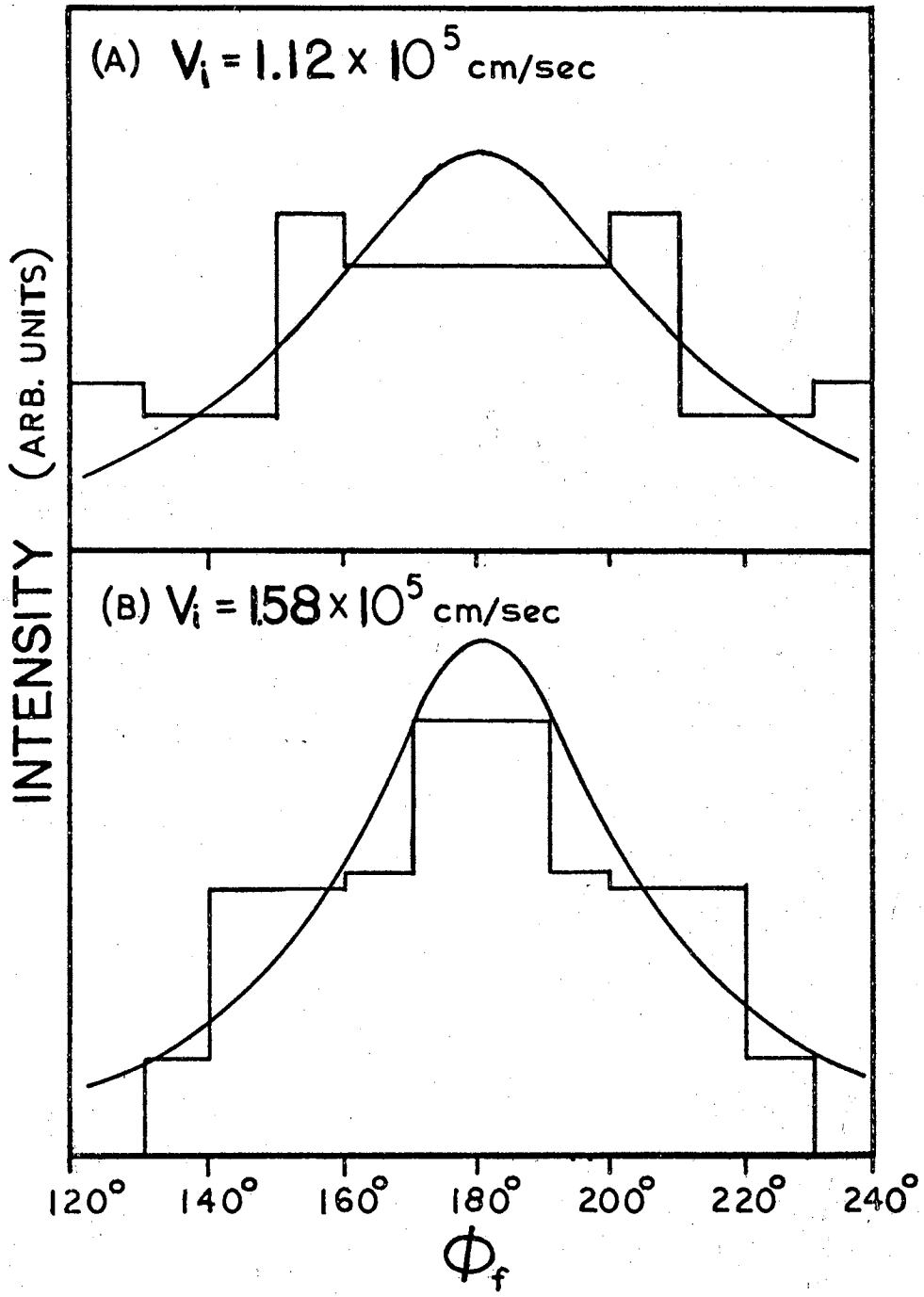

Figure 21. Variation of Out-of-Plane Scattering With Incident Particle Velocity.

The present model also predicts that the general shape of the ϕ_f distribution should be a rather insensitive function of ϕ_i and that it should become narrower as Θ_i increases and as D decreases.

The dependence of the in-plane Θ_f distributions upon ϕ_i have been examined, and the results predict a small subspecular shift of the lobe maxima and a general broadening of the distribution as ϕ_i increases from 0° on the (111) Ni plane. Experiment on (He/Ag) systems indicates the in-plane Θ_f distributions to be independent of ϕ_i.[31] On the other hand, (Ar/LiF) systems show a distinct Θ_f dependence on ϕ_i.[23]

D. Summary and Conclusions

The calculations of Ref. 79 have been extended to 3D by representing the (100) and (111) planes of Ni with nine movable lattice sites connected to fixed points by harmonic springs in a geometry chosen to simulate that present for the two crystal planes. The gaseous atom-surface interaction is constructed from nine pairwise Morse potentials operating between the gaseous atom and the nine movable lattice points. The dynamics of the system have been investigated under the assumption of classical motion, and relevant energy transfer coefficients and spatial distributions have been calculated as a function of incidence angles, beam velocity and temperature, surface temperature, gaseous atom mass, lattice force constant, and attractive

well depth and curvature. In general, the results indicate the following:

(1) Three-dimensional potential surfaces tend to exhibit deeper attractive wells than the corresponding 2D surfaces due to the added interactions of adjacent lattice atoms. Corresponding potential contour lines on a 3D surface exhibit less curvature than on the 2D surface.

(2) The ETC should be a decreasing function of incidence angle. In general, the rate of decrease of $\alpha_E(\theta_i,\phi_i)$ with θ_i seems to be sufficiently large to justify the "normal component model."

(3) The ETC should increase monotonically with increasing attractive well depth.

(4) The ETC should increase rapidly with decreasing lattice force constant.

(5) The ETC should increase as the steepness of the repulsive potential wall increases. This result implies that hard sphere models will tend to overestimate the energy transfer unless compensated in some manner.

(6) The extent of energy transfer is a rather insensitive function of the crystal plane being attacked.

(7) Energy transfer and normal scattering are favored for collisions which occur near a surface lattice site.

(8) The ETC is virtually independent of ϕ_i but is predicted to increase as ϕ_f moves away from the "in-plane" angle.

(9) The isotope effect yields $[\alpha_E(\theta_i,\phi_i)]_{^4He} > [\alpha_E(\theta_i,\phi_i)]_{^3He}$ provided E_g^i is in excess of the attractive well depth. For E_g^i values less than the well depth an inversion of the above isotope effect is seen due to the enhanced accelerating effects of the well upon the lighter atom.

(10) The ETC is a strong function of T_s and decreases monotonically as $T_G - T_s$ decreases. When $T_s \neq 0^\circ K$, lattice phase averaging becomes very important in systems of this type.

(11) The broadness and subspecular character of the scattering patterns obtained in Ref. 79 are artifacts of the 2D model and are completely removed by the extension to 3D.

(12) The scattering angle is strongly dependent upon aiming point.

(13) Bimodal spatial distributions result in part from the accelerating effect of the attractive well upon the incident gaseous atom. The prominence of this bimodal structure is predicted to decrease with increasing T_g and T_s, increase with increasing θ_i, and decrease with decreasing attractive well depth. Although this behavior is in accord with observation, it is felt there are still enough quantitative discrepancies present to make a one-to-one correlation between experimental bimodal distributions and the present calculations somewhat hazardous. This topic

is discussed further in Chapter V.

(14) A subspecular shift of the spatial distribution should occur with increasing T_s.

(15) The ϕ_f distributions are peaked at the in-plane angle and decrease rapidly on either side of it.

(16) The ϕ_f distributions are virtually independent of ϕ_i and become narrower as Θ_i and T_g increase and as D decreases.

(17) The Θ_f distributions exhibit a small subspecular shift of the lobe maxima and generally become more diffuse as ϕ_i increases from 0° on the (111) Ni plane.

(18) Whenever comparison with experiment is possible, all of the above results are found to be in qualitative to semi-quantitative agreement with experiment.

The final conclusion reached in Ref. 79 that the general approach is well suited to the study of such heterogeneous interaction phenomena seems justified by the present calculations. In the next chapter the model is employed to study the effects related to lattice dynamics and temperature.

CHAPTER IV

VELOCITY DISTRIBUTIONS AND SURFACE TEMPERATURE

A. Introduction

Recent gas-surface experiments have revealed some interesting effects that seemingly are related to lattice dynamics and temperature. Smith, Saltsburg, and Palmer[32] and Moran[41] have observed that monoenergetic beams give spatial scattering distributions that are similar to those resulting from thermal beams. The results seem to imply that thermal motion of the lattice is the dominant factor in producing spatial and velocity dispersion in the scattered beam. The hard-cube model successfully predicted the similarity of thermal and velocity-selected beam scattering, but the origin of the phenomenon was not revealed.[89] From a comparison of their scattering data for noble gases on Ni, Ag, and Au, Smith, Saltsburg, and Palmer[33] conclude that a simple description of the solid in terms of mass and heat of physical adsorption is inadequate. Smith, O'Keefe, Saltsburg, and Palmer[23] have studied the interaction of Ar and LiF crystals and found that the properties of the reflected spatial distributions are very sensitive to the nature of the surface. These results

suggest the use of thermal energy beams to study surface characteristics. Stickney[43] has studied the scattering of noble gases from single W crystals and observed that the scattering distributions become temperature independent for large surface temperatures.

In this chapter the gas-solid model introduced in Chapter III is employed to study effects of the velocity distribution in the incident beam and vibrational motion of the lattice atoms. The model leads to some new interpretations of experimental results and to some interesting possibilities concerning the velocity distributions of reflected particles. Section B briefly discusses the model employed for the calculations. In Section C the results obtained for different incident particle velocity distributions and surface temperatures are given and discussed. The results are summarized in Section D.

B. Formulation

The 3D, classical model described in Chapter III was employed in the present study of surface effects. Nine movable lattice sites are connected to fixed points by harmonic springs in a geometry representative of an FCC (111) crystal surface. The interaction potential is constructed from nine pairwise Morse potentials operating between the incident gaseous atom and the nine movable lattice points. The surface atoms are given an initial classical energy of $3\bar{k}T_s$. Numerical integration of the

Hamiltonian equations for the system results in ETC's and scattering distributions of reflected particles.

The computer time required for each trajectory was reduced in the calculations of this chapter by replacing the ten-body model with a two-body model after the reflected gaseous particle was 5 Å from the surface. At this separation the lattice atoms were replaced by one fixed site. Employment of an effective Morse potential with α = 1.35 $Å^{-1}$, D = 0.019eV and Re = 3.11 Å then gave results consistent with a complete ten-body, (He/Ni) integration.

As in Chapter III scattering distributions were obtained from a number of trajectories with different aiming points on the unit cell. The same initial velocity of the gaseous atom, V_i, was employed for each trajectory in a set of calculations. The results then, correspond to the interaction of an ideal velocity — selected beam. This calculation was performed for a number of V_i's distributed over a range. The results were combined in proportion to a skewed Maxwellian distribution characteristic of a beam effusing from a Knudsen cell at a temperature T_g ($\propto V^3 \exp(-M_g V^2/2\bar{k}T_g)$). This procedure theoretically simulates the interaction of an incident thermal beam. Both spatial and velocity distributions of reflected particles were calculated in this manner.

C. Results and Discussion

1. Gaseous Particle Velocity Distribution

The interaction of He with a FCC (111) Ni surface at $T_s = 600^{\circ}K$ for $\theta_i = 37.5^{\circ}$ and $\phi_i = 0^{\circ}$ was studied as a function of incident particle velocity and beam temperature. The spatial scattering and reflected velocity distributions were calculated and plotted as histograms for $V_i = 6.45 \times 10^4$ cm/sec, 1.12×10^5 cm/sec, 1.58×10^5 cm/sec, 2.04×10^5 cm/sec, 2.49×10^5 cm/sec, and 2.96×10^5 cm/sec. Three trajectories, evenly distributed over lattice-vibrational-phase, were computed at each of 26 aiming points. For $V_i = 0.645 \times 10^5$ cm/sec, 1.12×10^5 cm/sec, and 2.04×10^5 cm/sec, twice as many trajectories were eventually calculated. In each case the smaller number of trajectories had given qualitatively reliable results although the statistical scatter was more noticeable.

For low velocity cases a significant number of trajectory calculations resulted in trapped particles. Particles were arbitrarily assumed to be trapped if they collided with the surface more than once before escaping or if $\theta_f > 85^{\circ}$. With these assumptions, 30% of the particles with $V_i = 0.645 \times 10^5$ cm/sec and 17% of those with $V_i = 1.12 \times 10^5$ cm/sec were trapped. These particles were assumed to be completely accommodated and diffusely scattered so that they were included in the predicted spatial

distributions as a cosine contribution.

Lorentz functions were fitted to the predicted "in-plane" spatial distribution histograms. The resulting peak positions and widths at half-amplitude are plotted against V_i in Fig. 22. The peak position for $V_i = 1.12 \times 10^5$ cm/sec is clearly displaced toward the surface. Although this difference is near the limit of statistical scatter, the (Ar/Ag) experiments of Saltsburg and Smith[29] and calculations by Oman[78] show the same general trend. In both calculations the maximum amount of supraspecular displacement occurs at an incident energy of the same magnitude as the attractive wells of the interaction potential surface. Thus, an influence from the attractive wells is suggested. For large V_i the effect of the wells is negligible. The peak positions lie at the specular angle and the peak widths are almost independent of V_i as would be the case if the structure of the interaction potential contour surface dominated the interaction. As V_i decreases the particle energy becomes comparable to the attractive well depth. Initially, this causes low energy reflected particles to be scattered closer to the surface. Finally, for small V_i it causes slow particles to be trapped in the wells. Only particles that obtain large momenta components through interaction with surface atoms manage to escape. However, the momenta transferred from the lattice is largely normal to the surface, and therefore, tends to produce cosine scattering. Thus, the scattering peak

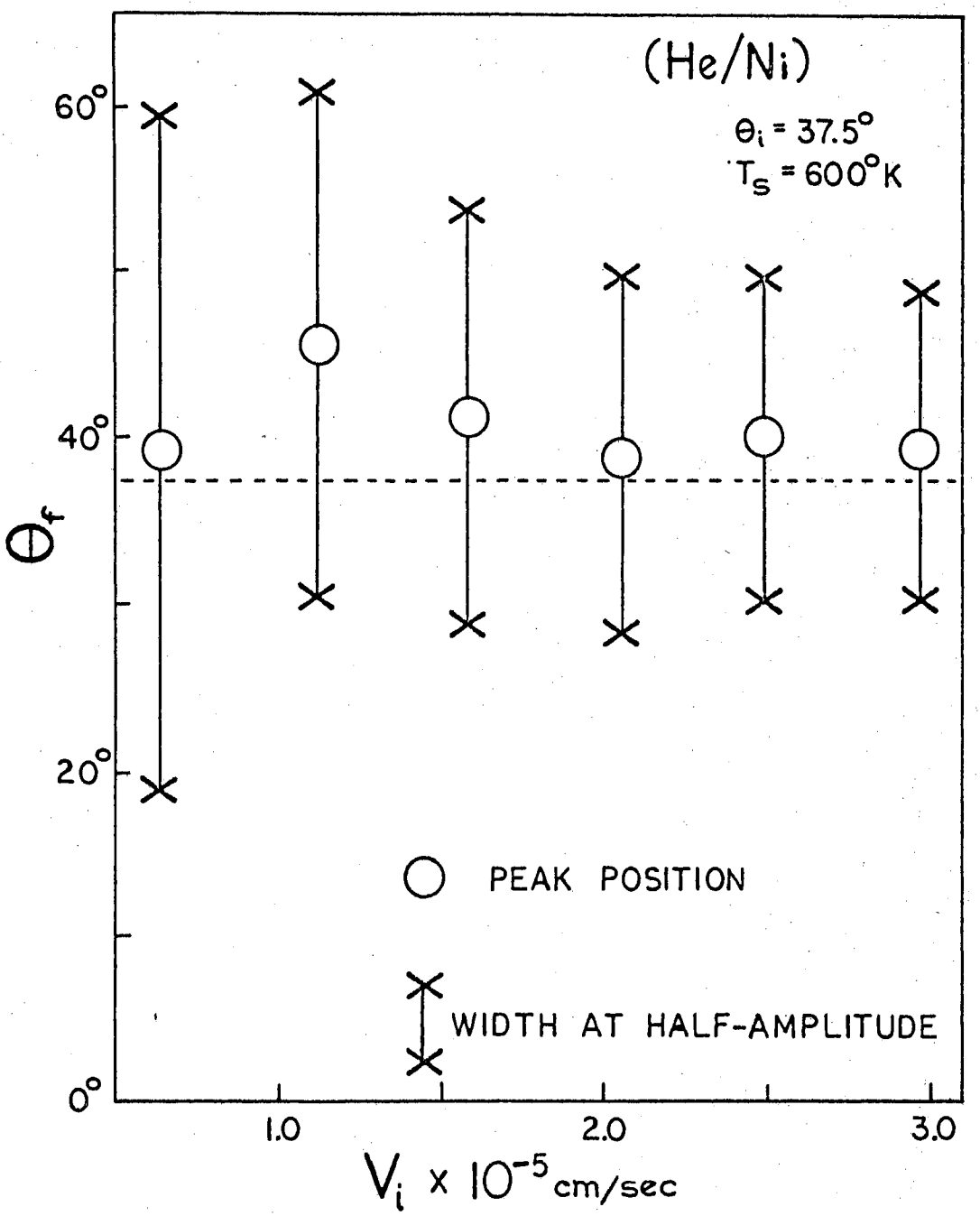

Figure 22. Variation of "In-Plane" Spatial Scattering With Incident Particle Velocity.

positions shift back toward the surface normal. In the limit of vanishing V_i the peak position approaches 0° since a cosine distribution would be observed. Oman[77, 78] has predicted and discussed the type of behavior described above and has denoted it by the terms "structure scattering" for large V_i and "thermal scattering" for small V_i.

It should be noted that the parameters employed in this work to represent (He/Ni) give excessively large attractive wells as was discussed in Chapter III, Section C.2. Thus, the predicted dependence of peak position on V_i in Fig. 22 is exaggerated, and quantitative agreement with experimental results for (He/Ni) cannot be expected.[33] If the above explanation for the behavior of Fig. 22 is valid, however, experimental measurement of scattering peak positions vs. V_i would give a means for estimating the attractive well interaction potential parameters.

The calculated scattering distribution histograms for the six V_i's of Fig. 22 were combined in the correct proportions to simulate thermal beams with $T_g = 170^\circ K$, $339^\circ K$, and $565^\circ K$. In Fig. 23 the resulting "in-plane" spatial scattering distribution for these thermal beams is compared with the scattering from the corresponding velocity-selected beams. The V_i of the velocity-selected beam in each case is equal to the average velocity of the effusive Maxwellian, i. e., $\bar{V} = 3/4\ (2\pi\bar{k}T_g/M_g)^{\frac{1}{2}}$. The histograms represent the number of particles scattered into each 10 increment of Θ_f.

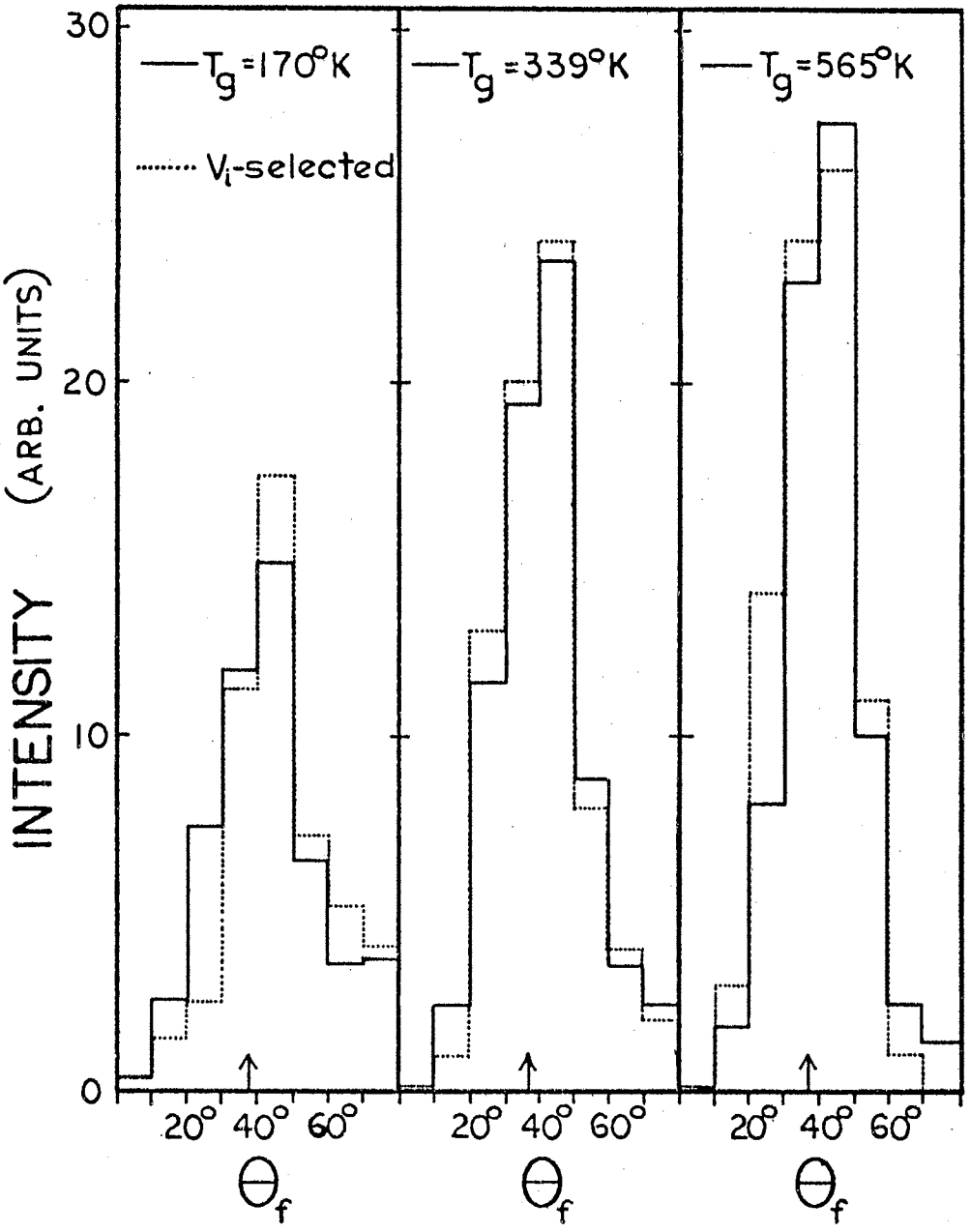

Figure 23. Comparison of Velocity-Selected and Thermal Beam Spatial Scattering.

Lorentz functions were fitted to the thermal beam histograms, and the results are shown in Fig. 24. The spatial distributions from Fig. 22 for velocity-selected beams have also been included. Comparison, which is facilitated because the statistical fluctuation has been averaged by the Lorentz fitting, shows that the thermal peak position is displaced toward the surface normal for low T_g, identical with the velocity-selected peak for intermediate T_g, and displaced toward the surface for larger T_g. The thermal-beam scattering widths are larger at all T_g, increasing from 0.4° larger at $T_g = 170^\circ K$ to 1.0° larger at $T_g = 565^\circ K$. The differences are near the limits of statistical error and may not be significant.

Clearly, the velocity-selected and thermal beam spatial scattering distributions calculated by the model are similar. This resemblance results from the small but regular dependence of scattering on V_i. The decreasing width that accompanies increasing V_i produces a cancellation of differences. That is, in a thermal beam the low velocity particles are more diffusely scattered than are the particles of average velocity, which are, in turn, scattered more diffusely than high velocity particles. The low and high velocity scattering differences tend to cancel when combined, and the result is very similar to the scattering obtained from particles having the average velocity only. The same reasoning applies to the peak

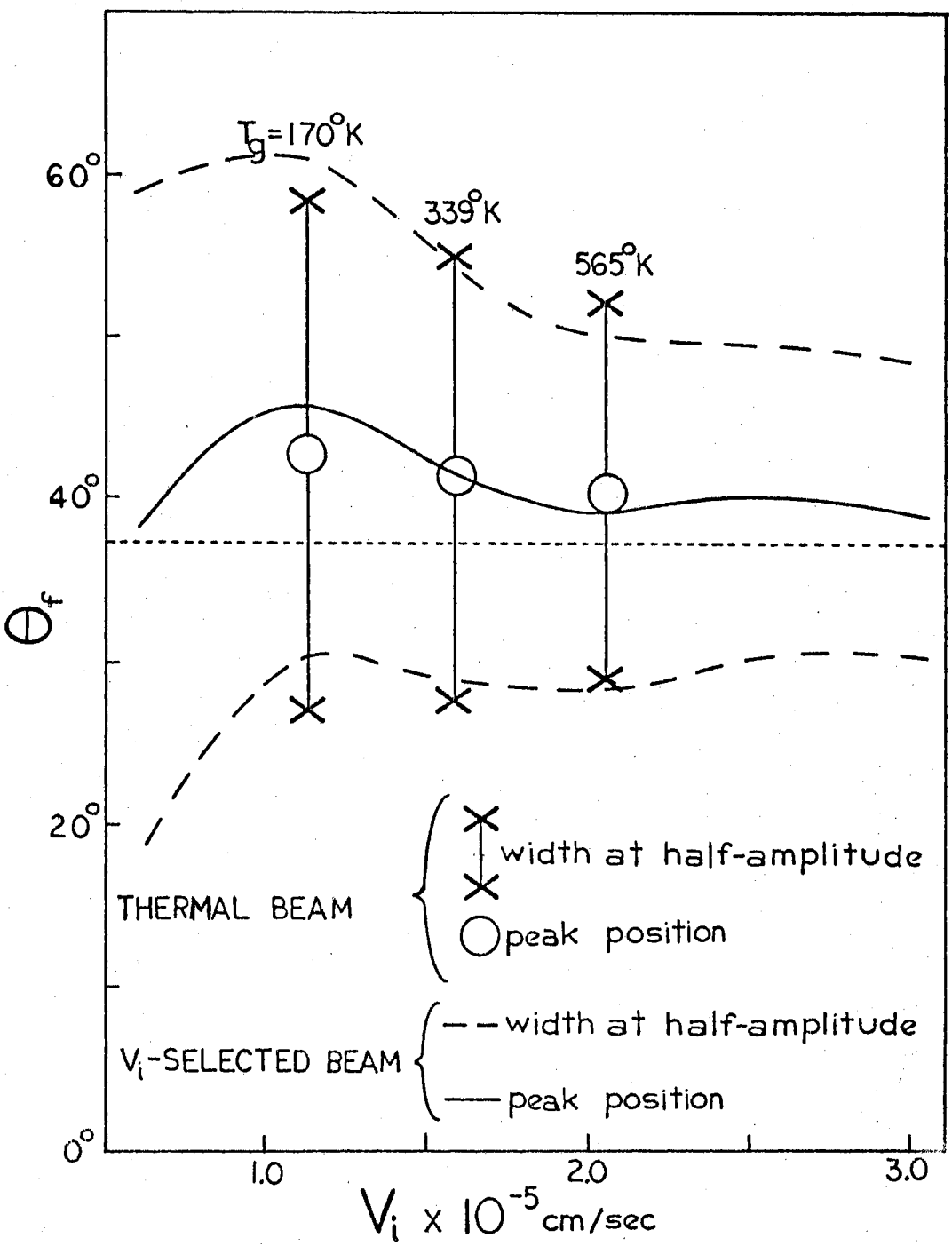

Figure 24. Comparison of Velocity-Selected and Thermal Beam Scattering.

position, although the fact that at first the shift is toward the surface but then reverses toward the normal makes the relationships more complex.

In Fig. 25 the V_f distributions of particles scattered "in-plane" into the specular lobe ($30^\circ < \theta_f < 50^\circ$) are plotted for the six V_i's of Fig. 22. These plots roughly correspond to the V_f distributions that would be measured by a detector positioned at the specular angle. The distributions are normalized to the same number of incident particles. The calculated average ETC's for each V_i are also included in the figure. Clearly, the final velocity distributions are not Maxwellian in character; interaction with the surface causes significant dispersion of final velocities. The tendency for particles to either gain or lose energy by interaction creates a definite bimodal distribution of reflected velocities. The magnitude and consistency of the structure indicate that statistical error is not responsible. Twice as many trajectories were calculated for $V_i = 2.04 \times 10^5$ cm/sec. The same qualitative behavior was predicted, thus, reducing the liklihood of a systematic error due to too few trajectories.

As can be seen from Fig. 23, the corresponding spatial scattering distribution for $V_i = 2.04 \times 10^5$ cm/sec shows no structuring. A spatial distribution histogram plot with an improved resolution of 5° rather than 10° also showed only a single peak. Therefore, it appears that the V_f distributions are more sensitive to the gas-solid

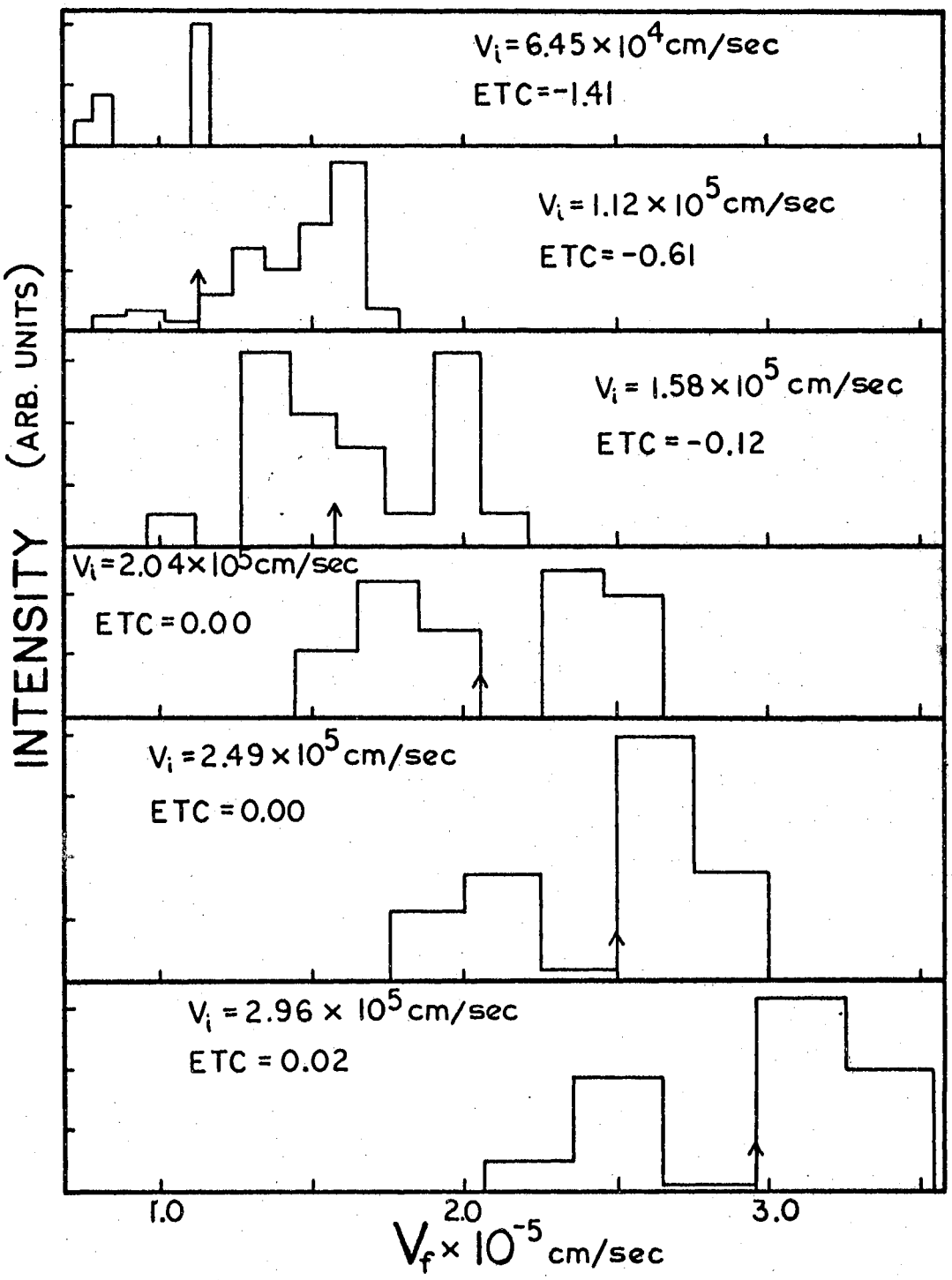

Figure 25. Variation of Reflected Velocity Distributions With Incident Velocity. The Distributions are for Particles Scattered in the Ranges ($50^\circ > \theta_f > 30^\circ$) and ($200^\circ > \phi_f > 160^\circ$).

interaction than are the spatial distributions. As a result, the V_f distributions could be expected to show more dependence upon velocity distribution in the incident beam.

Figure 26 compares the V_f distributions from a thermal beam at 170°K and the corresponding velocity-selected beam. The dashed curve of Fig. 26 (a) indicates a skewed Maxwellian distribution of initial velocities. The histogram represents four blocks of V_i's that were used in the proportions indicated to simulate the thermal beam. The distributions of these four V_i's from Fig. 25 were combined. The resulting thermal beam V_f distribution is denoted by the solid-line histogram in Fig. 26(b). For comparison the corresponding velocity-selected V_f distribution from Fig. 25 has been included. They are normalized to the same number of incident particles. As can be seen, the thermal beam gives a broader distribution, particularly in the high velocity region for this case in which $(T_g/T_s) = 0.28$.

Figure 27 shows the same comparison of V_f distributions for $T_g = 565°K$. For this case, $(T_g/T_s) = 0.94$ and the thermal distribution is broader in both the low and high velocity regions. The bimodal velocity distribution is still present, although not so distinctly as in the velocity-selected case. Structure averaging occurs because the maximum in the V_f distribution for one V_i often coincides with the minima of other V_i.

The model clearly predicts that final velocity

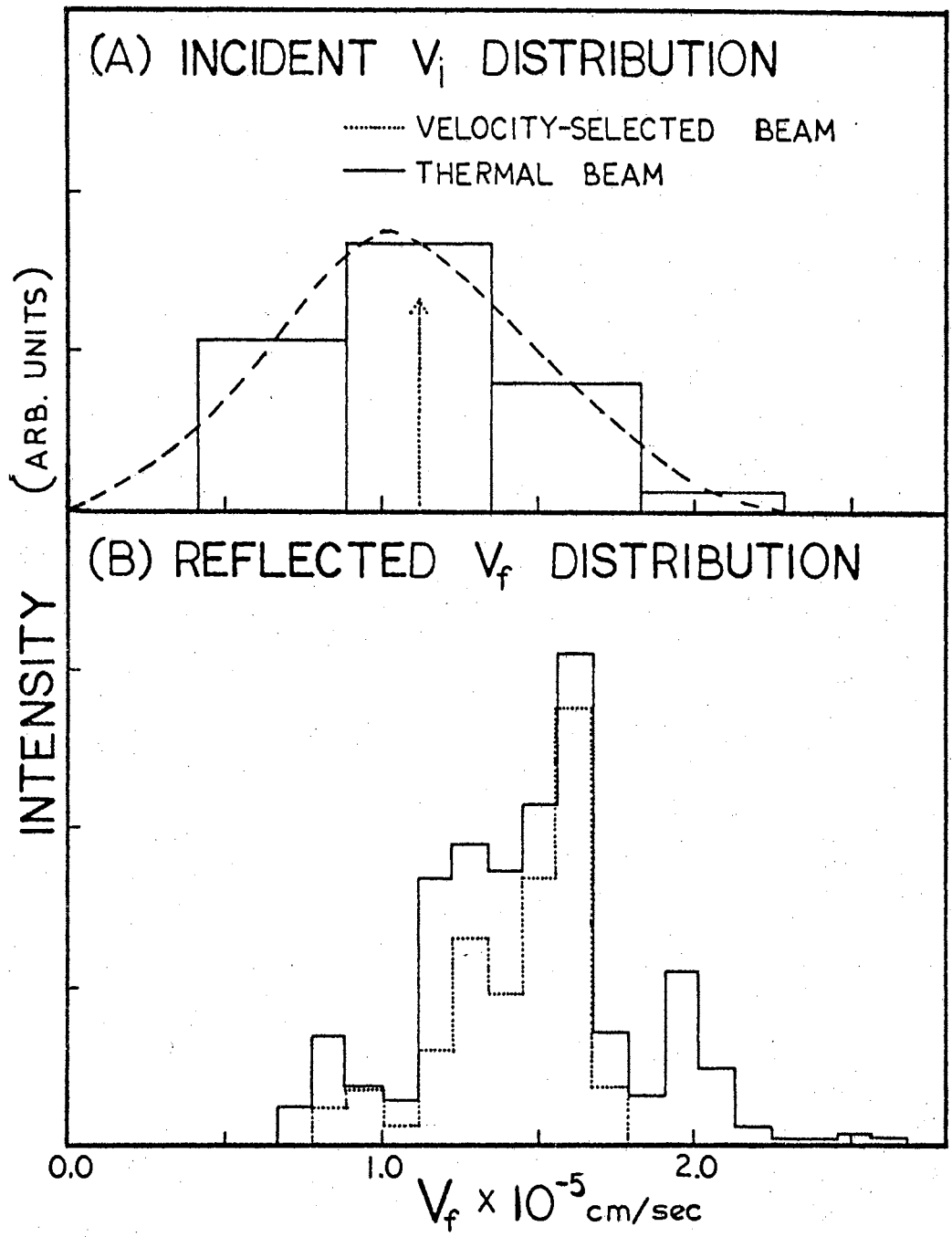

Figure 26. Comparison of Reflected Velocity Distributions for Velocity-Selected and Thermal Beams at $T_g = 170°$ K.

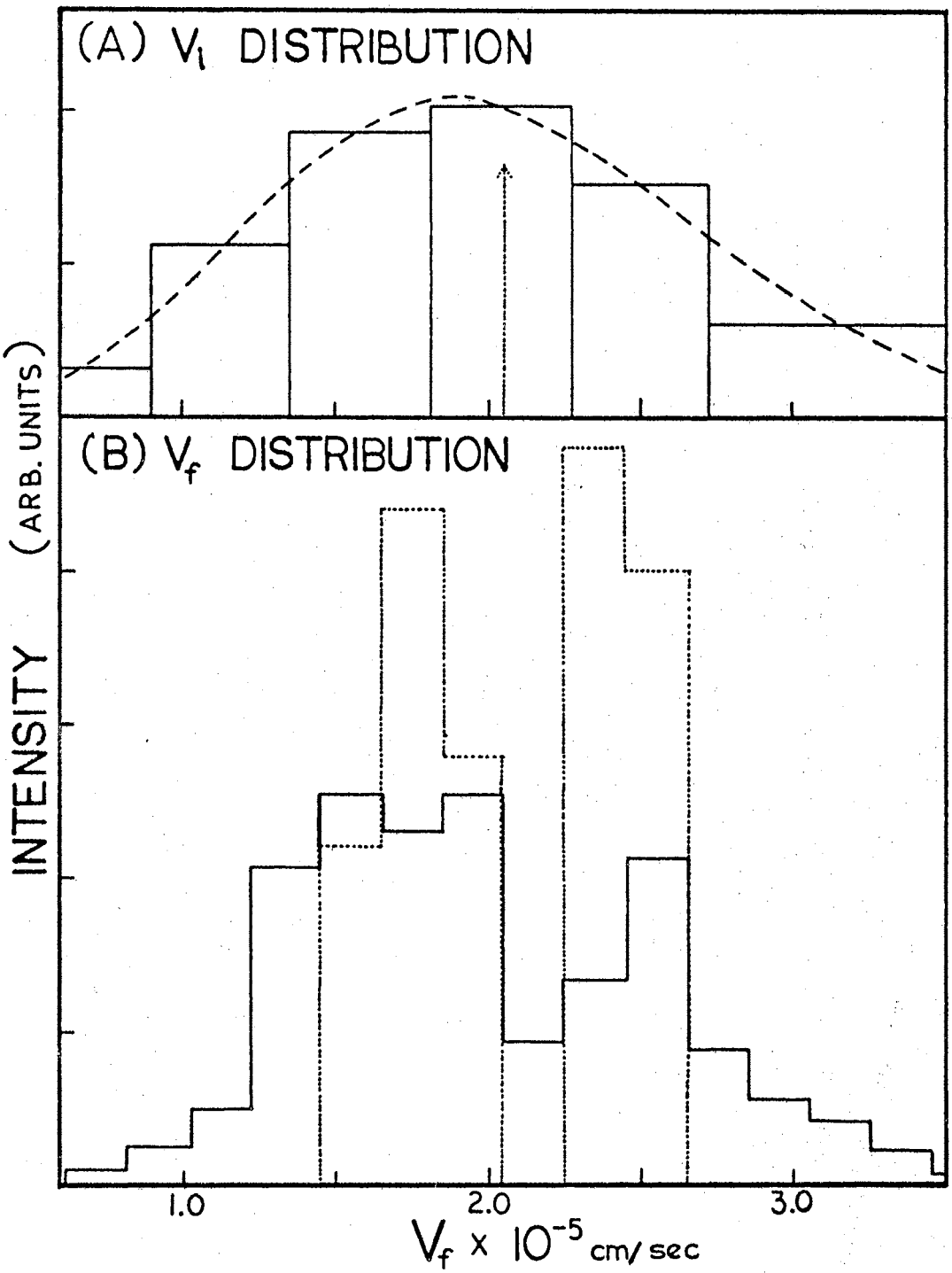

Figure 27. Comparison of Reflected Velocity Distributions for Velocity-Selected and Thermal Beams at $T_g = 565^\circ$ K.

distributions are, in some ways, more sensitive to the interaction than are spatial distributions. Experimental V_f distributions should show a dependence on V_i distribution and could show bimodal characteristics. As has been noted, however, the parameters employed in the model to simulate (He/Ni) are not true values. Hence, the calculations may exaggerate scattering characteristics.

2. Surface Temperature

To further investigate the importance of lattice energy, the dependence of the interaction on T_s has been studied in more detail than was reported in Chapter III. There, (He/Ni) calculations were completed for $\Theta_i = 37.5^\circ$, $\phi_i = 0^\circ$, $V_i = 1.12 \times 10^5$ cm/sec with $T_s = 0^\circ$K and 600°K. As can be seen in Fig. 19, the changes that result from the 600° surface temperature increase are a disappearance of bimodal structure, a subspecular shift of the spatial scattering, and a decrease in half-widths. The ETC also changes from positive to negative.

New calculations were completed for $T_s = 300^\circ$K, 900°K, and 1200°K. The complete set of "in-plane" spatial distributions are shown as polar plots of intensity vs. Θ_f in Fig. 28. For 900°K, six trajectories were calculated for each of 26 aiming points. For 300°K and 1200°K only aiming points that had given "in-plane" scattering in the previous calculations were employed. Accurate "in-plane"

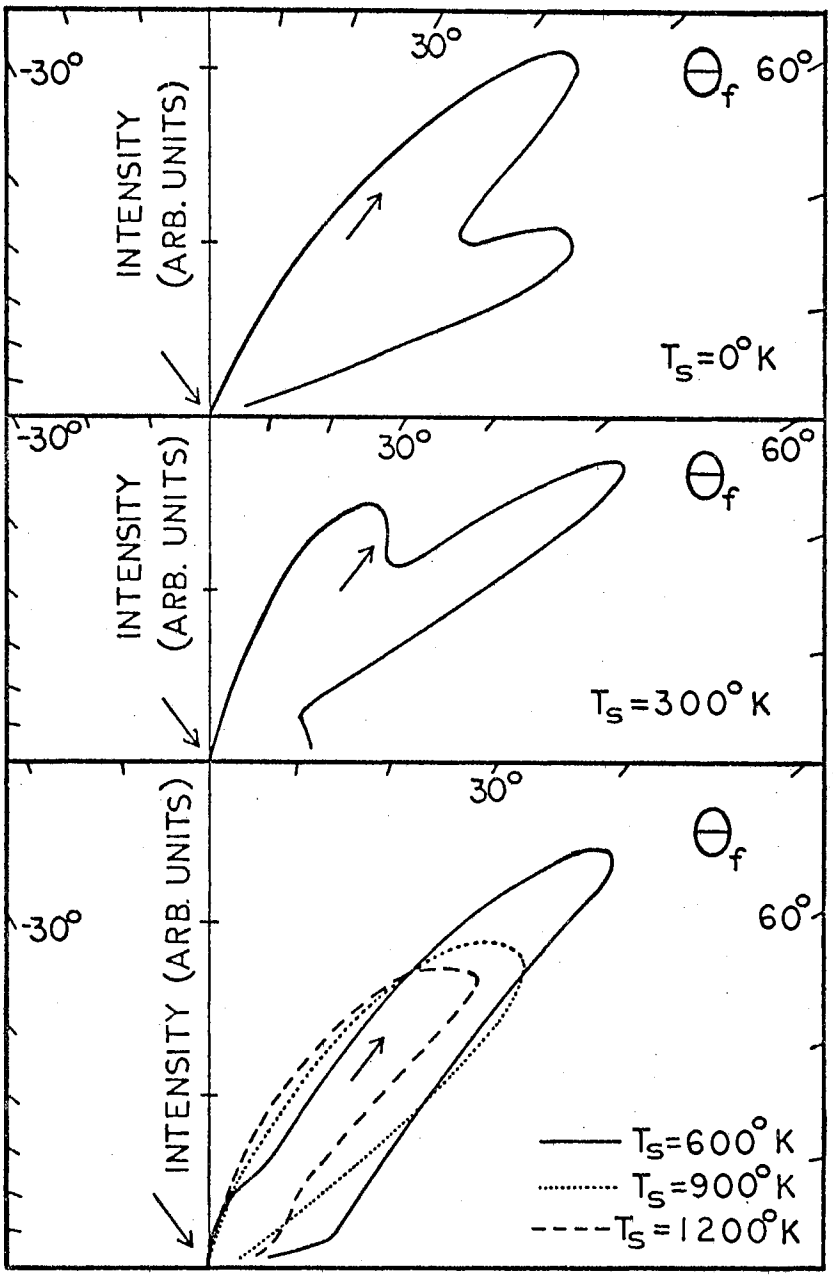

Figure 28. Variation of the "In-Plane" Spatial Distributions With Surface Temperature.

scattering distributions were still obtained, but out-of-plane distributions and percentages of trapped particles were not determined.

The most noticeable difference in Fig. 28 occurs when T_s changes from $0^{\circ}K$ to $600^{\circ}K$. For higher T_s the changes are of the same magnitude as statistical error, and it is difficult to draw any definite conclusions. However, there is a subspecular shift with increasing T_s. The half-widths remain approximately constant.

An interesting observation can be made from Fig. 28 concerning the relative effects of surface structure and lattice energy on scattering distributions. For $T_s = 0^{\circ}K$, surface structure (periodic variations in the interaction potential surface) and the response of lattice atoms to the incoming particles are the source of the calculated scattering. As can be seen, surface structure alone is sufficient to cause significant dispersion in the spatial scattering. For nonzero T_s the lattice atoms become kinetic partners in the interaction. The changes represented by Fig. 28 indicate, in part, the increasing effect of the kinetic energy of the surface atoms on the spatial scattering. However, as can be seen in Fig. 22, $V_i = 1.12 \times 10^5$ cm/sec with $T_s = 600^{\circ}K$ gives scattering that lies in the transition domain between thermal and structure scattering. Thus, the thermal effect could be masked to a degree by structure scattering. The interplay of thermal and structure

scattering could explain the independence of spatial scattering and T_s observed for high surface temperatures.[43] It is not then, surprising that the hard cube model fails to make this prediction since it treats thermal scattering but not structure scattering.[69, 70]

The variation of the V_f distributions with T_s is shown in Fig. 29. All particles scattered "in-plane" are considered. The plots are normalized to the same number of incident particles (note the change of scale for $T_s = 0^{\circ}K$). Comparison with Fig. 28 shows that surface temperature has a larger effect on final velocity than spatial distributions. For $T_s = 0.0^{\circ}K$, the interaction potential structure causes little dispersion of final velocities in contrast to the situation for spatial scattering. For nonzero T_s the V_f distributions are broadened considerably because particles both gain and lose energy during interaction with the energetic surface atoms. As would be expected, for increasing T_s greater percentages gain energy from the lattice.

It is interesting to note that for several trajectories energy transfer is from the gas to the lattice ($V_f < 1.12 \times 10^5$ cm/sec) even for $T_s > T_g$. This phenomenon is due to the relative velocity of the gaseous atom and lattice atom, V_r. For zero surface temperature the lattice atoms are assumed to be at rest and V_r is not a function of lattice atom vibrational-phase. As T_s increases, however, V_r becomes a strong function of vibration-phase. During the

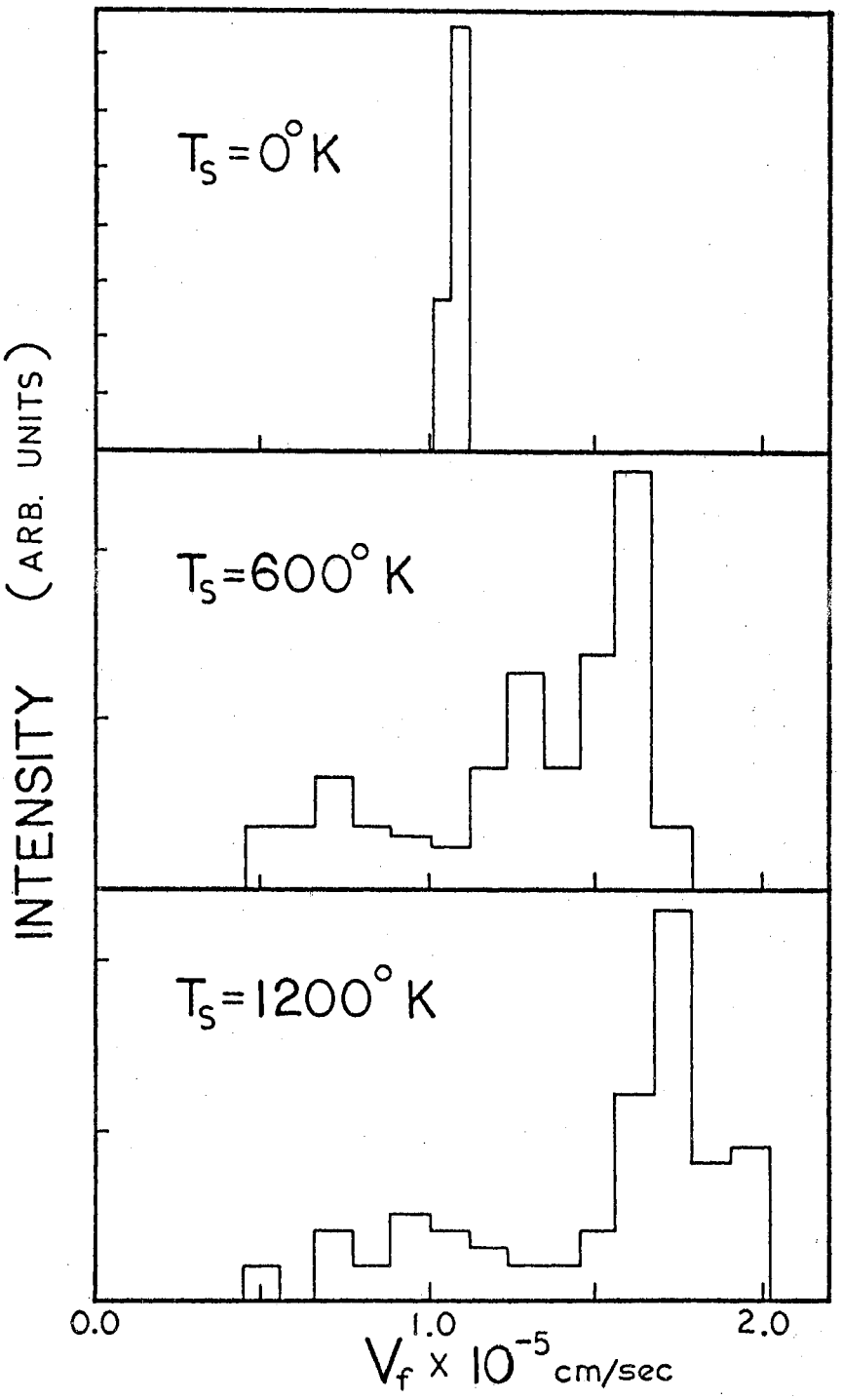

Figure 29. Variation of "In-Plane" Reflected Particle Velocity Distributions With Surface Temperature.

portion of the phase when the surface atom moves into the lattice, V_r decreases. As can be seen from Fig. 11, small V_r results in a large energy transfer from the gaseous particle to the surface. Thus, V_f is less than V_i; the ETC is positive, and the probability for trapping increases. On the other hand, as the lattice atom moves out of the surface in the positive $\not{z}$ direction, V_r increases and energy transfer from the lattice to the gaseous atom becomes significant. Then, V_f is greater than V_i; the ETC is negative, and the probability for trapping approaches zero.

This dependence of the energy transfer on lattice-vibrational-phase is shown for one particular trajectory in Fig. 30. The surface temperature is 1200°K. The $\not{z}$ coordinates of the gaseous particle and the central lattice atom are plotted as a function of time for seven trajectories that differ only in the phase of the surface atom at time of impact. The ETC for each trajectory is indicated. An ETC of unity means that the gaseous atom does not escape from the surface after the initial collision.

D. Conclusions

The 3D, classical model introduced previously has been employed to calculate spatial scattering and final velocity distributions for a (He/Ni) system as a function of incident velocity, beam temperature, and surface temperature. In general, the results indicate the following:

(1) The calculated results can be interpreted in

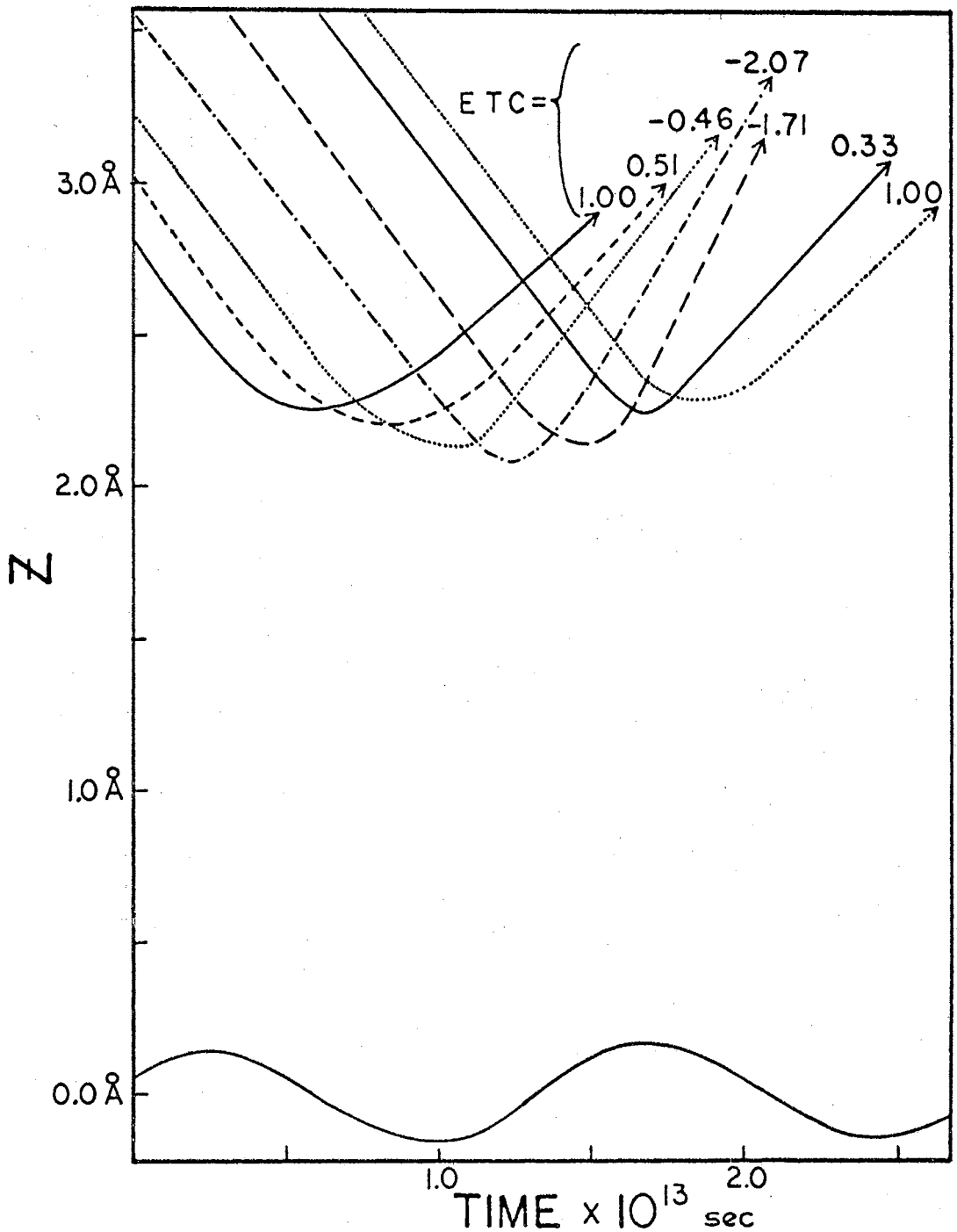

Figure 30. Dependence of Scattering on Lattice-Vibrational-Phase.

terms of the thermal scatter and structure scatter domains suggested by Oman.[77]

(2) The degree of broadness in the spatial distributions decreases with increasing V_i over the range studied.

(3) The spatial scattering peak positions approach the specular angle for large V_i. A supraspecular shift, which appears to be related to the interaction potential attractive wells, occurs for intermediate V_i. For small V_i the peak positions shift toward the surface normal.

(4) Velocity-selected and thermal beams are predicted to give similar spatial scattering distributions. This phenomenon results from the small, regular dependence of spatial scattering on V_i, which may or may not result from the thermal motion of the lattice depending upon whether thermal or structure scattering dominates.

(5) For surface temperatures in excess of 600°K, the spatial scattering is not a strong function of T_s. This observation could result from structure scatter dominating the thermal scatter.

(6) Reflected velocity distributions are disperse, non-Maxwellian, and tend to exhibit a bimodal structure. They are also more sensitive to the distribution of velocities in the incident beam and to surface temperature than are spatial distributions.

(7) Structure of the interaction potential surface causes more dispersion of spatial scattering than final velocities.

(8) For $(T_g/T_s) < 1$, some gaseous particles can still transfer energy to the lattice if the relative velocity of the gaseous and lattice atoms approaches zero during portions of the lattice-vibrational-phase.

In conclusion it can be stated that experimental measurement of final velocity distributions should be very informative. The model suggests that they may well be the most sensitive attribute of gas-solid interactions.

CHAPTER V

ADSORBED PARTICLES AND LATTICE IMPURITIES

A. Introduction

To this point only interactions with "clean" surfaces have been considered. However, the development of a general gas-solid interaction theory capable of treating adsorbed particles and lattice impurities is important since the great majority of experimental interactions occur at surfaces that have been contaminated by atmospheric gases. The interaction with a pure crystal lattice is observed only in rigorously monitored experiments. This chapter presents the results obtained by extending the 3D model to include adsorbed particles and lattice impurities. In general, it is found that the model qualitatively reproduces experimental observations for energy transfer and scattering distributions from contaminated surfaces. Section B discusses the formulation of the extended 3D model. In Section C the results of the interaction with adsorbed particles are given and discussed. In Section D the results for interactions with a surface containing lattice impurities are considered. The general results and conclusions are summarized in Section E.

B. Formulation

The basic lattice model of Chapter III is retained in the present model of the interaction process. The gaseous atom A is incident on the lattice face at some point P with initial velocity V_i at spherical polar incidence angles θ_i and ϕ_i. The scattering occurs at spherical polar angles represented by θ_f and ϕ_f at a reflected velocity V_f (see Fig. 1). The lattice face is again assumed to consist of nine movable sites in the (x-y) plane. These nine lattice sites are connected by harmonic springs to all nearest-neighbors. Figure 2 depicts the underlying lattice of the present model.

Adsorbed particles are incorporated into the surface model by including another layer of ten atoms above the basic FCC (111) lattice. The assumed configuration of the adsorbed layer with respect to the surface layer is shown in Fig. 31. The movable lattice sites are represented by the symbol O, the fixed lattice sites by X, the movable adatoms by ⊗, and the fixed adatoms by the symbol ●. The layer of fixed sites below the surface plane is still present in the model although they are not indicated. The unit cell for monolayer coverage is indicated by the dashed lines, and the actual aiming point area for trajectories is shaded.

A Lennard-Jones (12-6) pairwise type interaction potential is assumed to operate between each movable adsorbed particle and its nearest and next-nearest

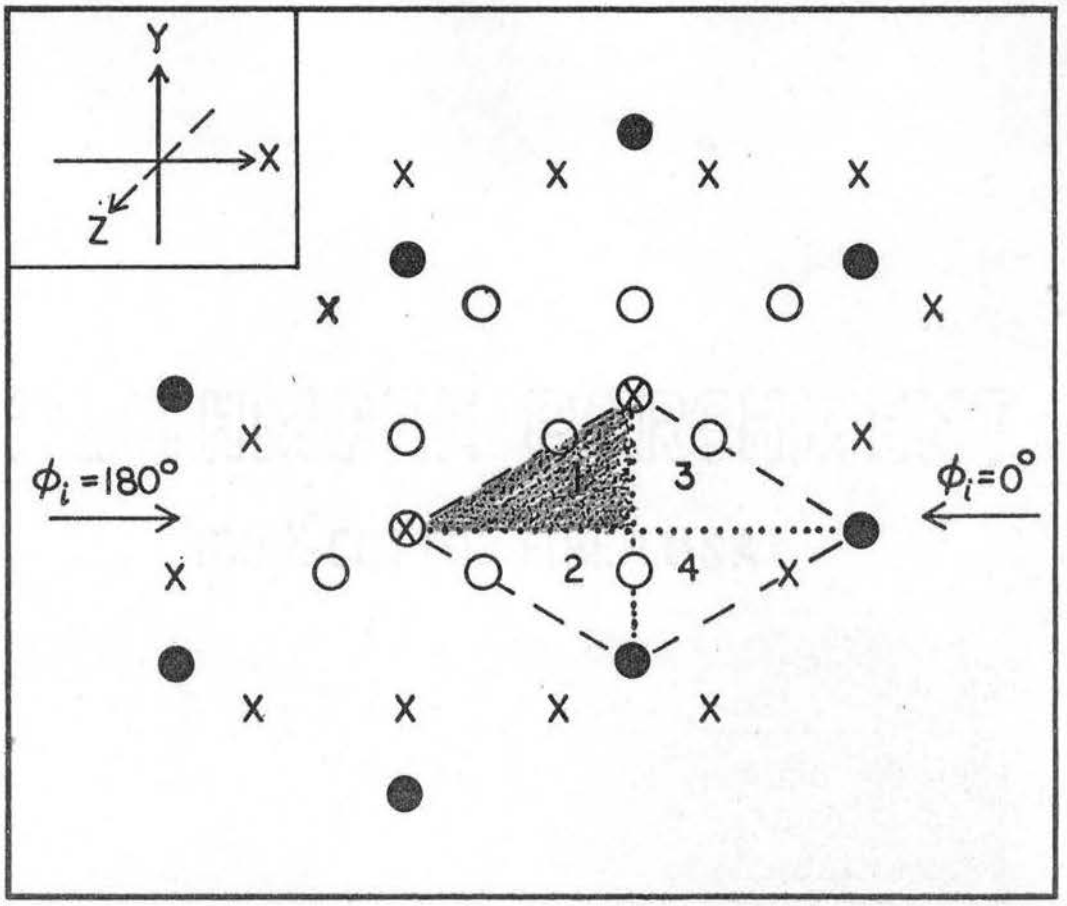

Figure 31: Surface Model for Adsorbed Particles. O, Movable Lattice Site; X, Fixed Lattice Site; ⊗, Movable Adparticle; ●, Fixed Adparticle. Dashed Lines Indicate the Unit Cell. Shaded Area is the Aiming Point Region.

neighbors in the crystal surface. Lennard-Jones potential terms also represent the interactions among nearest-neighbor adparticles. Morse potentials are assumed to operate between each movable particle and the incident gaseous atom. Thus, the overall interaction potential for the system is constructed from a sum of the 65 harmonic terms operating within the lattice, plus 11 Morse interaction terms operating on the incident gaseous particle, plus 23 Lennard-Jones terms for the movable adsorbed particles, i. e.

$$\mathcal{V} = \sum_{j=1}^{65} V_j^H + \sum_{i=1}^{11} V_{iA}^M + \sum_{k=1}^{23} V_{k\,Ad}^{LJ} \qquad (35)$$

The functional forms of the first two terms are given in Eq. (23). The Lennard-Jones term has the form

$$V_{k\,AD}^{LJ} = 4\epsilon \left[\left(\frac{\sigma}{R_k} \right)^{12} - \left(\frac{\sigma}{R_k} \right)^{6} \right] \qquad (36)$$

where R_k is the interparticle distance in the potential term denoted by $V_{k\,Ad}^{LJ}$; ϵ and σ are the usual Lennard-Jones potential parameters.

If ϵ is equated to zero for any pairwise interaction, the potential and the force between the two particles involved become zero, and they are effectively removed from the model. By this method the model can be made to represent a surface coverage of less than a monolayer. If all ϵ are equated to zero, the model reverts to the pure lattice of Chapter III. Impurity atoms within the lattice

can be simulated by changing the masses, force constants, and interaction potential parameters of lattice atoms.

The motion of the system is determined by the Hamiltonian equations which have the form given in Eq. (20). There are 12 rather than ten particles in the current model. Thus, 72 coupled differential equations must be solved. The initial position and momentum coordinates for the lattice atoms are the same as in Chapter III. The adsorbed particles of the monolayer are initially placed in the attractive wells existing above the centers of equilateral triangles formed by the lattice atoms. Their initial coordinates can be seen from Fig. 31 to be

$$
\begin{aligned}
X_{10} &= Re^{1}/2 \\
X_{11} &= -Re^{1} \\
Y_{10} &= 3^{1/2}\ Re^{1}/6 \\
Y_{11} &= -Re^{1}\ (1 - 3^{1/2}/6) \\
Z_{10} &= Z_{11} = Re^{Ad} \ .
\end{aligned}
\tag{37}
$$

The equilibrium distance in the Z direction for the adatoms Re^{Ad} is determined by numerically locating the point of zero net force. For a nonzero surface temperature T_s the initial momenta of the lattice and adsorbed particles are assigned as in Eq. (26). The initial variables for the gaseous atom are also assigned as in the previous model except for the minor alteration of starting the gaseous particle 12Å from the surface. This modification is

required because the layer of adparticles increases the range of the interaction.

C. Adsorbed Particles

1. Numerical Analysis

The motion equations were numerically integrated by an Adams-Moulton[85] procedure on an IBM 7040. Although the system of equations is somewhat more complicated, the computer time per trajectory remained about the same due to efficiency procedures introduced into the program. A systematic averaging over surface aiming points was carried out by a procedure similar to that described in Chapter III. The shaded area of Fig. 31 was scanned with 78 trajectories. Although this represents only one-fourth of the unit cell, reflection symmetry was assumed to give a second quarter for the case of $\phi_i = 0^\circ$. (It should be noted that reflection symmetry does not actually exist in the present model because of the underlying lattice configuration. The assumption is valid only if the layer of adparticles dominates the interaction.) The third quarter was obtained by setting $\phi_i = 180^\circ$, calculating 78 additional trajectories and then transforming the resulting ϕ_f's through 180°. Thus, by calculating two sets of trajectories aimed at points within the shaded region, one with $\phi_i = 0^\circ$ and the other with $\phi_i = 180^\circ$, the scattering from an entire unit cell for $\phi_i = 0^\circ$ was predicted.

The unit cell for a half-monolayer of adparticles is indicated by the dashed lines in Fig. 32(a). The aiming point area is shaded. Four sets of trajectories were calculated to scan the unit cell. The first-eighth was calculated for $\phi_i = 0^\circ$, and the second was obtained by reflection. The third and fourth octants were obtained as above by performing the calculations for $\phi_i = 180^\circ$ and transforming the results. The remainder of the unit cell was scanned by changing the adparticle configuration to that of Fig. 32(b). A set of trajectory calculations for $\phi_i = 0^\circ$ gave the fifth octant of the unit cell and reflection gave the sixth. The seventh and eight were calculated for $\phi_i = 180^\circ$ and transformed. Thus, the model reproduced scattering from an entire unit cell for monolayers or half-monolayers even though the aiming points were restricted to a confined region. This restriction is required because the model only includes interaction terms between the gaseous atom and 11 localized surface atoms. It also permits the best possible statistical averaging with a given number of trajectories.

The system chosen for study was He interacting with Ar adsorbed on a Ni FCC (111) lattice. The (He/Ar/Ni) system allowed the use of the (He/Ni) and (Ni/Ni) parameters of Table I so that a comparison of pure and contaminated surface interactions is possible. Since the interaction parameters for the noble gases are known, the (He/Ar) and (Ar/Ar) potential interactions could be accurately estimated.

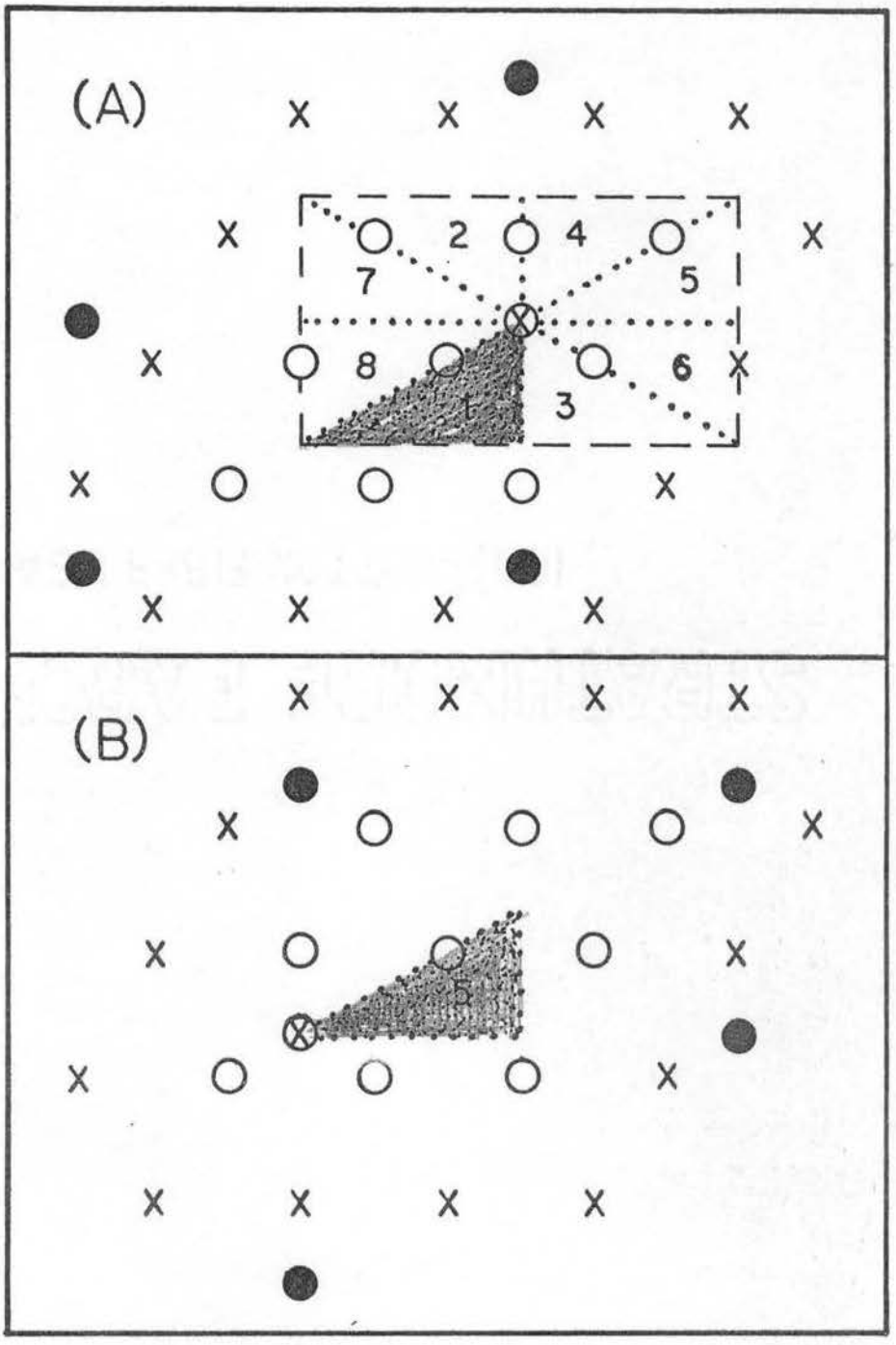

Figure 32: (a) Surface Model for a Half-Monolayer of Adparticles. (b) Complementary Surface Model for a Half-Monolayer.

Table II lists the values of the interaction potential parameters employed for the system. The resulting value of Re^{Ad} of Eq. (37) is 3.36254 Å.

TABLE II

(He/Ar/Ni) POTENTIAL SURFACE PARAMETER VALUES.

Parameter	Surface	Value	Reference
D	(He/Ar)	0.00218eV	90
α	(He/Ar)	1.71 $Å^{-1}$	46
Re	(He/Ar)	4.2 Å	—
k	(Ar/Ar)	0.248eV/$Å^2$	91
Re^1	(Ar/Ar)	5.43 Å	92
ϵ	(Ar/Ni)	0.018eV*	74
σ	(Ar/Ni)	3.33 Å	74
ϵ	(Ar/Ar)	0.00267eV*	93
σ	(Ar/Ar)	3.42 Å	93

*These well depths are one-fourth of the literature values. It has been pointed out by Oman[78] and in Chapter III that the usual pairwise well depth parameters give excessively large attractive wells when summed over a number of pairs.

2. Results and Discussion

The potential contour lines for the three model surfaces are illustrated in Fig. 33. The shaded plane in the inset shows the portion of the surface being considered. The solid lines represent the contours for He interacting with pure Ni. The dashed lines indicate the surface for a half-monolayer of Ar and the dotted lines are the Ar monolayer surfaces. For this particular plane a half-monolayer of Ar causes a dramatic increase in surface "roughness." (Throughout this chapter surface roughness refers to periodic variations in the surface interaction potential rather than geometric, macroscopic roughness.) The change is noticeable but not so large for other planes through the surface. The Ar monolayer produces a surface that is almost as smooth as pure Ni, but the attractive wells are not as deep. The effects of these surface differences on the interaction characteristics are pointed out below.

The interdependence of aiming point, $\alpha_E(\theta_i,\phi_i)$, and scattering angles θ_f and ϕ_f is indicated in Fig. 34. The calculations shown are for the (He/Ar(monolayer)/Ni) system with the initial conditions of $\theta_i = 37.5^\circ$, $\phi_i = 0^\circ$, $V_i = 1.58 \times 10^5$ cm/sec, and $T_S = 0^\circ$K. The resulting values of $\alpha_E(\theta_i,\phi_i)$, θ_f, and ϕ_f are shown for 21 trajectories distributed over the upper half of the unit cell. The origin of each vector represents the turning point of that

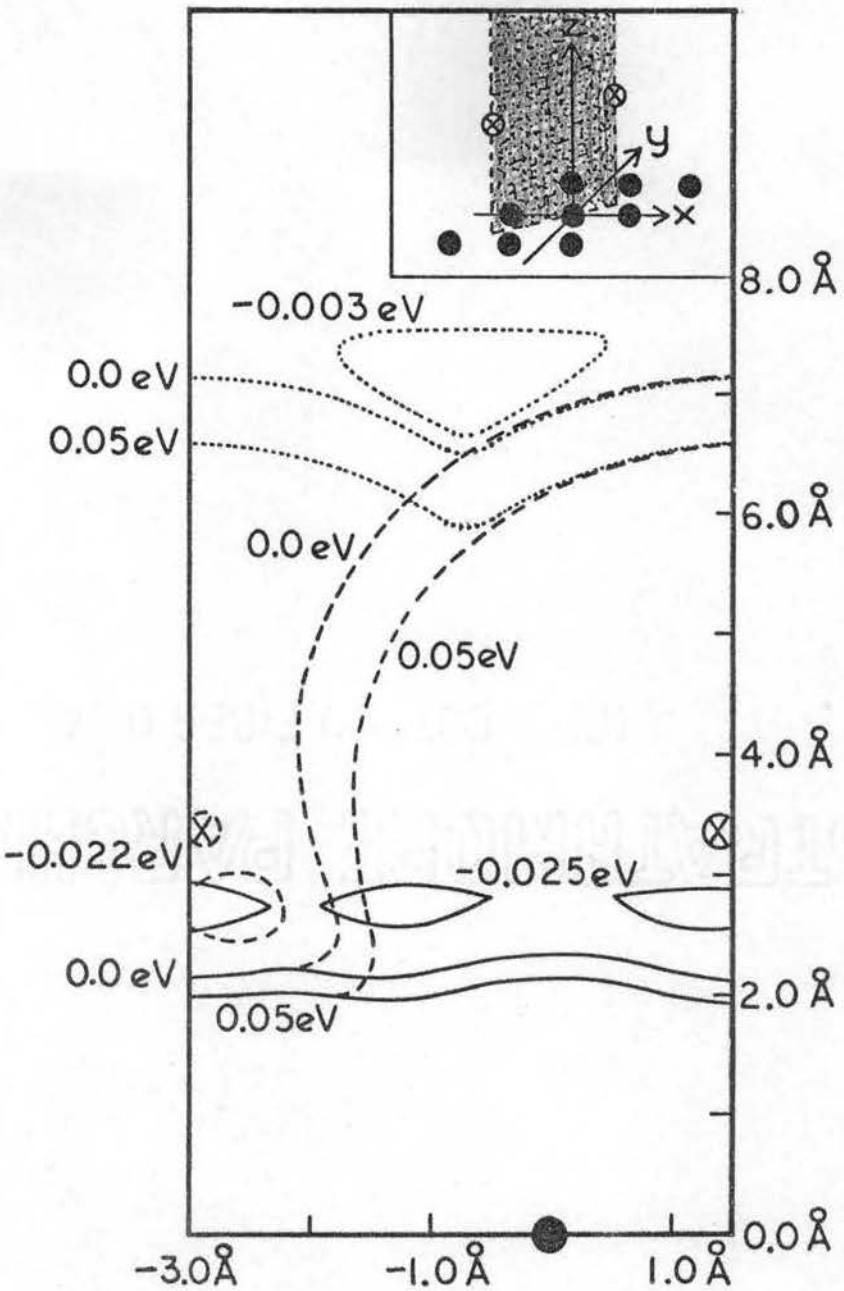

Figure 33: Potential Surface Contour Lines (_____), He/Ni; (– – –), He/Ar(Half-Monolayer)/Ni; (.....), He/Ar (Monolayer)/Ni.

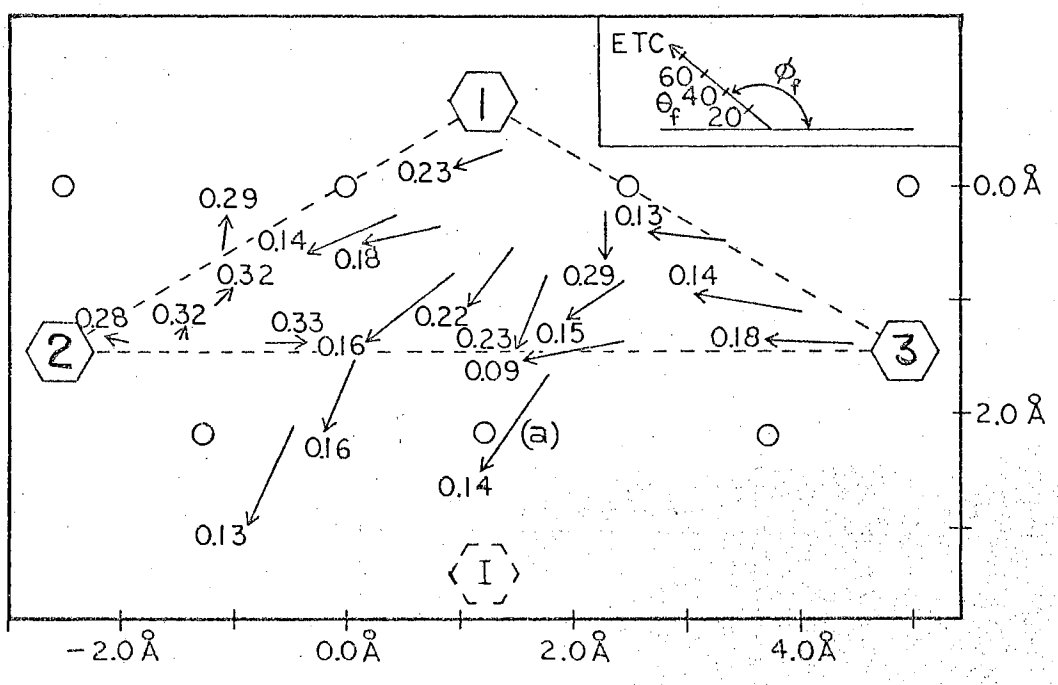

Figure 34: Interdependence of Aiming Point, $\alpha_E(\theta_i, \phi_i)$, θ_f, and ϕ_f.

trajectory, i. e., the point in the (x-y) plane where the z component of momentum for the gaseous particle changes from negative to positive. The direction of the vector gives the out-of-plane scattering angle ϕ_f; a horizontal position to the left indicates $\phi_f = 180^\circ$. The length of the vector represents θ_f according to the scale shown in the inset. The calculated $\alpha_E(\theta_i, \phi_i)$ for each trajectory is given by the number at the head of the vector. Several general features of the interaction can be noted from the figure.

(a) The scattering is dominated by the adsorbed layer of Ar. Comparison with Fig. 10, in which scattering from pure Ni is depicted, indicates that atoms of the substrate have, at most, a secondary effect. This observation is in accord with results reported earlier by Oman.[75] The reflection symmetry assumption used to obtain scattering from an entire unit cell as was described in Section C.1. can be seen to be justified by this result.

(b) Scattering from the adsorbed Ar results in more "backscatter" (scatter back toward the incidence angle) than was predicted for a pure Ni surface (compare with Fig. 10).

(c) Particles that interact strongly with adatoms to be backscattered have higher values for the ETC.

(d) The amount of out-of-plane scatter ($\phi_f \neq 180^\circ$) is increased due to the inadequate size of the model. For example, the trajectory represented by the vector labeled

(a) is scattered at $\phi_f = 236^\circ$ due largely to its replusive interaction with Ar(1) at the top of the unit cell. In the model calculation there is no interaction between Ar(I) and the gaseous particle. In reality this interaction is approximately equal to that from Ar(1) for trajectories in the area of (a). This additional interaction would cause the scattering to be more nearly in-plane for trajectories in this region.

The average ETC of the calculated trajectories with this set of initial conditions is 0.21 if four trapped particles are neglected. If the four trapped particles are assumed to be completely accommodated (ETC = 1.0) and included in the averaging, the ETC is 0.23. The true value should lie somewhere between these two extremes. For the case of a half-monolayer of Ar adatoms, 44% of the trajectories result in trapped particles. The ETC is calculated to be 0.21 if the trapped particles are ignored and 0.54 if they are included in the averaging as being completely trapped. The corresponding initial conditions on a pure Ni surface gave an ETC of 0.11 with no trapped particles, as was reported in Chapter III. The same conditions were employed for He interacting with a pure FCC(111) Ar lattice using the appropriate parameters of Table II; the resulting ETC is 0.23.

The above values for the ETC are plotted against surface coverage in Fig. 35. Experimental bulk AC's for a (He/K/W) system[14] are also included for comparison. Both

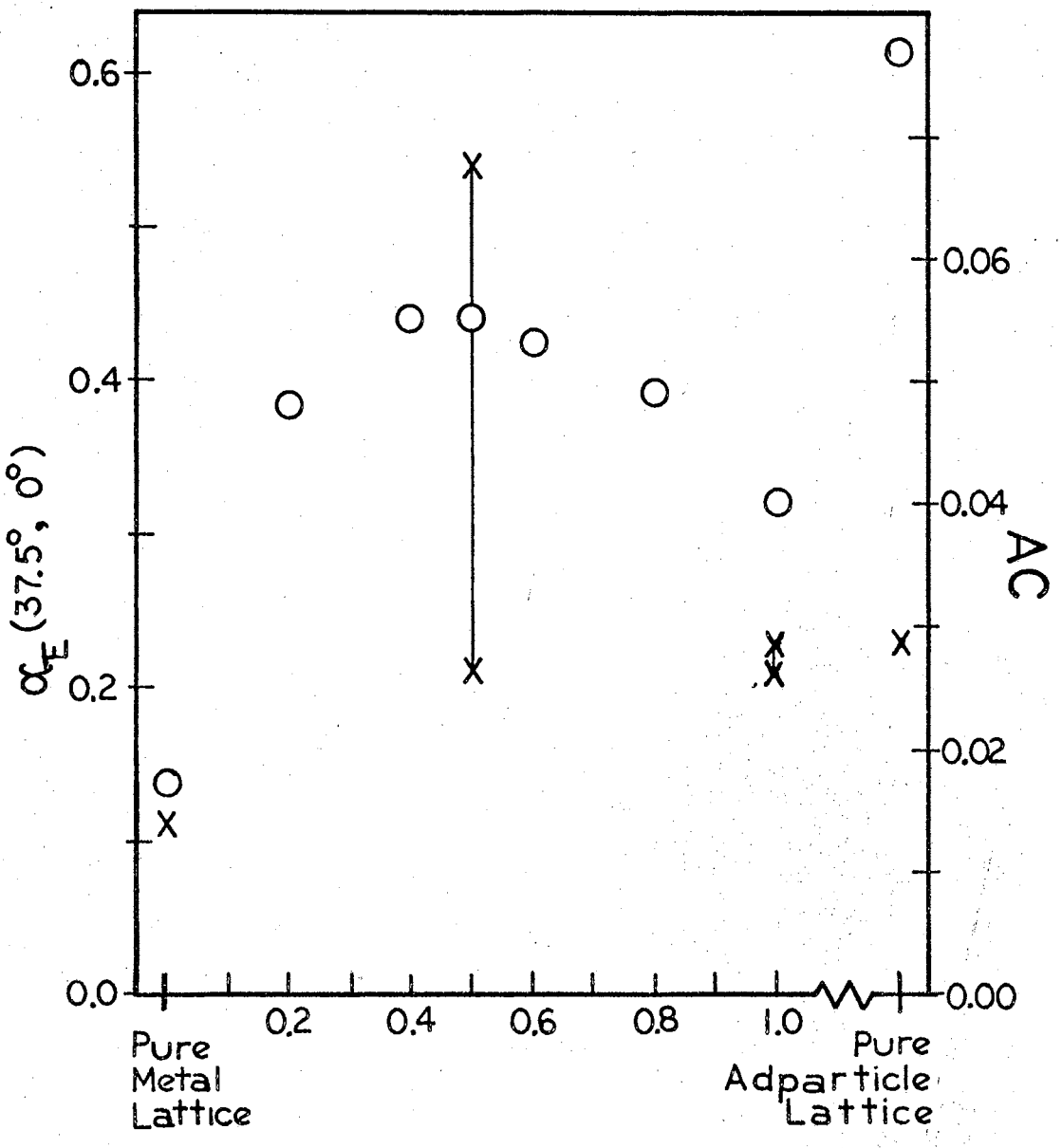

Figure 35: Variation of Energy Transfer With Surface Coverage. X, Calculated $\alpha_E(37.5°, 0°)$ Values for (He/Ar/Ni); O, Experimental AC Values for (He/K/W).

the theory and experiment exhibit energy transfer maxima at half-monolayer coverage. The model gives this result because of the greatly increased surface roughness for a half-monolayer. Specular scattering is highly probable for relatively smooth surfaces, and this results in minimum energy transfer with little trapping. A rough surface increases the occurrence of backscattering, multiple collisions, and trapping and thus, increases the energy transfer.

The effect of the rough half-monolayer surface on one particular trajectory is shown in Fig. 36. For monolayer coverage the trajectory with this set of initial conditions was scattered quasi-specularly after a single collision at $\theta_f = 56.8^\circ$, $\phi_f = 259.6^\circ$ with ETC = 0.17. For half-monolayer coverage collision with the adatom causes the particle to be initially backscattered parallel to the surface at $\theta_f = 89.4^\circ$, $\phi_f = 3.7^\circ$ with ETC = 0.29. This trajectory is denoted by the solid curve. Due to the finite nature of the 12-body model, these are normally the predicted final scattering conditions. Since $\theta_f > 85^\circ$, this trajectory result was neglected in calculating the lower ETC limit of Fig. 35 and was considered to be fully accommodated in calculating the upper limit. The interaction that would result from an infinite lattice can be approximated by translating and reflecting the lattice model at the instant the gaseous particle leaves the aiming point region (shaded area of Fig. 36). This transformation, which

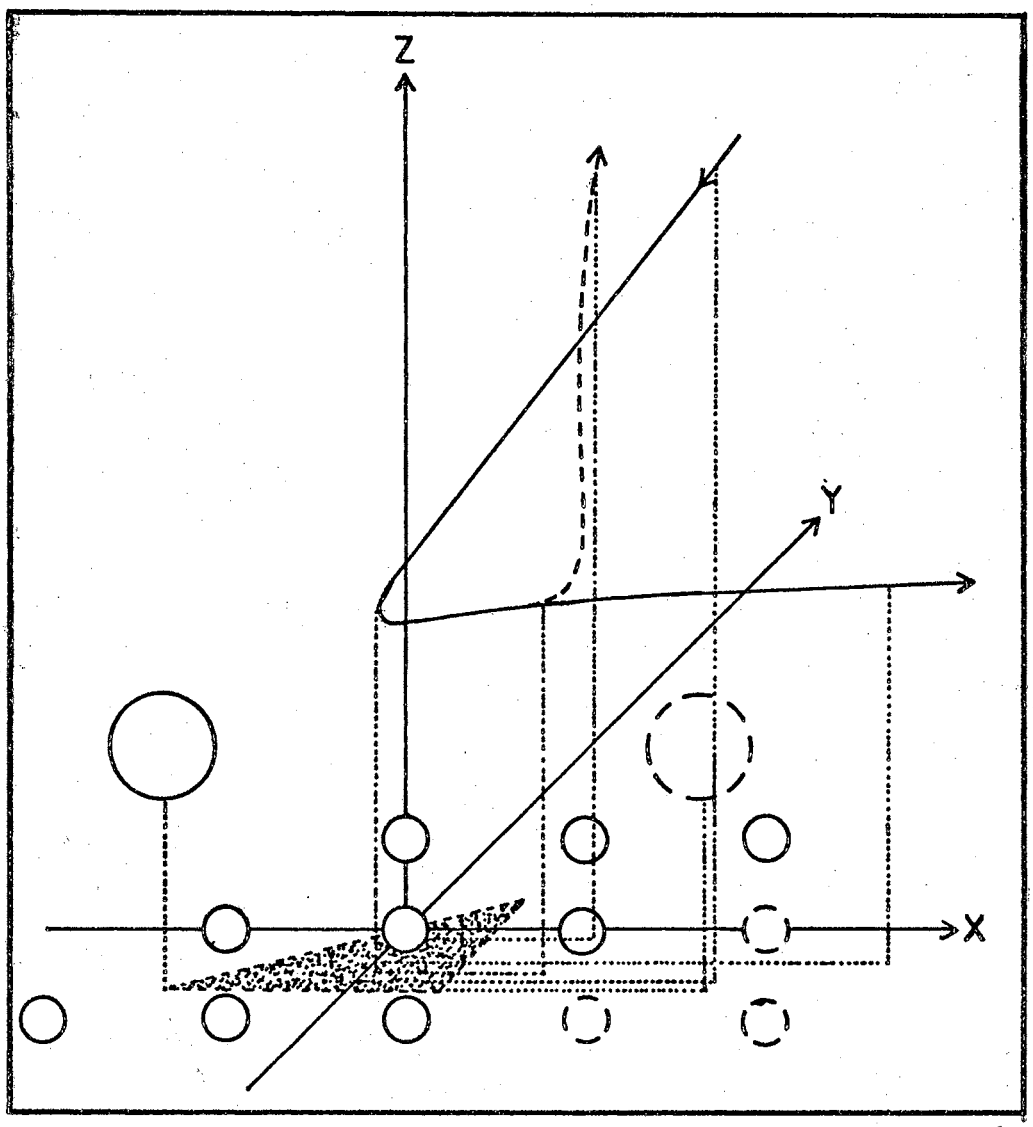

Figure 36: Trajectory for Half-Monolayer Coverage. Solid Curve Trajectory Results From Simple Ten-Body Lattice (Solid Circles). Dashed Trajectory Results From Translating and Reflecting the Lattice (Dashed Circles) so the Interaction Always Occurs Above the Shaded Region.

effectively keeps the particle above the aiming point region, can be continued until the interaction is complete. The particle can then be studied as it interacts with a second adatom to transfer additional energy. The results of a complete calculation, indicated by the dashed curve, are $\Theta_f = 10.9^\circ$, $\phi_f = 81.6^\circ$, and ETC = 0.55. This type of computation could be carried out for all trajectories not completed over the original aiming point region, and the actual ETC's rather than their limiting values could be calculated. This was not done because the computation times become excessive.

In Fig. 37 the variation of the ETC with $\epsilon_{Ar/Ni}$ (the Lennard-Jones binding strength between Ar and Ni) and the mass of the adparticles, M_{Ad}, is illustrated for initial conditions of $\Theta_i = 0^\circ$, $\phi_i = 0^\circ$, $V_i = 1.58 \times 10^5$ cm/sec, and $T_S = 0^\circ$K. The interaction is with a monolayer. Decreasing M_{Ad} from 40 amu to 20 amu increases the energy transfer considerably. Further calculations with variable gaseous atom mass M_g indicate that the ETC increases as the ratio (M_g/M_{Ad}) approaches unity. This result is in agreement with the mechanics of hard-sphere collisions. Increasing the binding strength between the lattice and adsorbed particles causes the ETC to decrease; the effect becomes greater as (M_g/M_{Ad}) approaches unity.

For all cases plotted in Fig. 37 the binding strength between the adparticles, $\epsilon_{Ar/Ar}$, is 0.00267 eV. Increasing

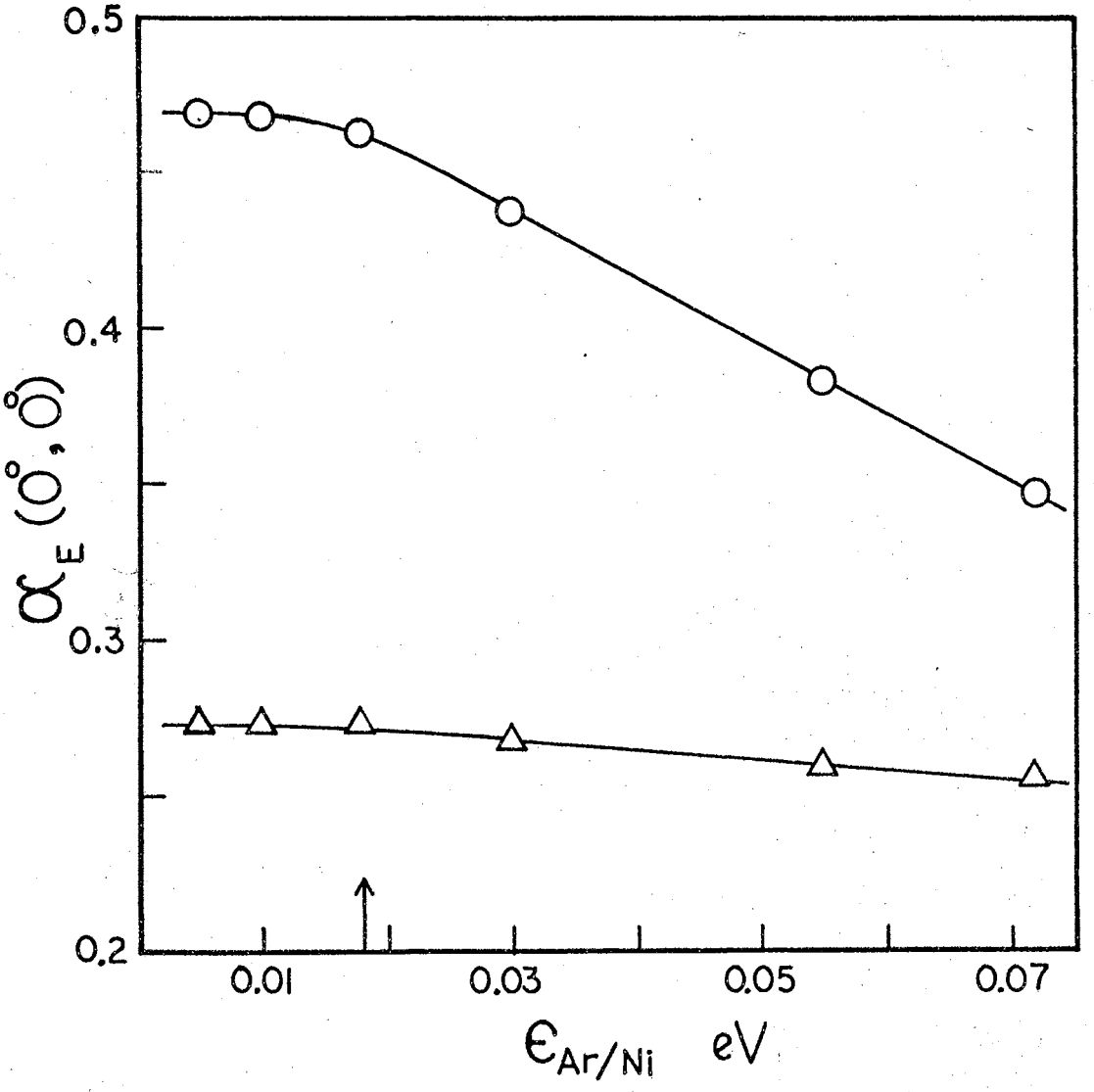

Figure 37: Variation of $\alpha_E(0^\circ, 0^\circ)$ With Adatom-Lattice Binding Strength and Adatom Mass. Δ, Adatom Mass = 40 amu; O, Adatom Mass = 20 amu.

this parameter to 0.06 eV causes no significant change in the calculated ETC. For the gas-solid interaction of the model it appears that the binding between the adparticles and the lattice dominates over the binding among adparticles. It should be noted, however, that the present 12-body model does not properly treat surface mobility of adatoms. Movement over the unit cell of the FCC(111) substrate lattice is possible, but the model is not large enough to properly allow movement over several lattice unit cells. Binding among adparticles could have an effect for realistic adatom motion.

Sputtering of adparticles by incident He was calculated in several trajectories for small $\epsilon_{Ad/Ni}$ values. More extensive calculations for these conditions would provide an interesting prediction of spatial and velocity distributions of sputtered surface atoms.

In Fig. 38 the variation of the ETC with the initial lattice-vibrational-phase parameter (Z^1 of Eq. (28)) for one specific trajectory is indicated. For these calculations $\Theta_i = 0^\circ$, $\Phi_i = 0^\circ$, $V_i = 1.58 \times 10^5$ cm/sec, and $T_S = 700^\circ$K. The coverage is a monolayer. One complete (Ni/Ni) lattice vibration is indicated by $Z^1 = 1.0$. Since the adparticles are weakly bound, their vibration phases are longer by a factor of about 3.5. The adparticle vibrations are also anharmonic. As a result, the variation of the ETC with Z^1 is not periodic as was the case for the

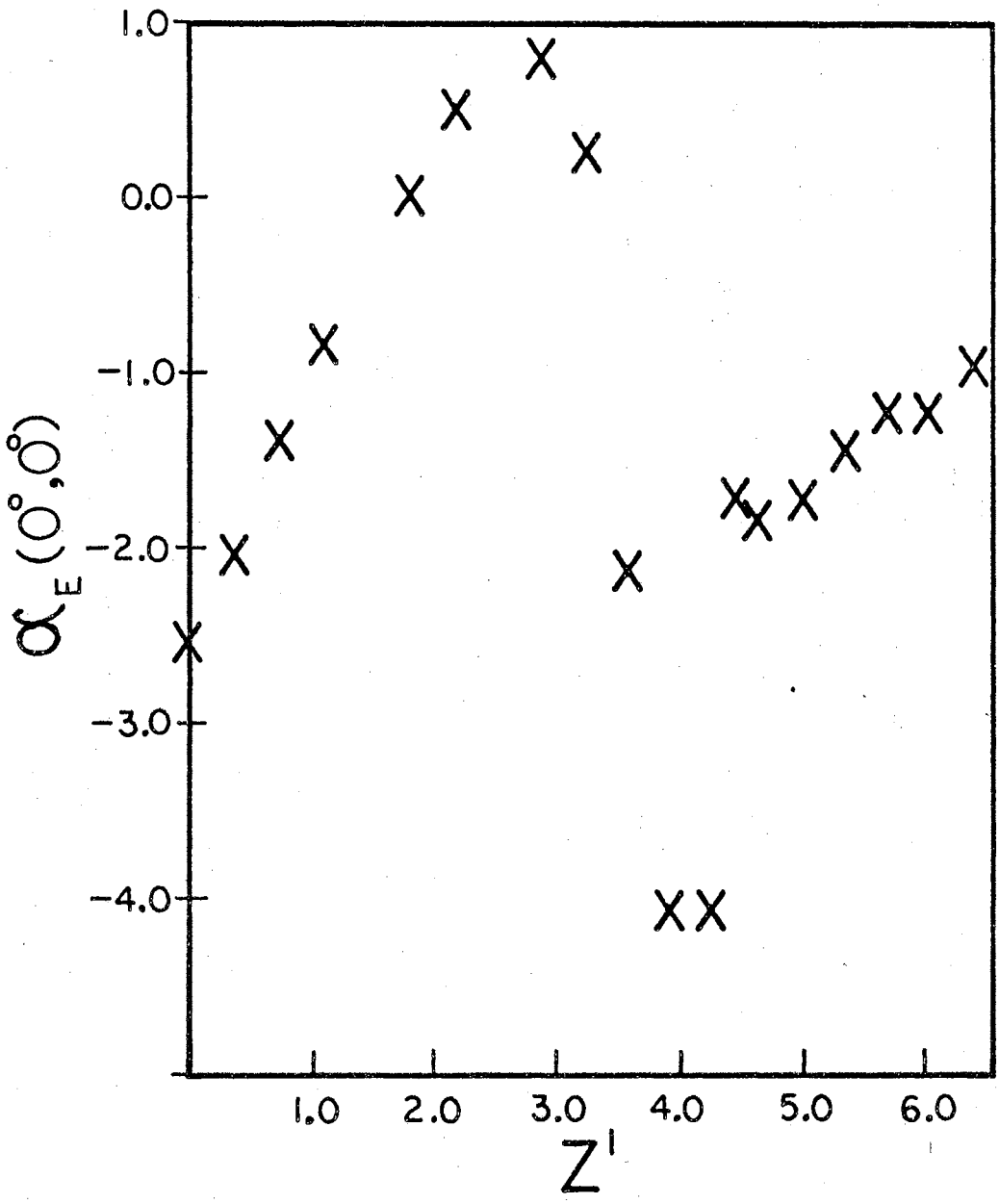

Figure 38: Variation of $\alpha_E(\theta_i, \phi_i)$ With Lattice-Vibrational-Phase Parameter Z^1 for a (He/Ar(Monolayer)/Ni) System.

pure Ni lattice (see Fig. 13). In that case six evenly distributed values of Z^1 were used to calculate trajectories for each point to effectively average over lattice phase. Thus, for a contaminated surface with $T_S \neq 0^\circ K$ a large number of trajectory calculations or an interpolation technique, such as that employed by Oman,[77] would be required for a complete study of the interaction. Such extensive calculations were not carried out because of the rather qualitative nature of the results produced by the model.

Figure 39 gives the "in-plane" scattering distributions (Θ_f's for trajectories in which $160^\circ < \phi_f < 200^\circ$) for He interacting with (a) a pure Ni lattice, (b) a half-monolayer of Ar on Ni, (c) a monolayer of Ar on Ni, and (d) a pure Ar lattice. The initial conditions are $\Theta_i = 37.5^\circ$, $\phi_i = 0^\circ$, $V_i = 1.58 \times 10^5$ cm/sec, and $T_S = 0^\circ K$. As the surface progresses from pure Ni to an Ar layer to pure Ar, the scattering distributions show significant changes. For a Ni lattice a single, quasi-specular lobe is predicted. A half-layer of Ar causes some backscattering and a noticeable decrease of the "in-plane" scattering intensity. The structure in the backscatter is statistical fluctuation and has no particular significance. An increased amount of forward scattering with some structuring occurs for an Ar monolayer. The Ar lattice gives a forward scattered bimodal distribution. These changes are reasonable in view of the surface roughness differences that were illustrated in Fig. 33. The pure Ni surface

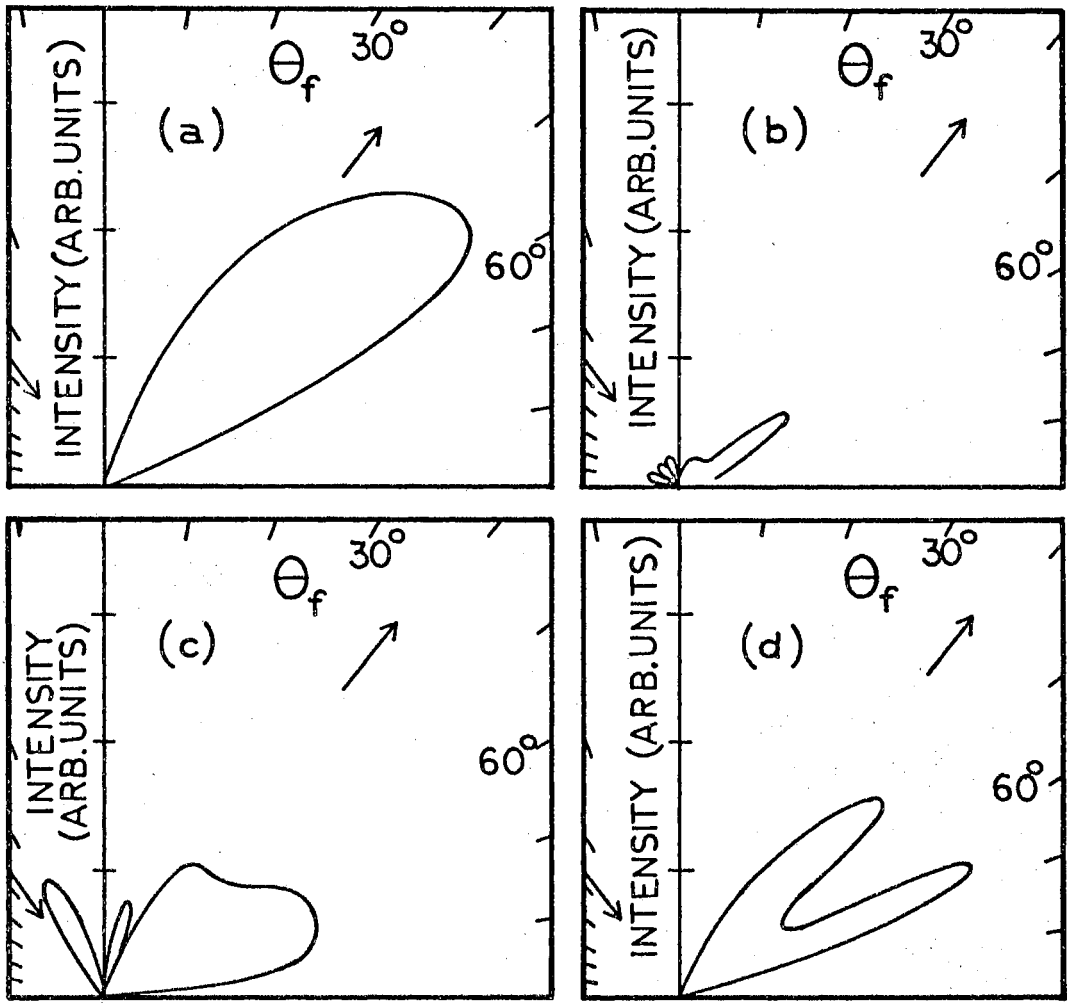

Figure 39: Variation of "In-Plane" Scattering Distributions With Surface Coverage. (a) He/Ni. (b) He/Ar(Half-Monolayer)Ni. (c) He/Ar (Monolayer)/Ni. (d) He/Ar.

appears relatively smooth to He particles with a V_i of 1.58×10^5 cm/sec. Thus, specular type collisions are highly probable. The protruding Ar atoms of a half-monolayer cause a significant amount of backscatter, out-of-plane scatter, and scatter which leads to multiple collision (see Fig. 36). With a monolayer of Ar the surface is relatively smooth; the amount of backscatter decreases and the forward peak intensity increases. It is interesting to note that three peaks result from the Ar monolayer; these are qualitatively similar to the backscatter, quasi-normal, and quasi-specular peaks observed experimentally for Ar reflected from dirty silver by Alaclay and Knuth.[40] The calculations were not extensive enough to determine the reproducibility or the origin of the quasi-normal peak.

The prediction of a double-lobed scattering distribution from the Ar surface but not from the Ni surface under identical conditions is both interesting and puzzling. Bimodal distributions have been experimentally obtained for (He/Pt),[3] (Ag/Mo)[39] and probably for (He/Ag)[31] but not for (He/Ni)[33] or (He/W).[43] The reasons for the differences are not obvious from experiments. It was suggested in Chapter III that the bimodal distributions result from the accelerating effect of the attractive well of the interaction potential. However, the well depth parameter for the (He/Ar) interaction is only 0.00218 eV while that for (He/Ni) is 0.00564 eV. Furthermore, Palmer,

Saltsburg, and Smith[34] have recently pointed out that this explanation is inconsistent with the experimental observation that (He/Ni) exhibits sharper peaks and less structure than that found for the (He/Ag) system. Clearly, factors other than the well depth must be important in the production of a bimodal scattering distribution.

The various parameters in the (He/Ar) interaction were varied independently to determine the origin of the bimodal distribution. The results indicate that both surface roughness and the attractive wells are important factors. The extent of bimodal structuring increases with increased attractive well depth as in Chapter III. However, it is observed that large well depths cause all particles to be scattered at large angles into a single lobe. Increasing the roughness of the surface potential contour lines by increasing the Morse range parameter α or the equilibrium lattice spacing R_e[1] causes the structuring to increase. Therefore, it appears that the structuring is present in (He/Ar) scattering because the equilibrium lattice spacing and range parameter are larger and create a rougher surface than for the (He/Ni) system. Since the Ag lattice spacing is 16% greater than that for Ni, a similar explanation appears to account for the observations made by Palmer, Saltsburg, and Smith.[34] Clearly, the structuring effect is complex, and while the present model is sufficient to explain the presence or absence of such structure, it is inadequate to predict whether or not bimodal structure

will be present in a given system without an a priori knowledge of the interaction potential.

The out-of-plane scattering distributions that result from the different surfaces are shown in Fig. 40. Only half of each distribution is shown since the unit cell has been scanned in such a manner as to make the scattering symmetric. The initial conditions are the same as in Fig. 39. The decrease of in-plane intensity and increase of backscattering caused by Ar adparticles is clearly illustrated. Although the model somewhat overemphasizes the amount of out-of-plane scatter from contaminated surfaces, experimental measurements of ϕ_f and backscatter distributions should give an indication of the degree of surface cleanliness.

D. Lattice Impurities

1. Numerical Analysis

Since contaminated surfaces result from lattice impurities as well as adsorbed particles, it is important to investigate the effects of impurity atoms which are a part of the surface layer. The present model was employed to study the possible effects of oxygen as a lattice impurity in a Ni FCC(111) crystal. This system is interesting because Smith and Saltsburg[30] are uncertain of the purity of the epitaxial "Ag" surface employed in their work and suggest, in view of LEED studies,[94] that a stable silver oxide surface could exist.

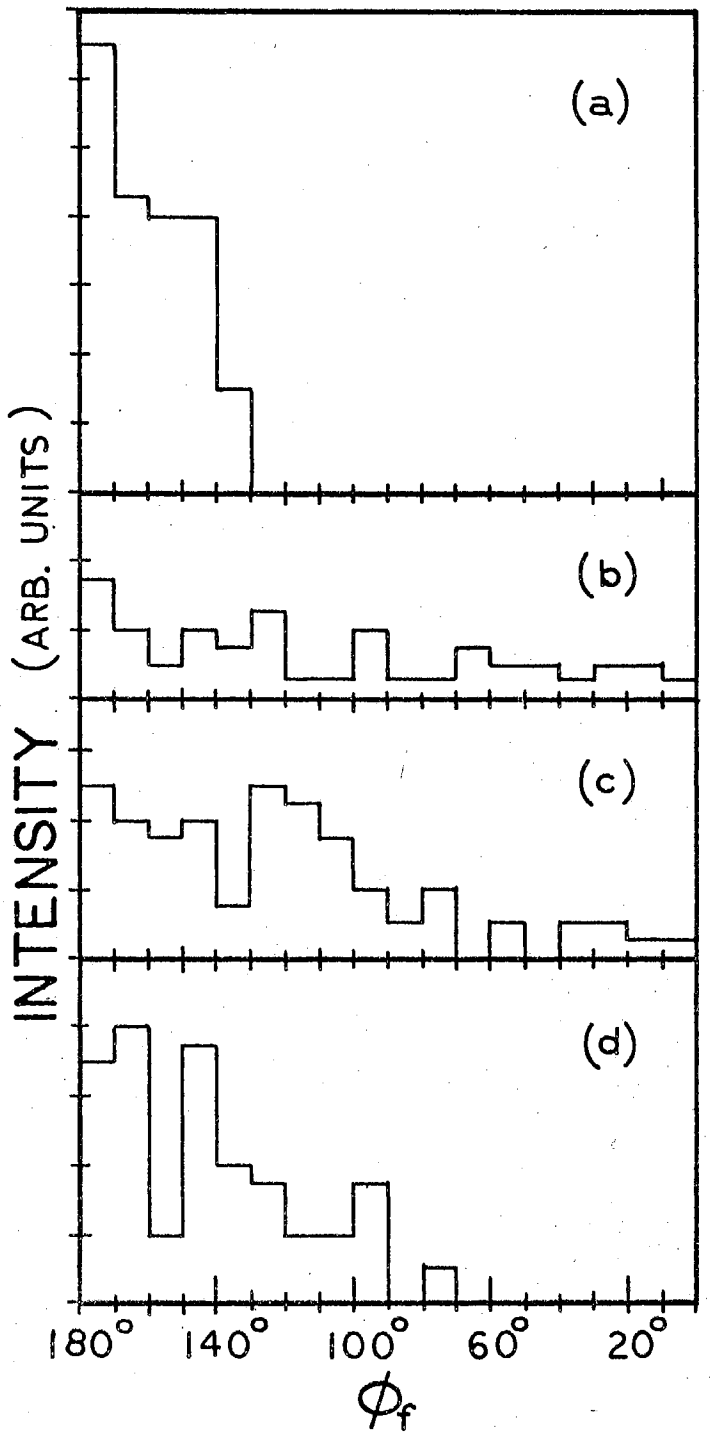

Figure 40: Variation of Out-of-Plane Scattering Distributions With Surface Coverage. (a) He/Ni. (b) He/Ar (Half-Monolayer)/Ni. (c) He/Ar (Monolayer)/Ni. (d) He/Ar.

Nickel atoms in the model were replaced by oxygen atoms to form the (2 x 2) reconstructed surface oxide of Ni depicted in Fig. 41(a). Movable Ni atoms are represented by O, fixed Ni atoms by X, movable oxygen atoms by ⊗, and fixed oxygen atoms by ●. The layer of atoms below the surface, which is not shown in the figure, is composed of fixed Ni atoms (see Fig. 2). The unit cell for this surface is four times as large as for the pure lattice. Hence, trajectory calculations on four different ten-body models were required to span the unit cell. In the first, denoted by I, atoms 1, 3, 7, and 9 are oxygen. To obtain scattering from quadrant II, the model shown in Fig. 41(b), where atoms 4, 6, and the appropriate fixed atoms are oxygen, was employed. The III and IV quadrants were also represented by appropriate positioning of impurity atoms.

The parameters chosen to represent the oxygen atoms and their interactions are shown in Table III. The force constant between the Ni and O atoms, $k_{Ni/O}$, was approximated from the Debye temperature of NiO[95]. The equilibrium distance, $Re^{1}_{Ni/O}$, is the same as for the (Ni/Ni) interaction. The Morse $\alpha_{He/O}$ and $Re_{He/O}$ parameters were obtained from the usual combining rules using the (He/He) and (O/O) Morse parameters. Because of the large difference in magnitude between the well depth parameters of the (He/He) and (O/O) interactions, the combining rule does not work well. Therefore, the $D_{He/O}$ value was estimated so

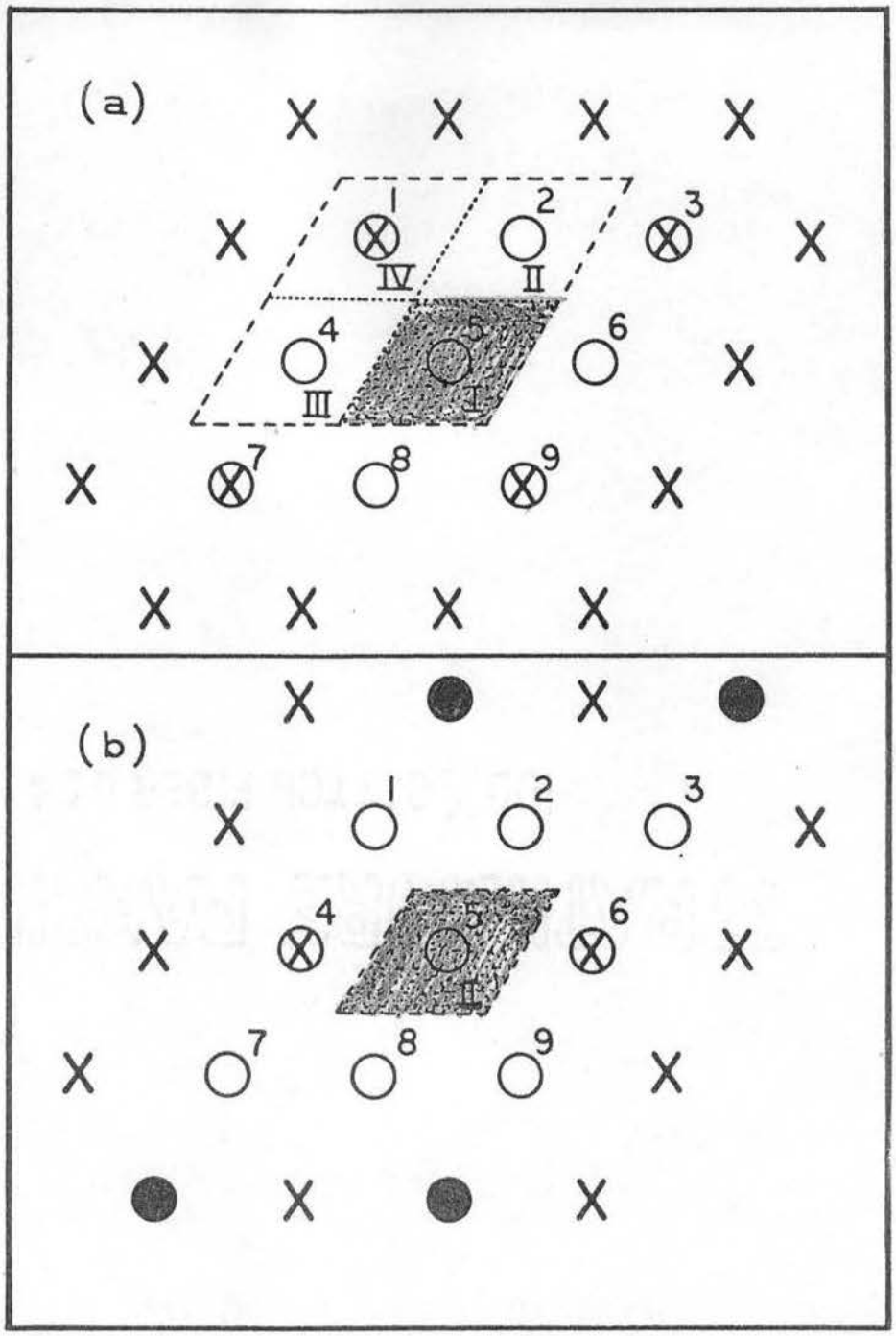

Figure 41: (a) Surface Model for Impure Lattice. O, Movable Lattice Atom; X, Fixed Lattice Atom; ⊗, Movable Lattice Impurity Atom; ●, Fixed Lattice Impurity Atom. (b) Quadrant II Scattering Model.

as to be consistent with the best-fit parameters obtained by the "soft cube" model of Logan and Keck.[71]

TABLE III

(He/Ni x O) POTENTIAL SURFACE PARAMETER VALUES

Surface Parameter	Value
$k_{Ni/O}$	7.9eV/Å^2
Re^1	2.49Å
M_o	16.0 amu
$D_{He/O}$	0.01eV
$\alpha_{He/O}$	2.37Å^{-1}
$Re_{He/O}$	2.17 Å

2. Results and Discussion

The surface potential contour lines for the (He/Ni x O) system are shown in Fig. 42. The impurity atoms can be seen to create a rather rough surface with deep attractive wells. It is doubtful that the oxide surface has been quantitatively portrayed. Nevertheless, it is hoped that the results qualitatively reproduce scattering from an impure surface and can provide some information for the

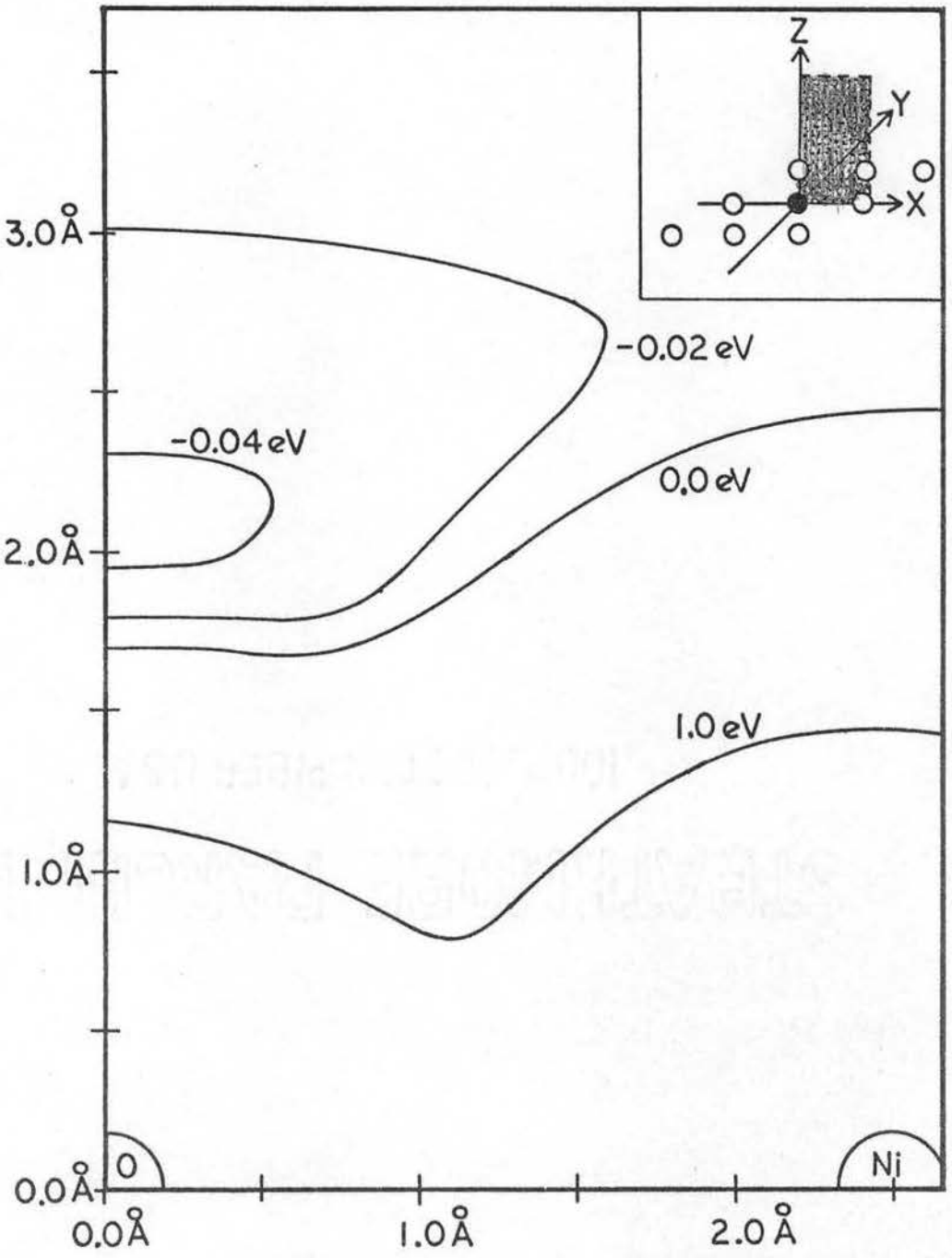

Figure 42: Potential Surface Contour Lines for the (He/Ni x O) System. Shaded Area in the Inset Shows the Plane Being Considered.

interpretation of experiments. In view of the recent uncertainty regarding reconstructed surfaces,[96,97] it is possible that Fig. 42 is not even qualitatively correct. For the case of an oxygen anion layer above the Ni lattice, the adparticle model described in Section C would be more representative.

The calculated "in-plane" scattering distribution for the (He/NixO) system with $\Theta_i = 37.5^\circ$, $\phi_i = 0^\circ$, $V_i = 1.12 \times 10^5$ cm/sec and $T_S = 0^\circ K$ is shown in Fig. 43 by the solid curve. For the oxide impurity lattice approximately 28% of the incident particles are trapped. The effect of adding these trapped particles to the scattering pattern in the form of a cosine distribution is indicated by the dashed line. For comparison the scattering from a pure Ni lattice for corresponding conditions is included as a dotted curve in Fig. 43. The backscattering that occurs from the oxide impurity lattice results from the roughness introduced into the interaction surface by the oxygen atoms. There is also an increased amount of trapping and this decreases the "in-plane" scattering intensity. The dashed curve shows that the amount of trapping is not extensive enough to cause diffuse scattering. Bimodal structuring disappears in going from pure Ni to the Ni x O surface as a result of the large attractive wells. This effect is analogous to that described in Section C.2. for the (He/Ar) scattering.

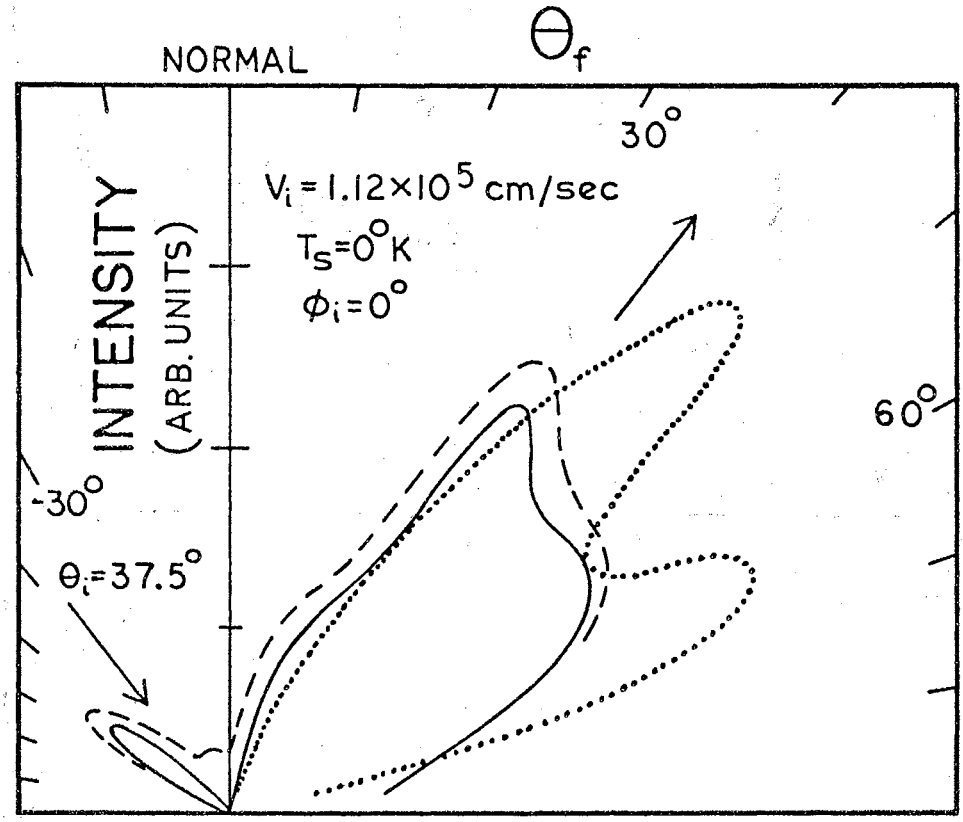

Figure 43. "In-Plane" Scattering for (He/Ni x O). (. . . .), He/Ni; (_____), He/Ni xO; (– – – –), He/Ni x O With Cosine Correction for Trapped Particles.

Scattering from the impure surface is still specularly directed and is rather similar to that from the pure Ni surface. Thus, the model confirms the suspicion of several investigators[30, 43] that in some cases it may be difficult to determine the purity of the surface from scattering data alone. Stickney[43] has recently found that Ne scattered from W has a spatial distribution almost identical to Ne scattered from a monolayer of oxygen on W.

The ETC on the impure lattice for the conditions of Fig. 43 is 0.12 if trapped particles are neglected and 0.34 if they are included in the averaging. As was suggested in Section C, the actual ETC should fall somewhere between these two extremes. The corresponding limits for the interaction with a pure Ni lattice are 0.12-0.13. There is an observable difference between the ETC's for the two surfaces and the origin of this difference is the greatly increased likelihood for trapping on the impure surface. An experimental arrangement that would permit both spatial distribution and final energy distribution measurements to be made would provide a much better probe for determining the nature of a surface.

E. Summary and Conclusions

A classical, gas-solid interaction model has been extended to treat adsorbed particles and impure lattices. Lennard-Jones (12-6) potentials are assumed to operate between the adparticles and the lattice atoms. For the

gas-adparticle and gas-lattice interactions, Morse-type potentials are assumed. Energy transfer coefficients and spatial distributions have been calculated as a function of surface coverage and composition, adatom mass, and adatom-lattice atom binding energy. In general, the results indicate the following:

(1) Surface potential contour lines are relatively smooth for interactions with pure lattices or monolayer surfaces. For half-monolayers and impure lattices the surface is rougher.

(2) A rough surface causes an increased probability of multiple collisions and large energy transfer.

(3) Atoms of an adsorbed monolayer dominate the interaction with the incident gaseous particle. This is in accord with the results reported by Oman.[75]

(4) The ETC increases as the ratio (M_g/M_{Ad}) approaches unity.

(5) The ETC increases as the binding energy between the adparticles and lattice decreases. For small binding energies sputtering of the adatoms by the gaseous particles was observed in the model.

(6) The adatom-adatom interactions have little effect on the ETC. This may result from the restricted surface mobility of adatoms inherent in the model.

(7) The ETC is a strong function of T_S and the vibrational phases of the surface atoms. The functional dependence is not periodic due to anharmonicity.

(8) Spatial scattering distributions are dependent upon the amount of surface roughness. Smooth surfaces give quasi-specular scattering. Rougher surfaces give a significant amount of backscatter. Extremely rough surfaces cause a large number of multiple collisions and decrease the intensity of "in-plane" scattering.

(9) A quasi-specular scattering distribution does not necessarily indicate a pure lattice.

(10) Experimental determination of out-of-plane scattering distributions could be indicative of the degree of surface cleanliness.

CHAPTER VI

CONCLUSION

A. Summary

The phenomena occurring at gas-solid interfaces have been studied with a 3D, classical model. The crystal lattice is assumed to consist of nine movable lattice sites connected to fixed sites by harmonic springs. Lattice impurities can be simulated by changing the identity of lattice atoms. Adsorbed particles are included by means of additional mass points above the lattice. Lennard-Jones (12-6) potentials are assumed to exist between the adparticles and lattice atoms while Morse potential functions operate between the gaseous and surface atoms.

The classical motion equations were solved numerically to yield trajectories that simulate He interacting with a Ni surface. Oxygen impurity atoms and Ar adparticles have also been employed in the model. A number of trajectories were calculated in order to properly average over vibrational phase and aiming point. The ETC and scattering distributions were calculated as a function of initial conditions and interaction potential parameters. In general, the results have indicated the following:

(1) The potential contour lines of the surface are

an important feature of the interaction. A 3D model is necessary because it exhibits deeper attractive wells and less curvature than 2D models. The attractive wells and curvature of the potential surface seem to cause bimodal spatial scattering. The rough surfaces that result from lattice impurities and half-monolayers of adparticles cause multiple collisions and large energy transfer.

(2) The ETC increases with increasing attractive well depth, increases with increasing steepness of the repulsive wall, and increases rapidly with decreasing lattice force constant.

(3) The ETC decreases as the in-plane angle of incidence approaches the surface, and it varies only slightly with the out-of-plane incidence angle.

(4) The ETC decreases as $(T_g - T_s)$ decreases. For nonzero surface temperature, lattice-phase averaging is important.

(5) The ETC increases as the mass or velocity of the gaseous atom increases provided the accelerating effect of the attractive well does not dominate the interaction, in which case an inversion or "turn-up" occurs.

(6) Adsorbed monolayers dominate the interaction with gaseous atoms. The ETC increases as (M_g/M_{Ad}) approaches unity or as the binding energy between the adparticles and lattice decreases.

(7) The 3D model yields spatial scattering distributions that are in semi-quantitative agreement with

experiment. If conditions are such that thermal motion of the lattice dominates scattering, a subspecular shift is predicted to occur with increasing attractive well depth or surface temperature, and a shift toward the surface occurs with increasing gaseous particle incident velocity. For large V_i the structure of the potential surface dominates the interaction and a shift toward the specular angle occurs. The width of the scattering is a decreasing function of V_i. Thermal and velocity-selected incident beams give similar spatial scattering distributions because of the regular dependence of scattering on V_i.

(8) The amount of out-of-plane scattering decreases as V_i increases or as the attractive well depth decreases.

(9) The smooth surface structure of a pure crystal gives quasi-specular scattering. The rougher surfaces caused by adparticles or impure lattices increase the amount of backscatter and out-of-plane scatter. However, quasi-specular scattering does not necessarily indicate a clean surface.

(10) Thermal motion of the lattice causes significant dispersion of gaseous particle velocities; surface structure, on the other hand, has little effect. Bimodal V_f distributions are predicted by the model. Differences in the V_f distributions from thermal and velocity-selected beams should be experimentally observable.

B. Suggestions for Future Work

The general success with which the 3D model treats heterogeneous interaction phenomena indicates that the investigation should be continued. Some suggested areas of further study are the following:

(1) The model could be extended to treat diatomic gaseous molecules. The effects of internal degrees of freedom on the interaction could then be investigated. A study of (H_2/Ni) and (D_2/Ni) systems using the (He/Ni) parameters would permit interesting comparison with the results of this work and experiment.[3, 22, 31] The extension to diatomics would be a step toward the theoretical treatment of surface catalyzed reactions. Potential functions that also allow for chemisorption of the gaseous atoms would be another extension in this direction.

(2) The model could be applied to determine interaction potential parameters. The Morse parameters would be adjusted to fit experimental ETC's and scattering distributions. The curvature parameter, for example, could be fit to the width of the spatial scattering obtained for large E_g^i. The well depth does not then affect the interaction. With α fixed, the well depth parameter could be fit to the width and peak positions for smaller E_g^i. Thus, one could obtain

the potential parameters for many systems that have not been studied by crossed-beam techniques or other methods.

(3) A vital question would be the consistency of the potential parameters obtained by the gas-solid model as compared to other methods. The data necessary to answer the question for (noble gas/K) systems are available. Thomas[14] has reported the AC's. In his experiments T_s, M_g, M_s, and k are fixed. By averaging over θ_i, ϕ_i, and V_i a quantity comparable to experiment could be calculated from the model. The parameters D, Re, and α are the only unknowns; they could be adjusted until the calculated and experimental AC's become equal. The (noble gas/K) potential parameters have also been determined by crossed-beam studies.[98] By comparing results from the two methods, one could evaluate the accuracy of interaction parameters derived from gas-solid experiments.

(4) A check on the validity of the gas-solid model and the predicted interaction parameters would be the success with which it could fit both experimental AC's and spatial scattering distributions with the same set of parameters. For the (Ne/W) system Thomas[14] has reported AC's and Stickney[43] has determined scattering

distributions. It would be interesting and worthwhile to determine the (Ne/W) best-fit Morse parameters from the AC data as described above and to compare the corresponding predicted spatial scattering with experiment.

(5) The limiting factor for the 3D model investigations is computer time. Thus, simplifications that reduce calculation times but give realistic results are necessary if extensive studies are to be attempted. Several simplifications are worthy of consideration

(a) Employ Lennard-Jones (12-6) functions rather than Morse functions to represent the gaseous atom-lattice atom interactions.

(b) Replace the harmonic springs that interconnect lattice atoms with one spring for each movable lattice site. Each lattice atom would then oscillate independently of neighbor atoms, and 65 harmonic functions would be replaced by nine.

(c) Employ more or less surface atoms depending on the nature of the problem being investigated.

(d) Employ a Boltzmann distribution of velocities for the surface atoms.

(6) Sputtering of surface particles by the incident gaseous atoms could be studied with the classical, 3D model. Calculations for Ar incident on a K surface would yield spatial scattering predictions that could be compared with experiment.[40, 99]

(7) Further calculations on the ETC ratio for ^4He and ^3He as a function of E_g^i for nonzero surface temperature could be compared with conductivity cell measurements.[14] Possibly experimental determination of the "crossover" point would fix the well depth parameter.

(8) Calculations designed to investigate the dependence of the bimodal V_f distributions on the potential parameters and initial conditions could specify the origin of the phenomenon. The results could also serve to guide an experimental search for bimodal V_f distributions.

SELECTED BIBLIOGRAPHY

1. Wachman, H. Y., J. Am. Rocket Soc., 32, 2 (1962).

2. Moe, K., AIAA J., 6, 1375 (1968).

3. Moore, G. E., Datz, S., and Taylor, E. H., J. Catalysis, 5, 218 (1966).

4. Hruska, S. J., Conference on Current and Future Problems in High Temperature Chemistry, National Academy of Sciences, Washington, 1967, p. 67.

5. Toba, K., Phys. Fluids, 11, 507 (1968).

6. Epstein, M., AIAA J., 6, 972 (1968).

7. Ward, J. W., Mulford, R. N., and Kahn, R., J. Chem. Phys., 47, 1710 (1967).

8. Knudsen, M., Ann. der Physik, 34, 593 (1911).

9. Jackson, J. M. and Mott, N. F., Proc. Roy Soc., A137, 703 (1932).

10. Roberts, J. K., ibid., A129, 146 (1930).

11. Roach, D. V. and Thomas, L. B., Proc. Intern. Symp. Rarefied Gas Dyn., Suppl. 4, 1, 163 (1967).

12. Hartnett, J. P., ibid., Suppl. 1, 1, 1 (1961).

13. Goodman, F. O., and Wachman, H. Y., J. Chem Phys., 46, 2376 (1967).

14. Thomas, L. B., Proc. Intern. Symp. Rarefied Gas Dyn., Suppl. 4, 1, 155 (1967).

15. Thomas, L. B., Fundamentals of Gas-Surface Interactions, ed. Saltsburg, H., Smith, J. N., Jr., and Rogers, M., Academic Press, New York, 1967, p. 346.

16. Hurlbut, F. C., Proc. Intern. Symp. Rarefied Gas Dyn., Suppl. 4, 1, 1 (1967).

17. Menzel, D. and Kouptsidis, J., Fundamentals of Gas-Surface Interactions, ed. Saltsburg, H., Smith, J. N., Jr., and Rogers, M., Academic Press, New York, 1967, p. 493.

18. Watt, W. and Moreton, R., R.A.E. Tech. Note No. CPM 80, (1964).

19. Wachman, H. Y., Proc. Intern. Symp. Rarefied Gas Dyn., Suppl. 4, 1, 173 (1967).

20. Wachman, H. Y., J. Chem. Phys., 45, 1532 (1966).

21. Crews, J. C., ibid., 37, 2004 (1962).

22. O'Keefe, D. R., et al., ibid., 49, 5194 (1968).

23. Smith, J. N., Jr., et al., ibid., 50, 4667 (1969).

24. Hinchen, J. J. and Foley, W., Proc. Intern. Symp. Rarefied Gas Dyn., Suppl. 3, 2, 505 (1966).

25. Hinchen, J. J. and Shephard, E. F., ibid., Suppl. 4, 1, 239 (1967).

26. Hinchen, J. J. and Malloy, E. S., Fundamentals of Gas-Surface Interactions, ed. Saltsburg, H., Smith, J. N., Jr., and Rogers, M., Academic Press, New York, 1967, p. 448.

27. Smith, J. N., Jr. and Saltsburg, H., J. Chem. Phys., 40, 3585 (1964).

28. Smith, J. N., Jr. and Saltsburg, H., Proc. Intern. Symp. Rarefied Gas Dyn., Suppl. 3, 2, 491 (1966).

29. Saltsburg, H. and Smith, J. N., Jr., J. Chem. Phys., 45, 2175 (1966).

30. Smith, J. N., Jr. and Saltsburg, H., Fundamentals of Gas-Surface Interactions, ed. Saltsburg, H., Smith, J. N., Jr., and Rogers, M., Academic Press, New York, 1967, p. 370.

31. Saltsburg, H., Smith, J. N., Jr., and Palmer, R. L., Proc. Intern. Symp. Rarefied Gas Dyn., Suppl. 4, 1, 223 (1967).

32. Smith, J. N., Jr., Saltsburg, H., and Palmer, R. L., J. Chem. Phys., 49, 1287 (1968).

33. Smith, J. N., Jr., Saltsburg, H., and Palmer, R. L., Proc. Intern. Symp. Rarefied Gas Dyn., Suppl. 5, (in press).

34. Palmer, R. L., Saltsburg, H., and Smith, J. N., Jr., J. Chem. Phys., (in press).

35. Smith, J. N., Jr. and Fite, W. L., Proc. Intern. Symp. Rarefied Gas Dyn., Suppl. 2, 1, 430 (1963).

36. Datz, S., Moore, G. E., and Taylor, E. H., ibid., Suppl. 2, 1, 347 (1963).

37. Somorjai, G. A., Ann. Rev. of Phys. Chem., 19, 251 (1968).

38. Stickney, R. E., Adv. Atomic Molecular Phys., 3, 143 (1967).

39. Daury, G., Constans, A., and Lostis, P., Surface Sci., 14, 103 (1969).

40. Alcalay, J. A. and Knuth, E. L., Proc. Intern. Symp. Rarefied Gas Dyn., Suppl. 4, 1, 253 (1967).

41. Moran, J. P., "Experiments on Scattering of Monoenergetic Ar Beams by Heated Pt", Ph.D. Thesis, Massachusetts Institute of Technology, 1967.

42. Hagena, O. F., Appl. Phys. Letters, 9, 385 (1966).

43. Stickney, R. E., (private communication).

44. Baule, B., Ann. Phys., 44, 145 (1914).

45. Devonshire, A. F., Proc. Roy. Soc., A158, 269 (1937).

46. Goodman, F. O., J. Phys. Chem. Solids, 24, 1451 (1963).

47. Shin, H., J. Chem. Phys., 42, 3443 (1965).

48. Shin, H., J. Phys. Chem., 70, 962 (1966).

49. Shin, H., ibid., 71, 1540 (1967).

50. Jackson, J. M. and Howarth, A., Proc. Roy. Soc., A142 (1933).

51. Piampuu, A. A., Sov. Phys. Tech. Phys., 12, 1397 (1968).

52. Feuer, P., J. Chem. Phys., 39, 1311 (1963).

53. Beder, E., Surface Sci., 1, 242 (1964).

54. Howsmon, A. J., Proc. Intern. Symp. Rarefied Gas Dyn., Suppl. 4, 1, 67 (1967).

55. Gilbey, D. M., ibid., Suppl. 4, 1, 121 (1967).

56. Allen, R. T. and Feuer, P., ibid., Suppl. 4, 1, 109 (1967).

57. Trilling, L., Fundamentals of Gas-Surface Interactions, ed. Saltsburg, H., Smith, J. N., Jr., and Rogers, M., Academic Press, New York, 1967, p. 392.

58. Cabrera, N. B., Disc. Farad. Soc., 28, 16 (1959).

59. Zwanzig, R. W., J. Chem. Phys., 32, 1173 (1960).

60. Goodman, F. O., J. Phys. Chem. Solids, 23, 1269 (1962).

61. Goodman, F. O., ibid., 23, 1491 (1962).

62. Goodman, F. O., ibid., 26, 85 (1965).

63. Goodman, F. O., Proc. Intern. Symp. Rarefied Gas Dyn., Suppl. 3, 2, 366 (1966).

64. Goodman, F. O., Surface Sci., 11, 283 (1968).

65. Goodman, F. O., J. Chem. Phys., 50, 3855 (1969).

66. Chambers, C. M., J. Math. Phys., 6, 1664 (1965).

67. Chambers, C. M. and Kinzer, E. T., Surface Sci., 4, 33 (1966).

68. Goodman, F. O., ibid., 7, 391 (1967).

69. Logan, R. M., Keck, J. C., and Stickney, R. E., Proc. Intern. Symp. Rarefied Gas Dyn., Suppl. 4, 1, 49 (1967).

70. Logan, R. M. and Stickney, R. E., J. Chem. Phys., 44, 195 (1966).

71. Logan, R. M. and Keck, J. C., ibid., 49, 860 (1968).

72. Madix, R. J. and Korus, R. A., J. Phys. Chem. Solids, 29, 1531 (1968).

73. Oman, R. A., Bogan, A., Weiser, C. H., and Li, C. H., AIAA J., 2, 1722 (1964).

74. Oman, R. A., Bogan, A., and Li, C. H., Proc. Intern. Symp. Rarefied Gas Dyn., Suppl. 3, 2, 396 (1966).

75. Oman, R. A., AIAA J., 5, 1280 (1967).

76. Oman, R. A., Proc. Intern. Symp. Rarefied Gas Dyn., Suppl. 4, 1, 83 (1967).

77. Oman, R. A., J. Chem. Phys., 48, 3919 (1968).

78. Oman, R. A., Proc. Intern. Symp. Rarefied Gas Dyn., Suppl. 5, (in press).

79. Raff, L. M., Lorenzen, J., and McCoy, B. C., J. Chem. Phys., 46, 4265 (1967).

80. Landau, L. D. and Lifshitz, E. M., Quantum Mechanics, Addison-Wesley, Reading, Massachusetts, 1958, p. 158.

81. Keck, J. C., Adv. Chem. Phys., 13, 85 (1967).

82. Rapp, D., J. Chem. Phys., 40, 2813 (1963).

83. Raff, L. M., ibid., 46, 520 (1967).

84. Karplus, M., Porter, R. N., and Sharma, R. D., ibid., 43, 3259 (1965).

85. Latta, T. M., University of Illinois, Graduate College, Digital Computer Laboratory, 7090/7094 Library Routine D2-UDI-ADM-3-36-SR (unpublished).

86. Karplus, M. and Raff, L. M., J. Chem. Phys., 44, 1212 (1966).

87. Devienne, F. M., Souquet, J., and Roustan, J. C., Proc. Intern. Symp. Rarefied Gas Dyn., Suppl. 4, 2, 584 (1966).

88. Thomas, L. B. and Schofield, E. B., J. Chem. Phys., 23, 861 (1955).

89. Stickney, R. E., et. al., Fundamentals of Gas-Surface Interactions, ed. Saltsburg, H., Smith, J. N., Jr., and Rogers, M., Academic Press, New York, 1967, p. 422.

90. Duren, D., et. al., Phys. Letts., 18, 282 (1965).

91. Moehwyn-Hughes, E. A., Physical Chemistry, Pergamon Press, London, 1957, p. 104.

92. International Critical Tables, 1, 340 (1926).

93. Hirschfelder, J. O., Curtiss, C. F., and Bird, R. B., Molecular Theory of Gases and Liquids, John Wiley and Sons, Inc., New York, 1954, p.1110.

94. Müller, K., Z. fur Physik, 195, 105 (1966).

95. Kaufman, L., AIME, 224, 1006 (1962).

96. Germer, L. H., Surface Sci., 5, 147 (1966).

97. Bauer, E., ibid., 5, 152 (1966).

98. Von Busch, F. R., Strunk, H. J., and Schlier, C. H., Phys. Letts., 16, 268 (1965).

99. Stein, R. P. and Hurlbut, F. C., Proc. Intern. Symp. Rarefied Gas Dyn., Suppl. 1, 1, 39 (1961).

VITA

Jerry Alan Lorenzen

Candidate for the Degree of

Doctor of Philosophy

Thesis: A THEORETICAL INVESTIGATION OF GAS-SOLID INTERACTION PHENOMENA

Major Field: Chemistry

Biographical:

Personal Data: Born in Grand Island, Nebraska, October 3, 1944, the son of Max and Norma Lorenzen.

Education: Graduated from Senior High School, Grand Island, Nebraska, in May, 1962; received the Bachelor of Science degree with a major in mathematics from Midland Lutheran College, Fremont, Nebraska, in May, 1966; completed requirements for the Doctor of Philosophy degree at Oklahoma State University in May, 1970, as a National Aeronautics and Space Administration Trainee.

Professional Experience: National Science Foundation Undergraduate Research Participant, Summer 1965; Formulations Department Lab Technician, Chemagro Chemical Company, Summer 1966; Graduate Teaching Assistant, Oklahoma State University, 1966 and 1967.